THESIS FOR THE DEGREE OF LICENTIATE OF ENGINEERING

# A tandem Catalyst for hydrogenation of $CO_2$ to light olefins — The role of the zeolite component

Wei Di


*Chemical Engineering Division*
*Department of Chemistry and Chemical Engineering*

CHALMERS UNIVERSITY OF TECHNOLOGY

Gothenburg, Sweden 2023

A tandem catalyst for hydrogenation of $CO_2$ to light olefins — The role of the zeolite component

Wei Di



Licentiatuppsatser vid Institutionen för kemi och kemiteknik
Chalmers tekniska högskola.
Nr 2023:02

Department of Chemistry and Chemical Engineering
Chalmers University of Technology
SE-412 96 Gothenburg
Sweden
Telephone + 46 (0)31-772 1000

Printed by Chalmers Digitaltryck
Gothenburg, Sweden 2023

A tandem catalyst for hydrogenation of $CO_2$ to light olefins

— The role of the zeolite component

Wei Di

Department of Chemistry and Chemical Engineering
Chalmers University of Technology, Gothenburg 2023

## Abstract

The catalytic conversion of waste $CO_2$ into light olefins offers a sustainable pathway for green chemicals production in the future. Over a tandem catalyst with the bifunctional active sites for methanol synthesis (CTM) and methanol to olefins (MTO), $CO_2$ can be efficiently converted via intermediate methanol into a mixture of light olefins (ethylene, propene, butene). In the study of $CO_2$ hydrogenation, the moderately acidic SAPO-34 molecular sieve is often used as the MTO catalyst component. SAPO-34 performs well for the formation of C-C bonds without fast coking, and minimal further hydrogenation of olefins. These qualities give the catalyst a long lifetime and high selectivity for light olefins. Unfortunately, under high-pressure hydrothermal conditions, it easily suffers structural damage.

In this context, the SSZ-13 zeolite, an alternative MTO catalyst with higher hydrothermal stability, but also stronger acidity, was systematically investigated and modulated with the aim to achieve high selectivity for light olefins and high stability during $CO_2$ hydrogenation. Firstly, in order to identify the effect of zeolite acidity on product distribution and coke deposition, two types of SSZ-13 zeolites with similar bulk composition, but different protonic acid site distributions, were synthesized. They were combined with a stable CTM catalyst (bulk indium oxide, $In_2O_3$) as a tandem catalyst and were evaluated in $CO_2$ hydrogenation. The SSZ-13 with isolated acid sites had a lower Brønsted acid site (BAS) density and exhibited a higher selectivity for light olefins compared with the one with paired protonic acid sites. By exchanging $Na^+$ cations to tailor the BAS density of SSZ-13 zeolite, the comparative experiments further indicated that the BAS density, rather than BAS distribution, had a high correlation with the selectivity for light olefins, which proved that the BAS density had the primary impact on the product distribution. The high BAS density promoted hydrogenation which reduced the selectivity for light olefins, while low BAS density tended to accumulate excessive coke leading to catalyst deactivation, but with improved selectivity for olefins. Thereafter, over the tandem catalysts with the optimized BAS density, a transient experiment with varying reaction conditions was carried out to investigate the coke evolution during $CO_2$ hydrogenation. The results indicated that the coking behavior of SSZ-13 zeolite was significantly affected by reaction conditions. By manipulating the reaction temperature and pressure, the active coke species, or so-called hydrocarbon pool species ($HCP_S$), can be deposited inside the zeolite in a targeted manner, thereby modifying the catalyst to achieve a higher MTO activity and lower olefin hydrogenation activity. Continuous transient experiments further revealed a dynamic equilibrium between the formation and degradation of coke inside SSZ-13 zeolite. This balance is established under the appropriate BAS density and optimized reaction temperature and pressure. Using the conditions of 20 bar and 375 °C, with a $H_2$ to $CO_2$ mole ratio of 3, the results obtained for the pre-coked tandem catalysts of $In_2O_3$ and SSZ-13 (BAS density = 0.23 $mmol*g^{-1}$) exhibited very stable activity, with selectivity for light olefins around 70% ± 2% (among hydrocarbon products), and low average coke deposition rate of 0.016 $wt.\%*h^{-1}$ over 100 h time-on-stream. This result also experimentally confirmed the success of pre-coking modification and verified the balance mechanism of coke accumulation.

**Keywords:** $CO_2$ hydrogenation, methanol-intermediate, light olefins, tandem catalysts, MTO reaction, SSZ-13 zeolite, Brønsted acid density, Al distribution, pre-coking, HCPs

# Acknowledgments

The research in this thesis was carried out at the Division of Chemical Engineering, Competence Centre for Catalysis (KCK), and Centre for Process Chemical Engineering (CPE), Chalmers University of Technology, Gothenburg, Sweden, from September 2020 to February 2023. Swedish Energy Agency is gratefully acknowledged for its financial support (P49617-1).

Additionally, I would like to express my gratitude to those who have guided, helped, and encouraged me during my Ph.D. studies.

First, I would like to express my deepest gratitude to my main supervisor Professor Derek Creaser, and my examiner and co-supervisor Professor Louise Olsson. Thank you for your trust, support, encouragement, and guidance. I am very grateful to join your research group and engage in research topics that fascinate me. Your tireless guidance and hard work always inspire me to move forward. I appreciate your profound knowledge, and value your patience and rigorous academic attitude, which benefit me a lot. Thank you so much!

I also would like to thank:

Prof. Oleg Pajalic from Perstorp AB, and Prof. Lars Josefsson from Josefsson Sustainable Chemistry AB, for your discussion and advice at various stages of my research, as well as your precious comments on my papers and thesis.

Prof. Claes Niklasson, Prof. Ronnie Andersson, and Senior Lecturer Gunnar Eriksson, I am very grateful to learn professional knowledge from you and have your help during teaching assistant work.

Abdenour Achour, Phuoc Hoang Ho, and Sreetama Ghosh, for all your efforts in our collaborations, I appreciate your assistance and suggestion, and I am looking forward to more technical discussions and collaborations in the future.

All current and former colleagues and friends in the Chemical Engineering division and KCK. Johanna Spång, Anna Oskarsson, and Malin Larsson for all your effective administrative support; Michael Andersson-Sarning for timely support on instrument troubleshooting and procurement; Prof. Diana Bernin and Dr. Tobias Sparrman for your help with NMR measurement; Jojo for your help with DRIFTS; Alexander Michael Riddell for assistance with UV-Vis; Andreas Schaefer for test on XRF; Joonsoo Han, Emma Olsson Månsson, Elham Nejadmoghadam, You Wayne Cheah, Jieling Shao, Andres Suarez, Dawei Yao, Aqsa Noreen, Rawipa Intakul, Prabin Dhakal, Quoc Khanh Tran, Emmanouela Leventaki, Joanna Wojtasz-Mucha, and Francisco Baena-Moreno for creating a wonderful work environment in our division; Previous colleagues Aiyong Wang, Muhammad Abdus Salam, Rojin Feizie Ilmasani, Joby Sebastian, Patric Kvist, Tobias Eidevåg, and Xueting Wang for all your help at the beginning of my Ph.D.

At last, special gratitude is owed to my wife Lili, my daughter Dasiy, and my parents, thanks for your endless love and encouragement!

Wei Di

Göteborg, February 20,2023

## List of Publications Included in the Thesis

This thesis is based on the following two appended papers. For each paper, the author of this thesis contributed to the research plan with co-authors, performed the experiments, analyzed the data, wrote the manuscript, and revised the paper according to the feedback from co-authors and reviewers.

### Paper I

$CO_2$ hydrogenation to light olefins using $In_2O_3$ and SSZ-13 catalyst −Effect of varying the Al distribution during SSZ-13 zeolite synthesis.

Wei Di, Phuoc Hoang Ho, Abdenour Achour, Oleg Pajalic, Lars Josefsson, Louise Olsson, and Derek Creaser.

Submitted

### Paper II

Modulating the formation of coke to improve the production of light olefins from $CO_2$ hydrogenation over $In_2O_3$ & SSZ-13 catalysts

Wei Di, Abdenour Achour, Phuoc Hoang Ho, Sreetama Ghosh, Oleg Pajalic, Lars Josefsson, Louise Olsson, and Derek Creaser.

Manuscript

## Publications not included in the Thesis

### Paper I

Role of the supports during phosphorus poisoning of diesel oxidation catalysts

Phuoc Hoang Ho, Jieling Shao, Dawei Yao, Wei Di, Derek Creaser, and Louise Olsson

Submitted.

## List of abbreviations

| | |
|---|---|
| BAS | Brønsted acid sites |
| BET | Brunauer, Emmett and Teller |
| BJH | Barret Joyner Halenda |
| CAPEX | Capital expenditures |
| CCS | Carbon capture and storage |
| CCUS | Carbon capture, utilization, and storage |
| CHA | Chabazite |
| COM | $CO_2$ to methanol |
| $C_n^0$ | Alkane with carbon chain length *n* |
| $C_n^=$ | Alkene with carbon chain length *n* |
| CP | Cross-polarization |
| DRIFTS | Diffuse reflectance infrared Fourier transform spectroscopy |
| DME | Dimethyl ether |
| FTS | Fischer–Tropsch synthesis |
| FID | Flame ionization detector |
| GC | Chromatography |
| GHGs | Greenhouse gases |
| GHSV | Gas hourly space velocity |
| HCPs | Hydrocarbon pool species |
| ICP | Inductively coupled plasma |
| MAS NMR | Nuclear magnetic resonance |
| MeOH | Methanol |
| MTO | Methanol to olefins |
| MS | Mass spectrometer |
| MFC | Mass flow controller |
| OPEX | Operating expenses |
| RWGS | Reverse water gas shift |
| SEM | Scanning electron microscope |
| SAR | Silicon to aluminum mole ratio |

| | |
|---|---|
| SDA | Structure directing agent |
| TPD | Temperature-programmed desorption |
| TPO | Temperature-programmed oxidization |
| TCD | Thermal conductivity detector |
| TGA | Thermogravimetric analysis |
| TOS | Time-on-stream |
| $TEAda^+$ | N, N, N-trimethyl-1-adamantylammonium |
| UV-Vis | Ultraviolet-visible |
| XRD | X-ray diffraction |
| XRF | X-ray fluorescence |

# Contents

# 1 Introduction

## 1.1 Reducing $CO_2$ emissions

The surge in global energy demand, combined with an overreliance on fossil fuels, has led to a dramatic surge in the emissions of harmful greenhouse gases (GHGs), especially carbon dioxide, over the past hundred years. In 2021, the Global $CO_2$ emissions from the combustion of fossil fuels and industrial processes reached the highest level ever of 36.3 gigatons (Gt) (seen in Figure 1), which led the concentration of $CO_2$ in the atmosphere to be as high as 417.19 ppm, which is 1.5 times what it was at the beginning of the pre-industrial revolution era (in 1750) [1]. The consequences of these anthropogenic emissions are far-reaching, disrupting the Earth's natural carbon cycle and causing global warming, ocean acidification, sea-level rise, and other harmful impacts, including climate change. Aiming to tackle the climate crisis, world leaders reached a consensus via the Paris Agreement in 2015 and pledged to limit the global temperature increase during this century to 2 °C, while continuing efforts to limit the increase even further to 1.5 °C [2]. As per the Paris Agreement, more stringent restrictions on emission levels of GHGs were recommended across the globe, and by the end of 2020, the world's major economies and countries have given the promise to achieve net-zero $CO_2$ emissions by mid-century [2]. In view of its commitment to the Paris Agreement, the European Union (EU) is taking a leading role to achieve higher emission reduction targets than the current ones [3]. In the "European Green Deal" communication, the European community proposed to increase the GHGs emission reduction target for 2030 to at least 50%, and towards 55% compared with 1990, in order to achieve net zero GHGs emissions by 2050, and thereby become the world's first major economy to achieve climate neutrality by mid-century [4]. However, the actions required to achieve this goal are far more difficult than realized. As there is no silver bullet for net-zero emissions, achieving this grand "blue map" requires a combination of a series of efforts, not only including the upgrading of energy-saving policies and consumption technologies, the adoption of alternative energy (e.g., nuclear, renewable energy), but also the contribution from carbon capture and storage (CCS) and carbon capture and utilization (CCU) [4,5]. The McKinsey report estimated the global CCS potential at 3.6 Gt, and Europe at 0.4 Gt – roughly 20% of the total European emissions reduction potential in 2030 [6]. This means that a large amount of $CO_2$ will become gradually available for permanent storage or use in the future. Considering the high economic cost, and the potential geological and ecological risks of storage by CCS [1,5,6], a more pragmatic method is to convert $CO_2$ into carbon-based materials and fuels by using chemical methods in order, to realize sustainable utilization of carbon resources. From this perspective, $CO_2$ will be regarded as a raw carbon-based material rather than a waste.

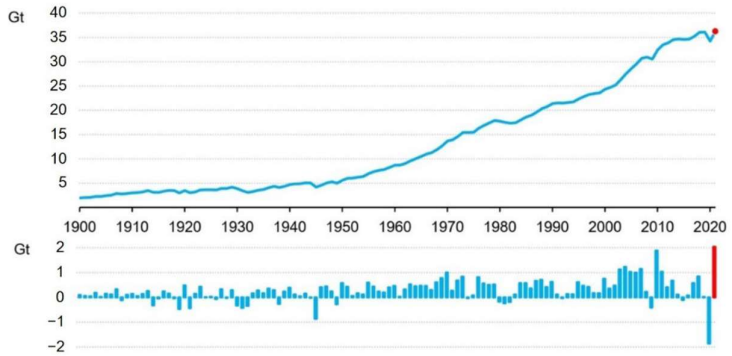


**Figure 1** $CO_2$ emissions and their annual change from 1900 to 2021. Reprinted from ref. [1]. MDPI Open Access License.

Until now, the utilization of $CO_2$ remains small compared to global anthropogenic $CO_2$ emissions. The use of $CO_2$ is estimated from 200 Mt to 500 Mt per year [3], Although 150 known chemicals can be obtained by converting $CO_2$ [7], most of which are limited to a few industry processes, such as food, agrochemicals (urea and carbonate fertilizer), welding, foaming, fire extinguishers, propellants, etc. [1]. Due to the high thermodynamic stability of $CO_2$ molecules, the conversion of $CO_2$ requires high energy and technical input [7]. In addition, other factors such as environmental (carbon tax) and economic indicators ($CO_2$ capture cost and product value) also may discourage the use of $CO_2$. In recent years, with the large-scale application of renewable resources to produce carbon-free energy and green hydrogen, the conversion of emitted $CO_2$ by hydrogenation is ushering in major opportunities [8]. More and more attention has been paid to conversion of $CO_2$ to high value-added products, such as fuels and light olefins.

## 1.2 Green light olefin production from $CO_2$ hydrogenation

Light olefins (Ethylene, Propylene, and Butene) are the building blocks of the modern chemical industry. Currently, most of the produced ethylene and propylene are used to produce polymers, such as polyethylene (PE), polyvinyl chloride (PVC), ethylene glycol (EG), acrylonitrile, cumene, and acrylic acid, widely used in packaging, textile, paint, and other industries. In addition, isobutylene is a basic raw material for plastics, rubber, and pharmaceutical products [9]. By the end of 2022, global ethylene consumption reached 177 million tons per year [10], and propylene consumption reached 125 million tons per year [11]. Traditionally, most of the raw materials for the production of light olefins comes from crude oil and natural gas (shown in Figure 2) [6], and more than 60% of the production capacity comes from the steam cracking process [9]. However, this production is the most energy-consuming process and one of the major contributors to the emissions of $CO_2$. Steam cracking accounts for approximately 3 EJ of primary energy use (due to the combustion of fossil fuels, excluding the energy content of the product) and almost 200 Mt of $CO_2$ emissions (due to the combustion of fossil fuels). The pyrolysis section of the Naphtha steam cracker alone consumes approximately 65% of the total process energy and accounts for approximately 75% of the total energy losses [6]. In contrast, if the emitted $CO_2$ is converted into low-carbon olefins with the help of green hydrogen produced by renewable energy, it will not only effectively reduce the consumption of fossil energy, but also effectively store and transport the renewable energy resources. Therefore, there is a tremendous benefit to producing green olefins from $CO_2$ and green hydrogen in terms of mitigating climate change. The benefits include: (i) Avoidance of the severe $CO_2$ emissions and fossil resource consumption during the current production processes; (ii) Re-use of waste $CO_2$; (iii) The ability to store $CO_2$ in the commodities made from olefins with relatively long lifecycles, such as polymer products [6].

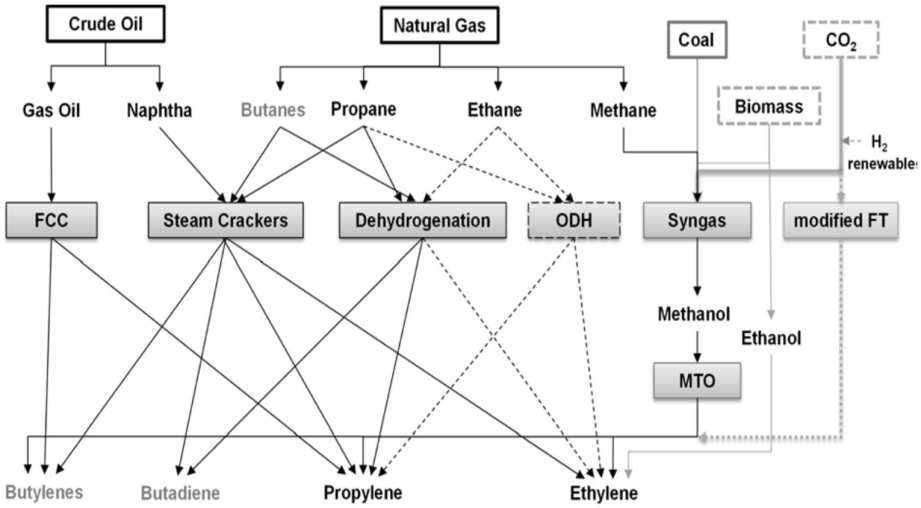


**Figure 2.** Production routes for light olefins regarding various raw materials. The dashed lines indicate processes under development. Reprinted with the permission from ref. [6]. Copyright (2011) WILEY-VCH

Among the many methods of $CO_2$ valorization, thermochemical conversion of $CO_2$ with the aid of heterogenous catalysts is considered to be the closest route to industrial application [12]. Specifically, in the area of heterogeneous catalysis for $CO_2$ to light olefins (CTO), there are two accepted reaction pathways: (1) the CO-intermediate pathway: hydrogenation of $CO_2$ to CO via a reverse water-gas shift (RWGS) reaction, followed by hydrogenation of CO via the Fischer–Tropsch synthesis (FTS) reaction to produce olefins; (2) the methanol-intermediate pathway: hydrogenation of $CO_2$ to methanol followed by the dehydration of methanol to form light olefins [1,9,12-15]. These two routes involve two different steps, the entire reactions can be either carried out in separate reactors (indirect route) or one reactor (direct route). Usually, when the two steps are not mutually exclusive, conduction within a single reactor (direct route) is feasible. Therefore, the direct catalytic hydrogenation to convert $CO_2$ to olefins in a single reactor is of interest because it may be more economical and energy efficient, which is critical to process viability.

## 1.3 Catalytic hydrogenation of $CO_2$ to light olefins over a tandem catalyst

Recent research has focused on optimizing single-step processes for the synthesis of olefins from $CO_2$ as well as developing more efficient catalysts [9,12,15]. In a CO-intermediate pathway, the entire reaction of $CO_2$ to CO by RWGS and subsequent conversion of CO to hydrocarbons by FTS, can occur simultaneously on a standalone Fischer-Tropsch (FT) catalyst. Therefore, this pathway is also referred to as a $CO_2$ modified FT process. As the proliferation of hydrocarbon chains directly follows the mechanism of the FTS reaction, in the FT process, the maximum selectivity of the light olefin products is limited by the Anderson–Schulz–Flory (ASF) distribution. The maximum selectivity for $C_2$-$C_4$ hydrocarbons is only 58% [16]. In contrast, in a methanol-intermediate pathway, $CO_2$ is first converted to methanol (CTM) over a CTM catalyst, followed by the transformation of methanol to olefins (MTO) over a zeolite/zeotype catalyst. This sequence of processes can obtain a higher selectivity for light olefins among hydrocarbon products, and it can also be achieved in a single reactor where a tandem catalyst system is used exhibiting bifunctional properties (CTM and MTO) as discussed above. In a tandem approach, the CTM and MTO catalysts are mixed to varying degrees of intimate contact, such as granular and powder, to achieve maximum synergy [15]. The catalysts for the CTM have been extensively reported, including industrial catalysts $Cu/ZnO/Al_2O_3$ and newer catalysts such as $In_2O_3$ oxides and others [17-21]. The zeolite/zeotype catalysts, such as SAPO-34 molecular sieve and SSZ-13

zeolite, have been widely addressed for C-C formation in MTO reaction due to their special CHA topology that shape selectively prefers light olefin products [22-26]. However, since these CTM and MTO reactions have their respective optimized reaction condition regimes, integrating them in one reactor needs stringent requirements to be met, including the use of mutually suitable reaction conditions that are also appropriate for the sensitive properties of the catalyst components [27]. For example, the $CO_2$ molecule is relatively inert, and requires elevated temperatures to be activated during the hydrogenation. The hydrogenation of $CO_2$ to methanol is also accompanied by the reverse water gas shift (RWGS) reaction to form CO. Therefore, the high temperature in the CTM reaction increases the conversion rate of $CO_2$, which greatly favors the RWGS thermodynamically, giving a higher selectivity for CO in the product [17-21]. In addition, in the MTO reactions with $H_2$ co-feeding (similar atmosphere as the methanol-mediated $CO_2$ hydrogenation), higher temperatures tend to be favorable for good stability of the zeolite/zeotype catalyst [28-29]. However, high temperatures also promote excessive hydrogenation of olefin products, resulting in decreased selectivity for alkenes and increased selectivity for alkanes, especially over strong acidic MTO catalysts, such as SSZ-13 zeolite [29]. Recently, some new studies have found that the co-feeding of water and hydrogen with methanol can effectively alleviate the quick coke deposition over SAPO-34 at high temperatures while maintaining high selectivity for olefins. Unfortunately, under high-temperature hydrothermal conditions, the SAPO-34 catalyst experiences structural damage [30]. In contrast, the SSZ-13 zeolite has better hydrothermal stability [31], and stronger BAS strength [29], resulting in an optimal production rate of olefins at a lower temperature [32]. However, due to its strong acidity, SSZ-13 tends to have a quicker deactivation under pure MTO reaction conditions, and exhibit high selectivity for paraffins during the hydrogenation of CO or $CO_2$ [27]. So far, there are few studies on how to tailor SSZ-13 zeolites and apply them as effective MTO catalysts in the $CO_2$ hydrogenation to light olefins process.

## 1.4 Objectives and scopes

The purpose of this work is to investigate an efficient and stable MTO catalyst component in the tandem catalyst for $CO_2$ hydrogenation to light olefins. Specifically, the SSZ-13 zeolite, a zeolitic homologue of the SAPO-34 molecular sieve with highly hydrothermal stability and varying acidity, was synthesized and used as zeolite component of the tandem catalyst. Its catalytic performance was investigated for light olefins production in $CO_2$ hydrogenation, and the mechanism related to olefins formation and coke deposition was explored based on catalyst modification and process optimization.

In Paper **I**, starting from the synthesis of SSZ-13 zeolites with varying acid densities and acid sites distributions, the physicochemical properties of SSZ-13 zeolites were characterized, and their catalytic performance was systematically investigated in catalyzing $CO_2$ hydrogenation to olefins. By correlating the reactivity with the physicochemical properties of catalysts, before and after the reaction, it was revealed that the Brønsted acid density of zeolites was the main factor affecting product selectivity and coke formation.

Then, in **Paper II**, taking the low acidic SSZ-13 catalyst as the research subject, a transient experiment with varying reaction conditions was carried out to investigate the formation and degradation of trapped coke within the catalysts during the hydrogenation of $CO_2$ to olefins, in combination with various characterization techniques including $N_2$ adsorption, DRIFTS, TGA, GC-MS, and TPO. A dynamic balance mechanism between the formation and degradation of coke was disclosed, and a pre-coking method was proposed for upgrading the fresh catalyst in order to improve the selectivity for product and the stability of the catalyst. Finally, the balance mechanism was verified through a long-term (100 h) stability test, and the pre-coking modification was also confirmed to be successful in improving the reaction performance of SSZ-13 within the $In_2O_3$/SSZ-13 tandem catalyst.

## 1.5 Outline of thesis

The outline of this thesis is as follows:

**Chapter 1:** General introduction, motivation, and objectives.

**Chapter 2**: Introduction to the technical background, progress, and challenges of methanol-mediated $CO_2$ hydrogenation to olefins.

**Chapter 3**: Description of the material synthesis and characterization methodology used in the experiments.

**Chapter 4**: Key findings and associated interpretations in papers.

**Chapter 5**: Main conclusions.

**Chapter 6**: Future work.

# 2 Background

The Methanol-mediated synthesis of light olefins from $CO_2$ comprises two consecutive reactions: $CO_2$-to-MeOH (CTM) and MeOH-to-olefins (MTO) processes. In this chapter, the CTM and MTO reactions as well as their catalyst components, will be introduced respectively. The synergy within the tandem catalyst system will also be elaborated.

## 2.1 $CO_2$ to Methanol (CTM) catalyst

In the context of applying either CO or $CO_2$ as a feedstock in methanol synthesis, catalyst development and mechanism research for methanol synthesis has continued uninterrupted for nearly one hundred years. All catalysts developments are based on the following three main coupled equilibrium reactions [18]:

$$CO_2 + 3H_2 \rightleftharpoons CH_3OH + H_2O, \qquad \Delta H_{298\ ,50bar} = -50kJmol^{-1} \qquad (1)$$

$$CO_2 + H_2 \rightleftharpoons CO + H_2O, \qquad \Delta H_{298K,10bar} = 41kJmol^{-1} \qquad (2)$$

$$CO + 2H_2 \rightleftharpoons CH_3OH, \qquad \Delta H_{298K,50bar} = -91kJmol^{-1} \qquad (3)$$

From the above reactions, it can be seen that methanol formation and the reverse water-gas shift (RWGS) reaction compete with each other [Eqs. (1) and (2)]. According to the results of isotope labeling and kinetic experiments, it has been proven that $CO_2$ is the predominant carbon source for methanol synthesis, and $CO_2$ can be directly converted to methanol without a preliminary reduction to CO. In view of thermodynamics, since the methanol formations [Eqs. (1) and (3)] are exothermic while the RWGS reaction is endothermic, a low reaction temperature and high reaction pressure are more favorable for methanol synthesis. However, a higher temperature is helpful for $CO_2$ activation from a kinetic aspect. Therefore, a compromise is usually made, where a moderate reaction temperature is used (at ~ 230 °C) to achieve a high yield (~ 30% at 50 bar) of methanol from $CO_2$ [33]. In general, low temperatures, high pressures, and high $H_2$: $CO_x$ ratios are beneficial for high methanol yields. In addition, the ratio of $CO/CO_2$ is another key factor affecting the methanol yield. Under conditions applying CO-rich syngas (CO + $H_2$) as feedstock, the water-gas shift reaction [WGS, reverse of Eqs. (2)] is prevalent. Adding a certain amount of $CO_2$ in the $CO/H_2$ feed can drastically improve the yield of methanol and the energy balance. So far, in industrial applications, the amount of $CO_2$ added has reached as high as 30% of the total carbon in the syngas [17]. While, under $CO_2$-enriched feed conditions, the RWGS reaction is dominant, and strongly affects the equilibrium yield of methanol due to the formation of additional water and CO in this parallel reaction. As the result, the thermodynamics for methanol production from $CO_2$ are lower than those for the production of methanol from CO. For example, the equilibrium yield of methanol from $CO_2$ is less than 40% at 200 °C and 50 bar, whereas the yield from CO is greater than 80% at the same conditions [17]. In industrial production, in order to obtain a higher methanol yield and $CO_2$ conversion rate as close to the equilibrium as possible, the CO product would be separated from the liquid products (water, methanol, and other high alcohols) and recycled back to the reactor inlet, mixed with fresh $CO_2$ and reacted again in the reactor at an optimized $CO/CO_2$ ratio [19]. Fornero et al. performed a process simulation for the hydrogenation of $CO_2$ to produce methanol in a reaction system with recycling non-condensable gas, it was found that a complete conversion of $CO_2$ over a process could be achieved using a recycle ratio (the ratio of the molar flow rate of the recycle gases to that of the fresh feed gases) of 5 at T=250 °C (P≥40 bar), or at T=235 °C (P≥30 bar) [34].

The commercial $CuO/ZnO/Al_2O_3$ catalysts, widely used in the production of methanol from syngas, present poor performance for $CO_2$ hydrogenation at high temperatures [18-21]. The increased temperature can facilitate $CO_2$ activation, however, the undesirable CO and $H_2O$ are formed by RWGS, reducing methanol selectivity. Moreover, a large amount of water generated during $CO_2$ hydrogenation to methanol and RWGS reaction are adsorbed on the surface of the catalyst, which seriously decreases the stability of the $CuO/ZnO/Al_2O_3$ catalyst. Water is considered to accelerate the growth of copper crystals at high temperatures, reduce the specific surface area, and cause sintering. At the same time, water will also accelerate the separation of Cu and ZnO active components at high temperatures, reducing their synergy and losing their activity [35]. Thus, at higher operation temperatures, the water and strong reductive atmosphere can lead to the formation of inactive $Cu^0$-$Zn^0$ bulk alloy, thereby eventually causing complete deactivation.

To improve the reactivity and stability during $CO_2$ hydrogenation, alternative catalysts for $CuO/Zn/Al_2O_3$ have been extensively investigated, and most of them can be divided into three categories. One category involves improved Cu-based catalysts, and the other is noble metal-based catalysts and a third is novel oxides catalysts [18-21]. In modified copper-based catalysts, most of the work attempts to enhance or maintain the Cu-ZnO binary core active components by introducing promoters or alternative supports. For example, the addition of noble metal promoters (such as Pt, Au, Rh, and Pd, et .al) are used to improve the low-temperature activity of the Cu-Zn catalyst. The promoters of Zr, Ga, and F were reported to modify the basicity /acidity and physiochemical properties of $Al_2O_3$ supports, which can enhance the activity or increase the selectivity towards methanol. In addition to being used a dopant, zirconia is often used to replace alumina as a support of Cu-Zn catalysts, and demonstrated a beneficial effect on $CO_2$ hydrogenation, where the enhanced activity and increased selectivity to methanol was assigned to the stabilization of highly dispersed Cu nanoparticles on the surface, and additional $CO_2$ adsorption on its basic sites, followed by hydrogenation on the adjacent Cu-ZnO active sites. The enhanced stability was attributed to the weak hydrophilic character of $ZrO_2$, which alleviates the strong adsorption of water on the catalyst surface [21]. In addition to the above-mentioned copper-based catalysts, noble metal catalysts, represented by Pd and Au, have also been widely reported. Supported on $CeO_2$, ZnO, $Ga_2O_3$, and $In_2O_3$, Pd-based catalysts exhibit good performance in $CO_2$ hydrogenation to methanol, and especially demonstrate a high selectivity for methanol at low temperatures (250 °C), but lower activity compared with copper-based catalysts [20]. In addition, noble metal catalysts have higher sulfur tolerance than copper, which offers another advantage of noble metal catalysts. However, at high temperatures (>300 °C), noble metal catalysts also exhibit strong activity toward RWGS and methanation reactions, resulting in high selectivity for CO and $CH_4$ in the product [20-21]. In recent years, the novel oxide catalysts represented by $In_2O_3$-based oxides and $ZrO_2$-based solid solutions $M_aZrO_y$ (Zn, Ga, Cd), are emerging as an effective catalyst for $CO_2$ hydrogenation to methanol. Most typically, these are outstanding with a high selectivity for methanol and good stability at high reaction temperatures (>300 °C). Unlike copper-based catalysts, the active centers in these $In_2O_3$-based or $ZrO_2$-based catalysts are derived from the oxygen vacancies generated by the partial reduction of the surface. It is considered that the active oxygen vacancies provide a strong binding for adsorbed species such as $CO_2$ and $H_2$, allowing hydrogenation at high reaction temperatures. Furthermore, the CO formation via surface redox mechanisms is reduced due to slight surface reduction [20].

Since it was first reported in 2016, indium oxide ($In_2O_3$) has been regarded as a breakthrough system due to its very high methanol selectivity [36]. The kinetic experiments by Pérez-Ramírez et al. found that the apparent activation energy of $CO_2$ hydrogenation to methanol over a bulk $In_2O_3$ catalyst was lower than that of the RWGS reaction, which was consistent with the high selectivity for methanol in experimental observation [37]. Some detailed mechanistic studies also indicated that the hydrogenation of $CO_2$ to HCOO was thermodynamically and kinetically favorable over the oxygen vacancies on the

surface of $In_2O_3$(110), which can also stabilize the key intermediates involved in the formation of methanol, including HCOO, $H_2COO$, and $H_2CO$. On the contrary, the $H_2CO$ and $H_2COO$ species were not stable on the surface of Cu (111) [38-39]. In a related mechanism rooted in the creation and elimination of oxygen vacancies (mark as $V_o$ sites as active sites) on $In_2O_3$ (110) (seen in Figure 3), the hydrogenation of $H_2CO$ was proposed as the rate-determining step (RDS). In a whole reaction cycle mechanism, the oxygen vacancies could be recovered during $CO_2$ hydrogenation [39].

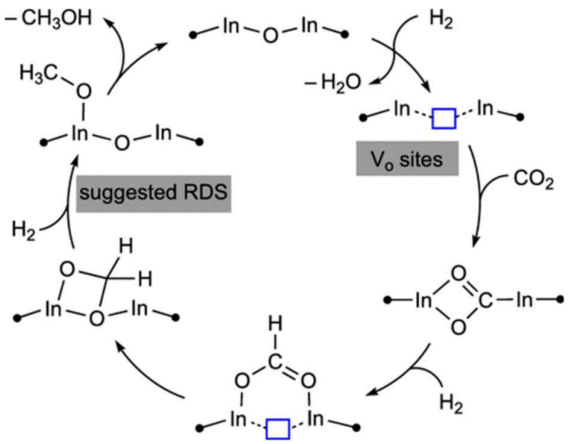


**Figure 3.** The Mechanism for the Hydrogenation of $CO_2$ to Methanol on Vo Sites of $In_2O_3$. Reprinted with the permission from ref. [39]. Copyright (2019) American Chemical Society

In the study of $CO_2$ hydrogenation, a high-performance $In_2O_3$-$ZrO_2$ catalyst has been developed by using monoclinic zirconia (m-$ZrO_2$) as support, compared with bulk $In_2O_3$ catalysts or $In_2O_3$-based catalysts with other carriers. $In_2O_3$-$ZrO_2$ achieved a great improvement in reactivity (5.2% of $CO_2$ conversion, 99.8% of methanol selectivity) and ensured stability for over 1000 h time-on-stream (T=300 °C, P = 5.0 MPa, $H_2$: $CO_2$ =4:1, and GHSV = 16000 $h^{-1}$). These results were attributed to the formation of epitaxially-grown $In_2O_3$ or solid $In_2O_3$-$ZrO_2$ solutions, providing the additional and/or super oxygen vacancies and thereby promoting $CO_2$ activation [36]. Later, Akkharaphatthawona et al. reported that incorporation of Ga into the crystalline lattice of $In_2O_3$ at x = 0.4 ($Ga_{0.4}In_{1.6}O_3$) remarkably boosted the methanol yield at higher reaction temperatures (340 °C –360 °C), which was related to an increase in the binding energy of the adsorbed intermediate molecules on the surface of the catalyst [40]. In order to overcome the rate-limiting of $H_2$ splitting on bulk $In_2O_3$ and further improve the reactivity, some hydrogenation metals (Pd, Au, Rh, Pt, Co, Ni) were also added as promoters into $In_2O_3$-based catalysts. Among many dopants, the Pd was embedded into the $In_2O_3$ with a low-nuclearity cluster form, that boosted the productivity of methanol without displaying the RWGS activity [41]. Considering that the CO could be present in the feedstock of $CO_2$ as an impurity or recycled byproduct from $CO_2$ hydrogenation in industry, the sensitivity of the $In_2O_3$-based catalyst to CO was also investigated in many reports [36, 42]. Co-feeding of CO seems to be beneficial to generating more oxygen vacancies *in situ* and significantly increasing the methanol yield. However, in the atmosphere of only $H_2$ and CO, the indium oxide catalyst will be completely reduced to metallic indium, resulting in complete deactivation [36]. When CO co-feeding, reached an equimolar CO to $CO_2$ ratio during $CO_2$ hydrogenation, Pérez-Ramírez et al reported that $In_2O_3$/m-$ZrO_2$ experienced an increase in methanol productivity, bulk $In_2O_3$ remained almost unaffected, but nickel-or palladium-promoted $In_2O_3$, $In_2O_3$/t-$ZrO_2$, and $In_2O_3$/$Al_2O_3$ experienced moderate to substantial deactivation. It was noted that controlling the formation of oxygen vacancies and sintering prevention are helpful for indium-based catalysts, whereas CO/$H_2O$-induced sintering and CO inhibition can attenuate the activity [42].

In summary, the methanol-mediated synthesis of light olefins from $CO_2$ combines two core reactions in one tandem system, which include the $CO_2$-to-MeOH (CTM) and the MeOH-to-olefins (MTO) process. The MTO reaction must be operated at >300 °C due to kinetic predisposition for C-C coupling. However, the CTM reaction is not thermodynamically favored at this high temperature. Increasing the temperature promotes the RWGS reaction, resulting in a large amount of water and CO, which not only reduces the yield of methanol, but also seriously affects the stability of the catalysts. Although the classic $Cu/ZnO/Al_2O_3$ catalyst has been efficiently used for methanol synthesis from syngas, it is not suitable as a methanol catalyst component for the direct $CO_2$ conversion to light olefins at an elevated temperature. The performance of $Cu/ZnO/Al_2O_3$ and other alternative catalysts have been summarized for hydrogenation of $CO_2$ to methanol (citation shown in Table 1), and it is clear that the $In_2O_3$-based catalysts are the most promising catalysts for CTM in the catalytic $CO_2$ hydrogenation to olefins system at high temperature, due to their higher methanol selectivity and stability. In this thesis, the research focuses on the activity and stability of MTO catalysts, in order to avoid the impact of the performance fluctuation of varying CTM catalysts on MTO systems, the stable bulk indium oxide catalyst was used as a fixed component to perform the CTM reaction.

**Table 1**. Qualitative comparison of different catalyst families for $CO_2$ hydrogenation to methanol. Reprinted with the permission from ref. [19]. Copyright (2022) Elsevier.

| | $Cu/ZnO/Al_2O_3$ catalyst | Other Cu-based catalysts | $In_2O_3$-based catalysts | Noble metal catalysts |
|---|---|---|---|---|
| Temperature/°C | 240-260 | 240-280 | 250-300 | 250-300 |
| Pressure/bar | 30-80 | 20-80 | 30-60 | 20-50 |
| Activity | High | High | Medium | Medium |
| RWGS activity | High | Medium | Low | High |
| By-product formation (other than CO) | Low | N/A | N/A | High |
| Thermal stability | Medium | Medium | High | N/A |
| Poisoning Resistance | Low | N/A | Low | Medium |

## 2.2 Methanol to olefins (MTO) catalyst

The methanol-to-olefins (MTO) reaction catalyzed by zeolites or zeotype catalysts is a classical process to produce light olefins in $C_1$ chemistry. The catalysts used for the MTO reaction are typically acidic zeolites (aluminosilicates) and SAPOs (silicoaluminophosphate) molecular sieves. In addition to the Brønsted acid center, co-catalytic organic substances are produced in their inorganic structure as the reaction progresses [43]. These organic substances are made of polymethylbenzenes and the attached carbenium ion, confined inside the cages of zeolites, and commonly called hydrocarbon pool species (HCPs). The corresponding reaction mechanism of methanol to olefins is called the hydrocarbon pool mechanism or double cycle mechanism (shown in Figure 4), which mainly includes an olefins cycle and an aromatics cycle [25, 26, 43, 44]. In the olefin cycle, the ethylene produced by the initial dehydration reaction is methylated to propylene and butene, then continues to grow into $C_{8+}$ chain hydrocarbons, which are finally cracked back to $C_3$ to $C_5$ olefins. In this olefin-based route, higher olefins are mainly cracked into propylene and butene, however, ethylene is only a minor cracking product of higher olefins. In addition to the olefin cycle route, the olefins can form dienes through hydrogen transfer reactions, or

olefin disproportionation reactions, or formaldehyde-assisted pathways, followed by cyclization of dienes to form aromatic species. These aromatics ($HCP_S$) can undergo isomerization and dealkylation to further co-catalyze the formation of olefins in an aromatics cycle. It has been recognized that methylbenzenes with two or three methyl groups predominantly deliver ethylene, while higher polymethylbenzenes favor the generation of propylene and butylene [44]. The types of formed polymethylbenzenes (HCPs) are strongly dependent on zeolite topology, acidity, and reaction condition [43,25, 26]. Moreover, as the reaction proceeds, the active HCPs will eventually form inactive heavy aromatics through polymerization and cyclization. These heavy polycyclic aromatics are inert, and act as coke precursors to block pores and cavities leading to catalyst deactivation. In industry applications, a SAPO-34 molecular sieve with medium acid strength is the optimal catalyst for $C_2$-$C_4$ olefins production, which typically is operated at 400-450 ℃ and 1 bar, giving high selectivity for accumulated light olefins of up to 80% in the methanol to olefins (MTO) process [25]. In order to remove the coke and recover the activity of the catalyst, a circulating fluidized bed reactor is often used to conduct continuous regeneration of the deactivated catalysts [25-26].

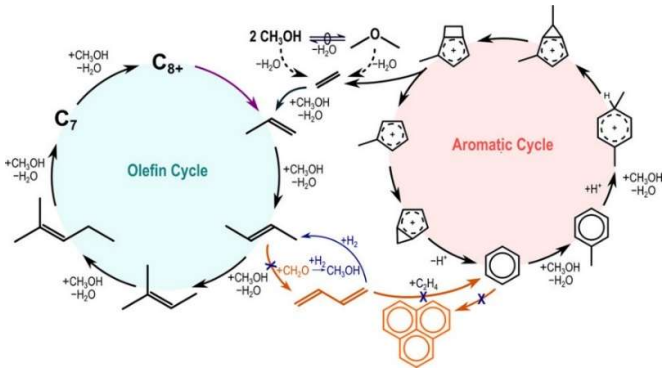


**Figure 4.** Dual Cycle Mechanism of MTO Chemistry. Reprinted with the permission from ref. [44]. Copyright (2020) American Chemical Society.

The topology and acidity of zeolites are two main important factors for the MTO reaction [26,45]. The shape/size/reactivity of HCP active intermediates are limited by the channel and cavity structures of zeolites. Through this space limitation, the MTO reaction exhibits different reaction routes and product selectivity on zeolites with different topological structures. Brønsted acidic sites are an important driving force for the MTO reaction. The acid strength, density, and their distribution in zeolites are closely related to the formation and evolution of reactive intermediates (HCPs). Therefore, the choice of topology and the adjustment of acidity are paramount to optimal catalyst performance.

Among all molecular sieve materials, zeolite/zeotype molecular sieves (SSZ-13, SAPO-34) with CHA topology have received special attention due to their high selectivity to light olefins [25,26,43,45]. These CHA zeolitic materials with elliptical cavities (10.4 × 12.0 Å) interconnected by 8-membered ring pore (3.8 × 3.8 Å) openings cause the aromatic cycle to prevail and allow only small products (3.8 Å) to escape through the pores while retaining the bulky reaction intermediates (hydrocarbon pool). Therefore, they have high selectivity to light olefins, such as ethylene and propylene [29, 43,45]. The medium-pore zeolite ZSM-5 (MFI topology, 10-membered ring) with channel dimensions of 5.3 × 5.6 Å (straight) and 5.1 × 5.5 Å (sinusoidal) allows free diffusion of larger molecules. In ZSM-5, both olefins and aromatic cycles contribute equally to olefin production. Therefore, it can produce both lower olefins and gasoline-range olefins [46]. The large-pore zeolite BEA (7.7 × 6.6 Å, 12-membered ring) can accommodate larger and more complex HCPs, which is beneficial to the propagation of both the olefin

cycle and aromatic cycle, as well as the effusion of $C_{4+}$ hydrocarbons outside the pore. Thus, its products range from $C_2$ alkanes or alkenes to $C_{12}$ aromatics, without product shape selectivity [47].

There have been many reports on the influence of acidity on the catalytic performance of zeolites [25,26,45]. It is known that an excess of Brønsted acid sites (BAS) can increase the probability of continuous reaction of products, and that high Brønsted acid strength would increase the secondary reaction rate of olefins and aromatics, further exacerbating the retention of coke precursors. Both of these conditions would accelerate coke formation, shorten the catalyst lifetime, and reduce the selectivity for light olefins. Therefore, zeolites with mild acid strength and relatively low acid density are preferred in the MTO reaction [26,45]. In a comparison of a silicoaluminophosphate molecular sieve (SAPO-34) and its aluminosilicate homologue (SSZ-13) with the same CHA topology, it has been shown that the SSZ-13 displays higher acid strength than SAPO-34. The high strength acidity has a significant influence on the reaction rates, enhancing the rate of olefin production and deposition of aromatics inside the pores of catalysts. Thus, SSZ-13 has a lower optimum operating temperature, but has a lower coking resistance compared with its SAPO-34 counterpart [32]. In addition, the BAS density and strength also affects the reaction routes [26]. For a nonacidic AlPO-18 catalyst, the methanol conversion was very low, and the reaction mainly followed the olefinic route. After the introduction of Si to generate Brønsted acid centers, the aromatics cycle pathway began to appear over SAPO-18. The higher BAS density of the catalyst, the aromatics route is more dominant in the MTO reaction to produce olefins [48]. Similar results were also confirmed in the MTO reaction catalyzed by SAPO-34. Over the low-silicon SAPO-34 with lower BAS density, the olefin route was dominant, and the ratio of propylene to ethylene was high. When the BAS density was increased, the proportion of ethylene increased. Further increasing BAS density accelerated the formation of coke species, such as polycyclic aromatics, thereby shortening the life of the catalyst. [49].

Simultaneous changes in the structure and acidic properties have also been reported to lead to different product distributions and preferential reaction routes, such as pre-coking [50], metal ion exchange [51-53], or by isomorphic substitution of T atoms in the framework [53]. SAPO-34, with a certain amount of coke deposition, exhibits a more obvious product shape selectivity than compared to when it is fresh, and displays an increasing ethylene selectivity with increased TOS (time-on-stream) due to enhanced aromatic cycle routes and shape selectivity [25,50]. Incorporation of $Zn^{2+}$ ions into the cation position of the framework of SAPO-34 by ion exchange, can decrease the BAS density and create extra diffusion limitations for hydrocarbons. It has resulted in higher ethylene selectivity and a higher ethylene-to-propene ratio than its un-exchanged counterpart [51-52]. However, the modification of the ZSM-5 zeolite by alkali metal ions had the opposite effect, where the modified ZSM-5 gave an increased selectivity for propene and decreased selectivity for alkanes and aromatics. This can be attributed to the depression of the H-transfer reaction, which decreased the aromatic cycle, and improved the olefin-based route to produce propene and higher olefins [53]. In addition to the topology and acidity of zeolite, lattice defects, and crystal size/morphology also affect the performance of MTO catalysts [54]. Moreover, reaction conditions such as reaction temperature [25], methanol partial pressure, and contact time [55] are also crucial for catalytic performance.

At approximately the same time as the development of catalysts for hydrogenation of $CO_2$ or CO to light olefins, a breakthrough in the MTO process was the discovery of the effect of co-feeding high-pressure hydrogen with methanol for improving the stability of MTO catalysts [28-29]. It was believed that the hydrogen participated in the hydrogen transfer reaction, blocking the pathways for formation of coke inside the zeolite cavities. The hydrogenation of coke precursors such as formaldehyde and 1,3 butadiene can suppress the formation of non-reactive polycyclic aromatics, thereby improving catalyst lifetime [44]. In the case of co-feeding methanol with hydrogen (0.13 bar $CH_3OH$, 4-30 bar $H_2$, 400 °C),

using a similar environment as methanol conversion in the $CO_2$ hydrogenation process, it has been reported that the lifetime (measured by turnover number) of SAPO-34 was improved by 3 to 70 times, without significantly decreasing the selectivity for light olefins [28]. Shi and colleagues studied the effect of acid strength on the MTO reaction, or on the hydrogen co-feeding MTO reaction, with the comparison of SSZ-13 and SAPO-34. It was found that the acid strength of the proton plays a key role in affecting catalyst lifetime and product selectivity in the MTO process. The shorter lifetime and lower olefin-to-paraffin ratio over SSZ-13 zeolite were attributed to its faster formaldehyde formation, hydrogen transfer, and subsequent alkylation reactions to form inert polycyclic aromatics on the high-strength Brønsted acidic sites. However, compared with SAPO-34, SSZ-13 achieved a longer lifetime and higher alkane selectivity in the reaction of co-feeding with MTO due to the faster hydrogenation rate of formaldehyde, dienes, and alkenes on the same Brønsted acidic sites [29]. The observed increases in the selectivity for $C_2$-$C_4$ alkane are also dependent on the zeolite typology. Alkane selectivity increased equally among zeolites with CHA, BEA, and FER topology, however, the zeolite with AEI structure exhibited a higher selectivity for propane than selectivity for $C_2$ or $C_4$ alkanes. This indicates that the zeolite topology also plays a role in the hydrogenation [44,56]. Catalyst life can be further improved by combining co-feeding of high-pressure water and $H_2$. Zhao et al. reported a synergistic effect of water and hydrogen in improving the lifetime of SAPO-34. Compared with co-feeding high-pressure hydrogen (4.2 bar $CH_3OH$, 35.7 bar $H_2$, 450 ℃), co-feeding the medial pressure of hydrogen and water (4.2 bar $CH_3OH$, 12.8 bar $H_2$, 22.8 bar $H_2O$, 450 ℃) is more conducive to prolonging the catalyst life and improving the selectivity for light olefins (propylene). Unfortunately, under high-pressure conditions, either in $H_2$ or $H_2$ and $H_2O$ co-feeding, the framework of SAPO-34 suffers from damage due to steam dealumination [30].

Currently, more than 90% of proposed tandem catalysts [22,23,57-65] (shown in Table 2) use SAPO-34 as an effective component for converting methanol to olefins in the $CO_2$ to olefins process. However, due to its severe instability in hydrothermal environments, there is an urgent need to explore an alternative catalyst component with high hydrothermal stability to conduct the MTO reaction during $CO_2$ hydrogenation. SSZ-13, a zeolitic homologue of the SAPO-34 molecular sieve with attractive hydrothermal stability and strong acidity, has been widely used for the selective reduction of $NO_x$($deNO_x$) [31]. With the same topology and similar pore size as SAPO-34, SSZ-13 was considered the best potential substitute for a SAPO-34 zeolite among all catalysts for the MTO reaction [25,26, 32, 45]. However, in a pure MTO reaction it has exhibited low coking resistance and a fast deactivation rate, due to the higher hydrogen transfer activity on its strong acidic sites, compared with its SAPO-34 counterpart [32, 66]. It has also performed poorly in early reports regarding the tandem catalytic system for $CO_2$ hydrogenation, because its strong acidity enabled further hydrogenation of olefins, leading to higher selectivity for paraffins in the products [56,67].

The acidic strength is broadly defined as the ease with which an acid loses $H^+$ to a base. Previous theoretical simulations indicated that proton affinity of an SSZ-13 zeolite is independent of either acid amount or location of tetrahedral Al in the zeolite framework, within a certain Si/Al range. Thus, even dealumination was not useful to alleviate its rapid deactivation in the MTO reaction [68]. However, lots of recent reports have confirmed that the proximity of the protonic acid (proton location) affects the performance of the MTO reaction over the SSZ-13 zeolite [69-70]. R. Gounder et al. confirmed that the rate of constant methanol dehydration for paired proton sites was 10 times higher than for isolated proton sites [69]. Davis, M.E. et al. found that the higher proportion of paired Al sites in the framework of SSZ-13 was responsible for hydrogen transfer reaction in pure MTO reactions. Neutralizing these paired proton sites by an ion exchange of $Cu^{2+}$ ions or reducing the pair proton sites by increasing the Si/Al ratio, the hydrogen transfer reaction can be significantly suppressed, and the lifetime of the SSZ-13 can be improved [66]. Similar reports also found that the SSZ-13 zeolite with a low proportion of $Q^4$(2Al)

[Si $(OSi)_2(OAl)_2$] structure in the framework showed a longer catalytic life in MTO reactions [70]. Over the ZnCrOx/SSZ13 tandem catalyst, Huang et al. found that increasing the Si/Al ratio of SSZ-13 can increase the selectivity for light olefins during the hydrogenation of syngas [71].

So far, in the practice of $CO_2$ hydrogenation to light olefins via methanol routes, the ideal zeolite component for high-performance tandem catalysts has not been found. How to develop a zeolite with high selectivity toward light olefins, while maintaining high stability, is an urgent task to be solved. Furthermore, in a tandem system, the MTO reaction is carried out under the co-feeding of methanol, hydrogen, water, carbon monoxide, and carbon dioxide. The effects of zeolite acid properties (acid density, acid strength, and acid distribution) on the selectivity of light olefins and coke deposition become more complicated. It is also necessary to distinguish which type of acid properties has the most significant influence.

.

**Table 2.** Catalytic Performance towards $CO_2$ hydrogenation to lower olefins (Tandem Catalysts).

| Catalysts | Temp | Press | GHSV | $X_{CO2}$ | Hydrocarbon product distribution (mol%) | | | | Sel.CO | Sel.CH | TOS | Ref. |
|---|---|---|---|---|---|---|---|---|---|---|---|---|
| | /°C | /bar | /mL*g$^{-1}$*h$^{-1}$ | /% | $CH_4$ | $C_2^0$-$C_4^0$ | $C_2^=$-$C_4^=$ | $C_{5+}$ | /% | /% | /h | |
| ZnZrO/SAPO-34 | 380 | 20 | 3600 | 12.6 | 3 | 14 | 80 | 3 | 47 | NA | 50 | [22] |
| $ZnGA_2O_4$/SAPO-34 | 370 | 30 | 5400 | 13.6 | NA | 8 | 88 | 2 | 49 | 51 | 10 | [23] |
| ZnAlOx/HZSM-5 | 320 | 30 | 2000 | 9.1 | 0.5 | 6.7 | 10.7 | 80.3 | 57.4 | 42.6 | NA | [57] |
| ZnZrO/HZSM-5 | 320 | 40 | 1200 | NA | 0.3 | 14.5 | 4.9 | 80.3 | 43.7 | 57.3 | NA | [58] |
| NiCu/$CeO_2$-SAPO-34 | 375 | 20 | 12000 | 17 | 2.1 | 16.7 | 78 | 3.2 | 64.2 | 35.8 | 10 | [59] |
| $In_2O_3$/SAPO-34 | 360 | 25 | 6000 | 28.2 | 5 | 18 | 70 | 2.3 | NA | NA | NA | [60] |
| $In_2O_3$/SAPO-34 | 380 | 30 | 9000 | 15.3 | 2.7 | 13.7 | 81.9 | 1.7 | 68.3 | 31.7 | 10 | [61] |
| In-Zr(4:1)/SAPO-34 | 380 | 30 | 9000 | 26.2 | 2 | 21.5 | 74.5 | 2 | 63.9 | 36.1 | 10 | [61] |
| $In_2O_3$-ZnZr-SAPO-34-S-a | 380 | 30 | 9000 | 17 | 1.6 | 11.1 | 85 | 2.3 | 55.8 | NA | 50 | [61] |
| $ZnAl_2O_4$/SAPO-34 | 370 | 30 | 5400 | 15 | 0.7 | 10 | 87 | 2.2 | 49 | 51 | 10 | [62] |
| $MgAl_2O_4$/SAPO-34 | 370 | 30 | 5400 | 8.7 | 1.9 | 25 | 65 | 8 | 96 | 4 | 10 | [62] |
| (CuO–ZnO)–Kaolin/SAPO-34 | 400 | 30 | 1800 | 50.4 | 13.6 | 15.8 | 70.6 | 0 | 7.5 | NA | NA | [63] |
| CuO-ZnO-$Al_2O_3$/SAPO | 400 | 30 | 1800 | NA | 10 | 25 | 62 | na | 3 | NA | NA | [64] |
| CuZnZr@Zn–SAPO-34 | 400 | 20 | 3000 | 19.4 | 14.6 | 20.2 | 60.5 | 4.8 | 58.6 | 41.4 | 24 | [65] |
| CuZnZr–SAPO-34 | 400 | 20 | 3000 | 12.6 | 8.8 | 45.7 | 42.5 | na | 56.7 | 43.3 | 24 | [65] |

Note: $H_2/CO_2$ = 3; NA = not available; TOS = Time-on-stream. Hydrocarbon production distribution doesn't take into account of CO, methanol and dimethyl ether.

## 2.3 The synergy between CTM and MTO catalysts

As mentioned above, the $In_2O_3$-based CMT catalyst can exhibit excellent performance for methanol synthesis in the temperature range of 250-300 ℃. The higher temperature is more favorable for the RWGS reaction, resulting in higher CO selectivity [17-21]. However, the optimum reaction temperature for the conventional MTO reaction is between 400-450 ℃, based on the SAPO-34 zeolite [25]. It has been found that the formation of C-C bonds is favored at high temperatures: when the MTO reaction is carried out at 250 °C, no methanol conversion occurs, only methanol and dimethyl ether appear in the effluent until the temperature gradually increases to 300 °C. In addition, the higher (>500 °C) and lower temperature (< 400 °C) reactions also present higher coking rates than the reactions performed under mild reaction conditions (400−450 °C). The extremely high coking rate at low reaction temperatures corresponds to rapid deactivation during methanol conversion, which is mainly due to the formation and accommodation of inert adamantanes in the catalyst [25,72]. A similar result was found in the MTO reaction with co-feeding of $H_2$ (4.0 MPa, $H_2$/MEOH/$H_2O$/$N_2$ = 3/1/2.67/2.66, SAPO-34). The reactions at 375 °C and 400 °C displayed an extremely short lifetime of less than 1 h, and many adamantanes were found in the spent catalysts, which block the channels, increase mass transfer resistance, and thus, cause fast deactivation [30]. In addition to temperature, pressure is also an important process parameter affecting product distribution and catalyst stability. High pressure facilitates the synthesis of methanol in the CTM reaction. However, high methanol partial pressure enhances the relative rate of methanol disproportionation to release formaldehyde, the concentration of which can accelerate the deactivation of the hydrocarbon pool and shorten the lifetime of SSZ-13 zeolite during the MTO reaction [54]. Nieskens et al. compared the deposition of coke with the lifetime between methanol-mediated syngas to hydrocarbon and the MTO process. The result indicated that the lower hydrogen pressure and higher methanol partial pressure can contribute to the formation of coke, which, in turn, causes catalysts to deactivate severely [73]. Therefore, the coupling of the CTM and MTO processes, so that good product selectivity and lifetime can be achieved under common conditions, is a notable challenge.

Although it is difficult to reconcile the optimal conditions required for these two reactions, there is a synergy between them. After mixing the two catalysts (CTM and MTO catalysts) into a tandem catalyst, these bifunctional tandem catalysts exhibited reduced selectivity for CO and increased conversion of $CO_2$. When compared to the sole CTM catalyst, the rapid conversion of methanol/DME to form lower olefins, was deemed to be the thermodynamic driving force to shift the methanol synthesis equilibrium towards products, and thus, suppress the parallel RWGS reaction [27]. In order to reduce the mass transfer resistance and further enhance the synergistic effect of the two catalysts, the integration of two catalyst components with different proximity has been extensively investigated, including a double bed mode, granule mixing (500-800 μm) mode, and powder mixing (0.5-1μm) modes [24]. Recent studies have found that too close contact (powder mixture) leads to the migration of some metal ions, from the CTM catalyst (oxides) to the MTO catalyst (ZSM-5 zeolites or SAPO-34), through solid-state ion exchange during $CO_2$ hydrogenation. Thereby, the performance of the zeolite catalyst is affected, and can even experience deactivation. Among these active metal oxide catalysts, indium oxide-based and zinc oxide-based catalysts are included [74-75].

In this work, indium oxide has been used as the CTM catalyst. In order to avoid the migration of indium ions into the zeolite catalyst, thereby reducing the interference of indium ions on the performance test of zeolites, the indium oxide and zeolite catalyst are combined in a tandem system by granular mixing.

# 3 Experimental

In this chapter, the techniques and methodologies related to the synthesis, characterization, and activity testing of catalysts are introduced.

## 3.1 Catalyst preparation

### 3.1.1 Synthesis of bulk $In_2O_3$

The CTM ($CO_2$ to methanol) catalyst used in **Paper I** and **Paper II** was bulk $In_2O_3$, which was prepared using the conventional co-precipitation method [76]. A 6.5 wt. % of indium (III) nitrate aqueous solution was used as the metal source, and a sodium carbonate solution (9.1 wt.% of $Na_2CO_3$ in water) was used as a precipitant. The precipitant was gradually added dropwise to the indium nitrate solution, under magnetic stirring, and at room temperature until the pH reached 9.2. After aging for 1 hour, the resulting mixture was filtered and subsequently washed with deionized water to dispose of $Na^+$. The final precipitate was dried in a vacuum oven overnight at 60 ℃, then calcined at 400 ℃ for 3 h to obtain the bulk $In_2O_3$ catalyst.

### 3.1.2 Synthesis of SSZ-13 zeolite with different Al distributions

As the key catalyst for the MTO reaction in the $CO_2$ hydrogenation to olefins process, SSZ-13 zeolites with different Al distributions were synthesized and studied in detail in **Paper I**. These zeolite samples, with paired Al or isolated Al distributions, were synthesized under hydrothermal conditions. The difference between them were the different compositions of gel precursors, silicon sources, and crystallization time, as shown in Table 3.

**Table 3.** Precursors, silicon sources, and crystallization conditions of synthesized zeolite samples

| Sample name | Si/Al in gel | Gel precursors composition ($SiO_2/Al_2O_3/TMAdaOH/Na_2O/H_2O$) | Silicon sources | Crystallization time (h) |
|---|---|---|---|---|
| H-PAR-15 | 15 | 100: 3.3: 20: 10: 4000 | fumed silica | 96[66] |
| H-PAR-20 | 20 | 100: 2.5: 20: 10: 4000 | fumed silica | 96[66] |
| H-PAR-25 | 25 | 100: 2.0: 20: 10: 4000 | fumed silica | 96[66] |
| H-ISO-15 | 15 | 100: 3.3: 20: 0: 4000 | silica sol | 144[77] |
| H-ISO-20 | 20 | 100: 2.5: 20: 0: 4000 | silica sol | 144[77] |
| H-ISO-25 | 25 | 100: 2.0: 20: 0: 4000 | silica sol | 144[77] |

The N, N, N-trimethyl-1-adamantylammonium hydroxide (TMAdaOH, 25 wt.%, Tokyo Chemical Industry Co. Ltd.) was used as the organic structure-directing agent (SDA) during the hydrothermal crystallization. The fumed silica (fumed powder, 99.8% of $SiO_2$, Sigma-Aldrich), or silica sol (LUDOX® AS-40, 40 wt.% of $SiO_2$), were utilized as the precursors of Si. The aluminum hydroxide (Sigma Aldrich, Al $(OH)_3$ > 99%) was used as the Al source. The SSZ-13 zeolite with an isolated Al distribution was prepared by using only the organic SDA ($TMAda^+$) [77], while the SSZ-13 zeolite with a paired Al distribution was synthesized in a hydroxide media from a gel precursor, which includes both organic ($TMAda^+$) and inorganic cations ($Na^+$) as SDAs [66].

Specifically, in the synthetic procedure of SSZ-13 with paired Al sites, a gel precursor was first prepared according to the detailed composition (Table 3). Next, the gel was transferred to a Teflon-lined stainless-steel autoclave and kept at 160 ℃ for 96 h under rotation. After crystallization, washing, and drying,

the calcination occurred at 600 ℃ for 8 h under flowing air. Then, the sodium type SSZ-13 was obtained and named as Na-PAR-x, where 'x' represents the molar ratio of Si/Al derived from the designed formulation. Afterward, the ion exchange treatment of Na-PAR-x was carried out at 80 ℃, by using 2.5 M $NH_4NO_3$ aqueous solution, and repeated twice in order to obtain the $NH_4$-typed SSZ-13 zeolite samples. After drying and calcination at 550 ℃ for 4 h in static air, the final proton-typed SSZ-13 zeolite with paired Al distribution was obtained, and designated as H-PAR-x. In the synthesis of SSZ-13 zeolite with only isolated Al sites, the pre-prepared gel was placed in a 160 mL Teflon-lined stainless-steel autoclave and heated at 160 ℃ for 6 d of crystallization, with constant rotation. The resulting zeolite was filtered, washed, and then dried at 110 ℃ overnight. After subsequent calcination at 600 ℃ for 8 h under flowing air to remove the residual SDA, the protonated SSZ-13 zeolite with an isolated Al distribution was denoted as H-ISO-x, where 'x' represents the molar ratio of Si/Al from the designated formulation. The as-synthesized fresh zeolite, before the removal of SDA, was named as TEA-ISO-x.

The $Co^{2+}$ cation exchange experiments and associated characterization (Ultraviolet-visible spectroscopy) were used to identify whether there are paired Al sites (proton pairs) inside the two proton-types SSZ-13 zeolites, and the saturated $Co^{2+}$ exchange capacity was used to quantify the content of Al sites (proton pairs) [77-79]. Before characterization, the proton-type zeolite samples were subjected to $Co^{2+}$ ion exchange followed by rehydration [78]. Firstly, 1g of proton-type SSZ-13 zeolite powder was mixed with 150 ml of 0.5 M cobalt (II) nitrate (Sigma Aldrich, ≥98%) solution under stirring. After sufficient ion exchange at 80 ℃ for 48 h, the solid was collected and washed 4 times with deionized water, then the resulting sample was dried overnight at 110 ℃ and calcined at 500 ℃ for 1 h in static air. After that, the sample was immersed in an equal volume of deionized water for 1 h, and then dried at 100 °C for 3 h to achieve rehydration. The final obtained sample was denoted as Co-ISO-x or Co-PAR-x respectively, where 'x' represents the molar ratio of Si/Al derived from the designated formulation, as above.

The Cobalt cation exchange capacity was calculated based on the mole ratio of Co to 2Al ($n_{Co}/n_{2Al}$) inside the Co-exchanged samples. The concentration of Co and Al was obtained from the elemental analysis results.

### 3.1.3 Synthesis of $Na^+$-exchanged SSZ-13 zeolite

In **Paper I**, to study the effect of the acid density of SSZ-13 zeolite on the catalytic performance, based on sample H-ISO-15 as the parent material, lower acidic samples with varying acid densities were prepared by sodium ion exchange. Specifically, 3 g of H-ISO-15 zeolite sample was ion-exchanged with 300 ml of $NaNO_3$ (Sigma Aldrich, > 99%) solution for 24 h at 25 ℃, under stirring. The ion exchange treatment was carried out once without controlling the pH of the solution. The degree of ion exchange was controlled by changing the concentration of the sodium ions in the solution (molarity of sodium ion ranges from 0.033 to 2 mol/L) with other parameters fixed. After ion-exchange, the zeolite slurry was filtered, washed three times with deionized water, and subsequently dried at 110 ℃ overnight. After calcination at 550 ℃ for 4 h in static air, the obtained sample was denoted as Na-y-ISO-15, where 'ISO-15' represents the parent material, 'y%' indicates the degree of exchange by Na, which was determined from the molar ratio of incorporated Na to Al from composition analysis.

### 3.1.4 Preparation of tandem catalysts

The powders of $In_2O_3$ and SSZ-13 samples were pressed into large pellets (20 mm pellet die, 2.5 tons of pressure), then crushed, and sieved into granules using the size 250 μm-500 μm. Thereafter, the tandem catalysts were prepared by physically mixing granules of the $In_2O_3$ oxide and SSZ-13 zeolite. these two granular components were mixed homogeneously by being shaken in a glass vessel. The weight ratio of the $In_2O_3$ oxide and SSZ-13 zeolite components was fixed at 2:1.

In **Paper I**, the tandem catalysts denoted as M / H-ISO-x, M / H-PAR-x, or M / Na-y-ISO-15 were composed of bulk $In_2O_3$ (M), and the samples H-ISO-x, H-PAR-x, or Na-y-ISO-15 respectively. In order to be compared with the tandem catalysts, the same amount of indium oxide catalyst was mixed with inert silicon carbide to form the pure indium oxide catalyst, denoted as M($In_2O_3$). In **Paper II**, the tandem catalysts named as $In_2O_3$/ SSZ-13-x, were made of bulk $In_2O_3$ and H-ISO-x. In this thesis, $In_2O_3$/ SSZ-13-x will be represented by M/H-ISO-x (**Paper I** notation) to maintain a consistent narrative.

## 3.2 Characterization of fresh catalysts and individual components

### 3.2.1 Powder diffraction (XRD)

The X-ray diffraction pattern of zeolite and oxide samples were measured by using a Bruker D8 X-ray diffractometer with a CuKα (λ=1.54Å) radiation source. The diffraction angles (2θ) were scanned from 5 to 55°, with a step size of 0 to 029°, and dwell time of 1s. Relative crystallinity (RC) was calculated using the equation : $RC_x = \sum I_x / \sum I_0 \times 100\%$, where $\sum I_x$ is the sum of the XRD diffraction peak intensities of sample x, at 2θ = 9.6°, and 20.9°; and where $\sum I_0$ is the sum of the XRD diffraction peak intensities of sample H-PAR-15, at 2θ = 9.6°, and 20.9°.

### 3.2.2 Elemental analysis (ICP&XRF)

The elemental composition (Si, Al, and Na) of all samples was measured on an Axios wavelength dispersive X-ray fluorescence (XRF) spectrometer (Zetium, Malvern-Panalytical), employing an Rh anode as the X-ray source. The cobalt loading in the $Co^{2+}$-exchanged sample was determined via inductively coupled plasma sector filed mass spectrometry (ICP-SFMS), in the lab of ALS Scandinavia AB (Luleå, Sweden).

### 3.2.3 Scanning electron Microscope (SEM)

The scanning electron microscope (SEM) was employed to identify the crystal morphology of zeolite samples. The instrument used was a JEOL JSM-7800F scanning electron microscope with an energy dispersive X-ray system.

### 3.2.4 $N_2$ adsorption

The textural properties (specific surface area and pore volume) of samples were determined by $N_2$ adsorption at -196 ℃ on a Micromeritics Tri-Star 3000 instrument. Samples were degassed at 300 ℃ for 6 h prior to measurements. The total surface area was determined using the Brunauer-Emmett-Teller (BET) equation, based on fitting the data in the relative pressure ($P/P_0$) range from 0.005 to 0.05. The micropore and mesopore volumes were measured from the $N_2$ adsorption isotherm using the t-plot and the BJH methods respectively.

### 3.2.5 Magic angle spinning nuclear magnetic resonance (MAS NMR)

To investigate the information related to the framework of the zeolite samples, the $^{27}Al$ and $^{29}Si$ magic angle spinning nuclear magnetic resonance (MAS NMR) experiments were carried out on a Bruker Avance III 500MHZ magnet spectrometer equipped with a 4 mm double-resonance MAS probe. The $^{27}Al$ MAS NMR single pulse spectra with high power decoupling spectra (hpdec) were recorded at 130.3 MHz with a MAS spinning rate of 11 kHz. The single pulse $^{29}Si$ MAS NMR spectra were acquired at 99.4 MHz with a MAS spinning rate of 11 kHz. The $^{29}Si$ cross-polarization (CP) MAS NMR spectra were collected by employing a cross-polarization pulse sequence with 5 ms of contact time and 2 s of recycle delay. All chemical shifts were referenced externally to the methylene ($-CH_2-$) group of adamantane set to 38.48 ppm (with sr =0). The framework Si/Al ratio of the zeolite sample was estimated by using the reported equation [71, 78]:

$$\frac{Si}{Al} = \frac{\sum_n^4 I_{Q4(nAl)}}{I_{Q4(4Al)} + 0.75 * I_{Q4(3Al)} + 0.5 * I_{Q4(2Al)} + 0.25 * I_{Q4(1Al)}}$$

Where n is the number of O-Al binding with Si, and the $I_{Q4(nAl)}$ is the integrated peak area from the $^{29}$Si MAS NMR spectra, corresponding to each Si with different $Q^4$(nAl) [Si $(OSi)_{4-n}(OAl)_n$] coordinations.

### 3.2.6 Ultraviolet-visible spectroscopy (UV-Vis)

Ultraviolet-visible spectroscopy (UV-Vis) was used to determine the chemical state of $Co^{2+}$, and to detect the presence of $Co^{2+}$ on paired Al sites of Co-exchanged SSZ-13 zeolite samples. The UV-Vis diffuse reflectance (DRS UV-vis) spectra were collected on a LAMBDA 365 UV-Vis Spectrophotometer (PerkinElmer), attached with an integrating reflectance sphere accessory (50 mm). The baseline of the spectra was recorded by using the $BaSO_4$ (Sigma Aldrich, ≥98%) as a 100% reference. Then, the sample spectra were collected from 10000 to 40000 $cm^{-1}$ at a scan rate of 240 $cm^{-1}$/s. The diffuse reflectance was transformed into absorption intensity by using the Schuster-Kubelka-Munk equation [79]: $F(R_\infty) = (1 - R_\infty)^2/2R_\infty$, where $R_\infty$ is the diffuse reflectance from a semi-infinite layer.

### 3.2.7 Diffuse reflectance infrared Fourier transform spectroscopy (DRIFTS)

Diffuse reflectance infrared Fourier transform spectroscopy (DRIFTS) was employed to investigate the acid properties (information on acidic hydroxyl groups, and chemisorbed species on the surface) of zeolite samples. The DRIFTS spectra were acquired on an FT-IR spectrometer (Vertex 70, Bruker) equipped with a diffuse reflectance accessory (Thermo Scientific™). Before measurement, the sample surface was cleaned by pretreating at 550 °C for 60 min under 100 Nml/min of Ar flow, then cooled down to 30 ℃ under Ar flow for spectra acquisition. After obtaining the spectra of the surface hydroxyl groups, the baseline spectra were collected based on the clean surface, thereafter, 1000 ppm of continuous $NH_3$/Ar flow (100 NmL/min) was then dosed gradually into the cell while the synchronous adsorption spectra were recorded in the range of 4000-1000 $cm^{-1}$ with a resolution of 4 $cm^{-1}$ until the sample reached saturation. the outlet streams were recorded by an on-line mass spectrometer (Hiden HR20). After adsorption at 30 ℃, the sample was heated to 200 ℃ under Ar flow for desorption and then cooled down to 30 ℃ for spectra collection.

### 3.2.8 Temperature-programmed desorption of ammonia ($NH_3$-TPD)

A temperature-programmed desorption of ammonia ($NH_3$-TPD) experiment was carried out to quantify the acidity of zeolite samples. On a calorimeter (Sensys DSC, SETARAM), coupled with a mass spectrometer (HPR-20 QUI, Hiden), 30 mg of a granular sample (250 -500 μm) was pretreated at 550 ℃ for 1 h, followed by cooling to 100 ℃ in flowing Ar (500 Nml/min). Then, the sample was exposed to a 2000 ppm of $NH_3$/Ar gas flow (20 Nml/min) for 2 h until the sample was saturated with $NH_3$, after which it was flushed with Ar (20 Nml/min) for 4 h to remove the physisorbed $NH_3$. Finally, the desorption of $NH_3$ was carried out by increasing the temperature from 100 ℃ to 700 ℃ with a ramping rate of 10 ℃/min under a pure Ar (20 Nml/min) flow. The desorbed $NH_3$ was monitored by an online mass spectrometry, where the concentration of $NH_3$ was recorded at the characteristic mass to charge ratio (m/z) of 17. The MS signals were calibrated prior to the experiment using gas mixtures of known composition. The Brønsted acid density assessed from the deconvolution peaks of the $NH_3$- TPD curve with centers ranging from 300 ℃ to 700 ℃.

## 3.3 Catalytic performance test and in situ pre-coking treatment

### 3.3.1 Catalytic performance test

The catalytic reaction test and the *in situ* pre-coking treatments were carried out in a stainless-steel fixed bed reactor (VINCI Technologies, France) with an inner diameter of 8.3 mm and a length of 215 mm. Before reaction, 1 g of well-mixed tandem catalyst was placed in the isothermal zone of the reactor tube. The empty volumes at the top and bottom of the reactor tube were filled with silicon carbide (Sigma Aldrich, 500 μm), and the interfaces between the silicon carbide and catalyst were separated by quartz wool plugs. The reaction temperature was monitored by a K-type thermocouple with its tips positioned in the center of the catalyst bed. The reaction pressure was controlled automatically by a pneumatic back pressure valve, and the feeds of reactant gases were precisely controlled by mass flow meters.

In **Paper I**, the catalytic performance of different catalysts was evaluated under fixed reaction conditions. Specifically, the tandem catalysts were pretreated under Argon flow, (150 Nml/min) at 400 ℃ for 1 hour at ambient pressure prior to the reaction. After the catalysts were cooled down to 325 ℃ in pure Ar, the Ar flow was stopped, and the reactant gases were introduced into the reactor with a $H_2/CO_2$ ratio of 6:1, and an hourly space velocity (GHSV) of 6400 $mL*g^{-1}*h^{-1}$. When the reaction pressure rose to 10 bar, the reaction started, and the online analysis of all gaseous products was carried out simultaneously.

In **Paper II**, the reaction tests were investigated under varying reaction parameters. In the case of fresh tandem catalysts, these were first pre-treated at 400 ℃, for 1 hour, in a pure Ar flow (150 Nml/min), then cooled down to the desired reaction temperature (325-400 ℃). Thereafter, the reactant gases with the set feed ratio of $H_2/CO_2$ (2.5:1 to 6:1), were introduced into the reactor at a fixed total gas hourly space velocity (GHSV) of 6400 $mL*g^{-1}*h^{-1}$. The reaction results were recorded after the pressure reached its setpoint value (10 bar to 40 bar). For the tandem catalysts, after *in situ* pre-coking, reaction tests were switched directly to the target pressure and temperature without the need for argon pre-treatment.

### 3.3.2 The in-situ pre-coking treatment

In **Paper II**, the *In situ* pre-coking refers to the modification of the catalyst, with coke, by applying a transient temperature treatment of the catalyst. When the fresh tandem catalysts had reached 400 ℃ under atmospheric pressure in Ar, a mixture of $CO_2$ (15.2 Nml/min) and $H_2$ (91.4 Nml/min) gases were fed into the reactor at a total pressure of 30 bar and kept constant during the whole treatment. Firstly, the initial treatment (30 bar, 400 ℃) was maintained for 0 or 5 h. Then the temperature was decreased to 325 ℃ and a second stage treatment was conducted (30 bar, 325 ℃) for 10 to 20 h. Finally, the temperature was increased to 400 ℃ at 30 bar under the fixed reactants atmosphere, followed by 5 h dwelling time to complete one cycle of a pre-coking treatment.

### 3.3.3 Product analysis

All gaseous products from the reaction were analyzed using an online gas chromatograph (GC-456, Bruker). This GC was equipped with a thermal conductivity detector for the detection of permanent gases and methanol, and a flame ionization detector for the analysis of hydrocarbons. The identification of each gaseous compound ($CO_2$, CO, $CH_4$, $CH_3OH$, DME and $C_1$ to $C_7$ hydrocarbons) was performed based on their retention times. The quantification was done by integrating the peak areas and using the calibration factors acquired from gas calibration standards (Linde Gas). The $CO_2$ conversion, the selectivity or yield of CO and methanol, and the selectivity of individual hydrocarbon products, excluding CO, were calculated according to these equations:

$CO_2$ conversion: $\mathrm{Conv.CO_2} = \left(n_{\mathrm{CO_2},in} - n_{\mathrm{CO_2},out}\right)/\, n_{\mathrm{CO_2},in} \times 100\%$

CO selectivity: $\mathrm{Sel.CO} = n_{\mathrm{CO}} \,/\, \left(n_{\mathrm{CO_2},in} - n_{\mathrm{CO_2},out}\right) \times 100\%$

$CH_3OH$ selectivity: $\mathrm{Sel.MeOH} = n_{\mathrm{MeOH}} \,/\, \left(n_{\mathrm{CO_2},in} - n_{\mathrm{CO_2},out}\right) \times 100\%$

Dimethyl ether (DME) selectivity: $\mathrm{Sel.DME} = 2 * n_{\mathrm{DME}} \,/\, \left(n_{\mathrm{CO_2},in} - n_{\mathrm{CO_2},out}\right) \times 100\%$

$C_nH_m$ selectivity among hydrocarbons excluding CO, $CH_3OH$ and DME:

$\mathrm{Sel.C_nH_m} = n * n_{\mathrm{C_nH_m}} \,/\, \left(n_{\mathrm{CO_2},in} - n_{\mathrm{CO_2},out} - n_{\mathrm{CO}} - n_{\mathrm{MeOH}} - 2 \times n_{\mathrm{DME}}\right) \times 100\%$

Yield of $CH_3OH$ in effluent: $\mathrm{Yield\ MeOH} = \left(n_{\mathrm{MeOH}} \,/ n_{\mathrm{CO_2},in}\right) \times 100\%$

Yield of $C_nH_m$ in effluent: $\mathrm{Yield\ C_nH_m} = n * \left(n_{\mathrm{C_nH_m}} \,/ n_{\mathrm{CO_2},in}\right) \times 100\%$

where $n_{\mathrm{CO_2},in}$ refers to the mole of $CO_2$ at the inlet, and $n_{\mathrm{CO_2},out}$, $n_{\mathrm{CO}}$, $n_{\mathrm{MeOH}}$, $n_{\mathrm{DME}}$, $n_{\mathrm{C_nH_m}}$ represents the moles of the $CO_2$, CO, $CH_3OH$, DME, and individual hydrocarbons at the outlet, respectively. Here the $n_{\mathrm{CH_4}}$, $n_{C_n^0}$, and $n_{C_n^=}$ indicates the moles of methane, paraffin, and olefin respectively.

## 3.4 Analysis of coke species inside the spent catalyst

After the reaction, the spent catalyst was purged using argon overnight, then taken out and ground into a uniform powder for analysis.

### 3.4.1 Thermogravimetric analysis (TGA)

Thermogravimetric analysis (TGA) was conducted in order to obtain the content of the retained coke inside the catalysts. On a Thermal Analysis System TGA/ DSC 3+ (Mettler Toledo), 10 mg of spent catalyst was heated to 700 °C with a ramping rate of 10 °C/min, in an air flow of 100 mL/min. The amount of coke was calculated from the weight loss between 300 °C and 700 °C, and the TGA patterns of coke in all samples were normalized based on that, starting from 300 ºC.

### 3.4.2 Gas chromatography/mass spectrometry (GC-MS)

The components of soluble coke were extracted by dichloromethane and analyzed by Gas chromatography/mass spectrometry (GC-MS) [66]. 100 mg of the spent catalyst powders were firstly digested in 2 ml of HF solution (48 wt.%) for 30 min to release the encapsulated hydrocarbons, then the soluble organic species were extracted by 5 ml of dichloromethane ($CH_2Cl_2$). After filtering, 1 µl of the obtained organic liquid mixtures were analysed by a gas chromatography/mass spectrometry system (GC-MS, Agilent GC 7890B, Agilent 5977A mass) equipped with a moderately polar VF1701ms column (30m × 0.25mm × 0.25µm). The total ion current (TIC) chromatograms were obtained via automatic scanning in the mass range of m/z from 40 to 300. For comparison, each sample was batch injected through an autosampler, while maintaining the same injection temperature and the same analysis method.

### 3.4.3 Temperature-programmed oxidation (TPO)

The temperature-programmed oxidation (TPO) experiment was used to investigate the types of coke by continuously monitoring the consumption of $O_2$ as well as the emissions of CO, $CO_2$, and $H_2O$ during the oxidative decomposition of the coke inside the catalysts. 50 mg of spent catalyst sample was pretreated at 110 °C for 1 h, then cooled down to 25 °C in flowing Ar (20 Nml/min). Thereafter, 5000 ppm of $O_2$/Ar flow (20 Nml/min) was injected into sample tube and maintained until the baseline of the oxygen MS signal (m/e = 32) was stable. Further, the sample was heated from 25 °C to 700 °C, with a ramping rate of 10 °C/min and held at 700 °C for 2 h so that all the organic coke was fully decomposed. The MS signals of outlet $O_2$ (m/z = 32), $CO_2$ (m/z = 44), CO (m/z = 28), and $H_2O$ (m/z = 18) were monitored as a function of time-on-stream (TOS). The intensities of these signals were calibrated by using a standard gas mixture with known concentration before the experiment.

# 4 Main results and discussion

## 4.1 SSZ-13 zeolites with varying Al distribution and their catalytic performance in bifunctional composite for conversion of $CO_2$ to light olefins

It has been shown that the SSZ-13 zeolite has the most potential as a substitute for the SAPO-34 molecular sieve catalyst in the MTO reaction since they have the same topology and pore structure. In order to adjust its acidity, so that it can achieve a comparable performance to SAPO-34 in the reaction of $CO_2$ hydrogenation to olefins, in **Paper I**, the SSZ-13 zeolites with isolated acid site distribution (isolated Al distribution) and varying acid density were synthesized. Their performances were investigated, and the main acid properties promoting high product selectivity and stability were sorted out. For comparison, the SSZ-13 zeolites with the same bulk composition but containing paired acid sites (Paired Al distribution), were synthesized and tested as a reference.

### 4.1.1 Catalytic performance of two types of SSZ-13 zeolites

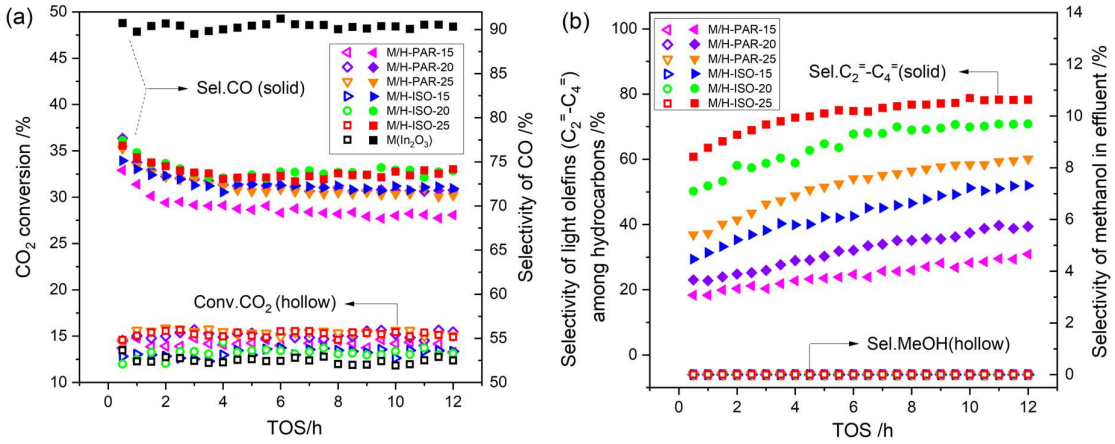


**Figure 5.** $CO_2$ hydrogenation over $In_2O_3$ catalysts or over the tandem catalysts ($In_2O_3$ and SSZ-13). (a) The conversion of $CO_2$ and selectivity for CO; (b) The selectivity for unconverted methanol and selectivity for light olefins ($C_2^=$ to $C_4^=$) among hydrocarbons. GHSV = 6400 mL*g$^{-1}$*h$^{-1}$, T=325 ºC, P=10 bar, $H_2/CO_2$= 6.

Figure 5 shows the $CO_2$ hydrogenation, over pure $In_2O_3$ catalyst and the bifunctional tandem catalysts, as a function of TOS). The pure $In_2O_3$ catalyst [M($In_2O_3$), Figure 5a] exhibited a stable performance over 12 h, where the selectivity for CO was approximately 90%, and the conversion of $CO_2$ was close to 12.3%. However, over the bifunctional catalysts consisting of $In_2O_3$ and zeolite, the $CO_2$ conversion was increased by approximately 2%, and the CO selectivity significantly decreased by approximately 25% to 30%, with the different zeolite compositions. The beneficial effect of the tandem catalyst for the conversion of $CO_2$ to hydrocarbons has been reported to be due to the rapid conversion of methanol/DME to lower olefins and other hydrocarbons, resulting a shift in the thermodynamic driving force of the methanol synthesis equilibrium toward products [27,80]. Therefore, the conversion of $CO_2$ to hydrocarbons via the methanol route is promoted, whereas the reverse water gas shift reaction (RWGS) is inhibited causing the selectivity for CO to decrease. Over the tandem catalyst composed of different SSZ-13 zeolite samples, but with the same $In_2O_3$, the reactivities of the SSZ-13 zeolite samples were evaluated for olefin production. At 325 °C and 10 bar, all SSZ-13 zeolites had a strong MTO reactivity with gradual coke accumulation. There was no apparent deactivation within the 12 h (indicated by no methanol detected in effluent), and the selectivity of light olefins ($C_2^=$-$C_4^=$) increased as the

reaction proceeded. Compared with H-PAR-x samples (x=15, 20, 25), the H-ISO-x samples exhibited a higher selectivity for olefins. In particular, the tandem catalyst M/H-ISO-25 with the highest Si/Al ratio provided 78% selectivity for light olefins at a TOS of 12 h. In contrast, over the M/H-PAR-25 catalyst, the selectivity for olefins was only 60%. It is accepted that the MTO reaction and the hydrogenation reactions proceed simultaneously on Brønsted acid sites of the zeolites in the $CO_2$ hydrogenation reaction [44]. Particularly, the different acid densities and acid distributions (Al distributions) of zeolites may all affect the MTO reactions, hydrogenation reactions, and coke deposition, resulting in different product selectivity. Therefore, it is necessary to determine which property plays a decisive role for the whole process.

### 4.1.2 Characterization of two types of SSZ-13 zeolites

#### 4.1.2.1 Bulk properties.

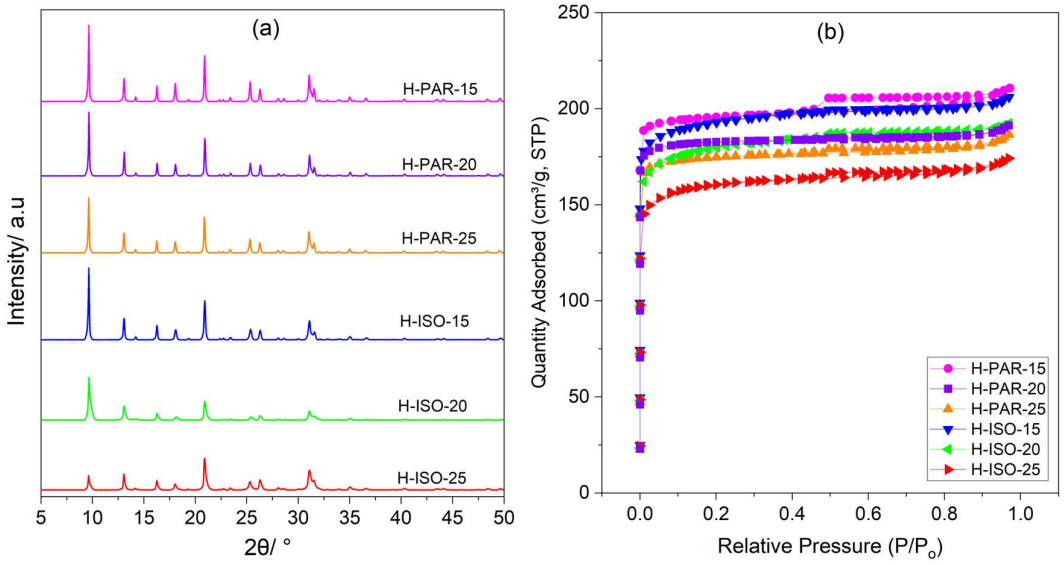


**Figure 6** XRD patterns (a) and $N_2$ adsorption-desorption isotherms (b) of synthesized H-ISO-x and H-PAR-x samples (x=15, 20, 25).

In Figure 6, the results of XRD patterns (a) and $N_2$ adsorption isotherms (b) indicate that all samples exhibited the pure CHA framework topology [81], and they clearly had micropore structures with typical type **I** isotherms [66, 77]. The micropore volumes were very close to the theoretical pore volume of CHA topology (0.24 $cm^3g^{-1}$) [78], as shown in Table 4. The XRD patterns of all samples (Figure 6a) had the same crystal plane orientation, except for sample H-ISO-25. In order to evaluate the crystallinity of the samples, the intensities of two main peaks at $2\theta = 9.6°$ and 20.9° were integrated, and the sum of the intensities of these corresponding peaks in Sample H-PAR-15 was assigned as 100% of relative crystallinity. The relative crystallinities of other samples were calculated by comparing the corresponding peaks' intensity sums with that of H-PAR-15, and the results are summarized in Table 4. The results of relative crystallinity and BET tests demonstrate that the sodium ions and the SAR of the gel precursor have important effects on the crystallization of SSZ-13 zeolites. For the Sample H-PAR-x, which utilized both $Na^+$ cations and $TMAda^+$ as SDAs in crystallization, good crystallinity and porous structure were observed, that only decreased slightly with the increase of Si/Al. However, Sample H-ISO-x synthesized by using $TMAda^+$ as the sole SDA had poor crystallinity at high Si/Al composition. At a SAR (Si/Al ratio in the gel formula) of 15, the sample H-ISO-15 had a comparable crystallinity to that of Sample H-PAR- 15. However, as the SAR decreased from 15 to 25, the crystallinity significantly

declined, and the relative crystallinity dropped to 63%. The micropore volume also decreased to 0.22$cm^3*g^{-1}$ and the BET surface area decreased to 514.8 $m^2*g^{-1}$.

**Table 4.** Characterization results of two series of proton-type SSZ-13 zeolite samples with different Si/Al ratios.

| Sample | Si/Al [a] ratio | Relative crystallinity [b] | $S_{BET}$ [c] /$m^2*g^{-1}$ | $V_{meso}$ [d] /$cm^3*g^{-1}$ | $V_{micro}$ [e] /$cm^3*g^{-1}$ | Crystal particle size [f] /μm | Particle shape [g] | $Co^{2+}$ exchange capacity [h] |
|---|---|---|---|---|---|---|---|---|
| H-PAR-15 | 13.9 | 100.0% | 622.3 | 0.042 | 0.28 | 0.84 | cube | 0.12 |
| H-PAR-20 | 20.2 | 95.2% | 581.0 | 0.025 | 0.27 | 3.93 | cube | 0.11 |
| H-PAR-25 | 26.5 | 89.6% | 556.1 | 0.033 | 0.26 | 4.19 | cube | 0.09 |
| H-ISO-15 | 14.2 | 98.5% | 617.7 | 0.056 | 0.26 | 2.73 | pseudo-cube | 0.02 |
| H-ISO-20 | 20.3 | 72.3% | 578.3 | 0.059 | 0.24 | 2.88 | cube | <0.01 |
| H-ISO-25 | 27.3 | 63.0% | 514.8 | 0.051 | 0.22 | 2.84 | cube | <0.01 |

[a] Mole ratio was determined by XRF. [b] Relative crystallinity (RC).[c] BET surface area. [d] Mesopore volume. [e] Micropore volume. [f] Average crystal particle size and [g] Crystal particle shape from SEM micrographs. [h] Cobalt cation exchange capacity.

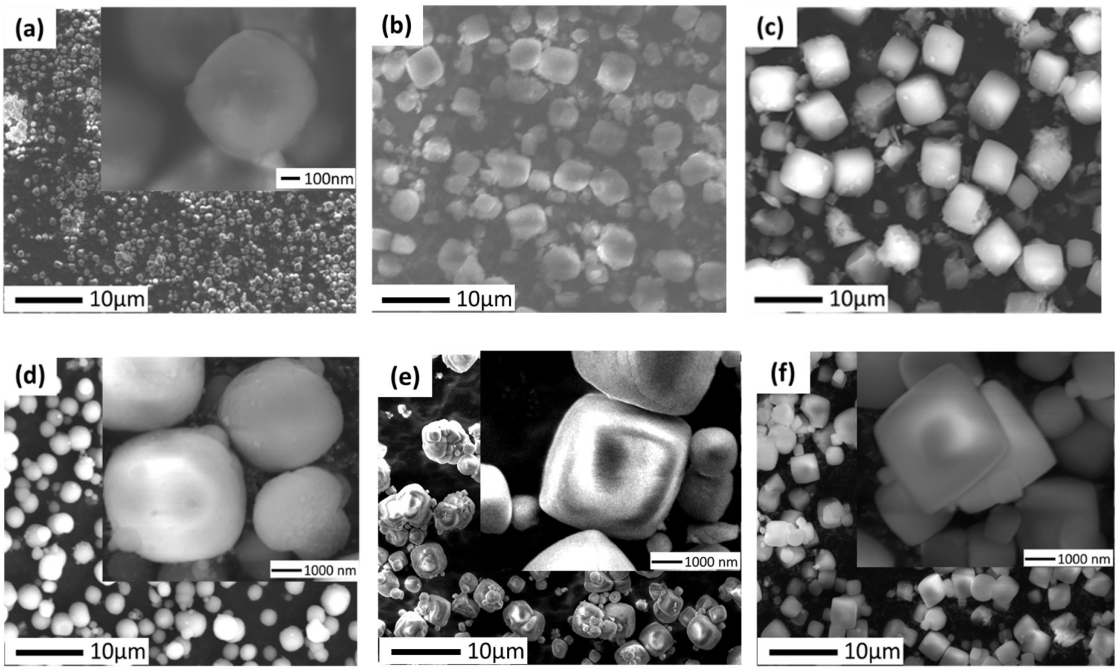


**Figure 7.** SEM images of two types of HSSZ-13 zeolites: (a) H-PAR-15, (b) H-PAR-20, (c) H-PAR-25, (d) H-ISO-15, (e) H-ISO-20, (f) H-ISO-25.

In Figure 7, the H-PAR-x samples had the same cubic morphology in a SAR range from 15 to 25, whereas the H-ISO-x samples exhibited diverse morphologies with changes in SAR. Sample H-ISO-15 presented pseudo-cubic crystal-particles, and macro-steps appeared on its crystal surface (Figure 7d, inset), which appeared to be aggregates of small and layered crystal particles. As the SAR increased, the crystal particles of the sample gradually transitioned to a cubic face profile, and sample H-ISO-25

exhibited the positive facets of cubic crystals (Figure 7f). Notably, the morphology of H-ISO-x samples was preserved well, there were no irregular silicon-aluminum oxides or worm-like amorphous precursors on the crystal particle surface of sample H-ISO-20 (Figure 7e, inset) or H-ISO-25 (Figure 7f, inset). Although the XRD and nitrogen adsorption experiments demonstrated that the crystallinity of the sample decreased with increasing SAR.

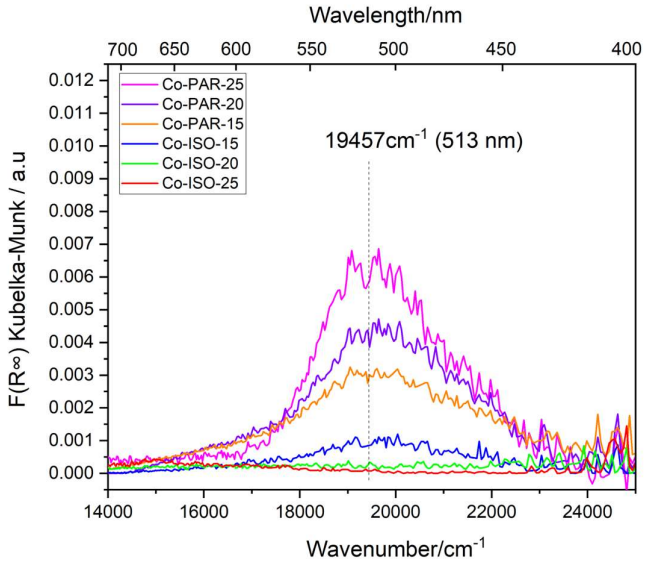


**Figure 8** UV-Vis spectra of rehydrated Co-PAR-x and Co-ISO-x samples (x=15, 20, 25) at ambient temperature.

In the framework of silica-alumina zeolite, the paired proton sites mainly originate from the proximity of Al in the framework, such as the arrangement structure of Al-O-(-Si-O) -Al or Al-O-(-Si-O)$_2$ -Al. When the framework aluminum atoms are far apart (x >2 in the Al-O-(-Si-O) x -Al structure), they are usually referred to as an isolated aluminum distribution, and the corresponding proton acid sites are also termed isolated proton sites [77]. It is widely accepted that a pair of Al atoms (paired proton sites) in the zeolite framework can accommodate a tetrahedrally coordinated bare $Co^{2+}$ cation under dehydration conditions, and uptake an octahedrally coordinated $Co^{2+}$ hexahydrate complex under humid conditions [77-78]. After cobalt ion exchange experiments, it was found that there were obvious Co species in H-PAR-x, and the content increased with a decrease in SAR (as shown in Table 4). In order to further distinguish the introduced $Co^{2+}$ ions, rather than cobalt oxides or cobalt silicate species, Ultraviolet-visible (UV-Vis) spectroscopy was performed to identify the incorporated $Co^{2+}$ on the paired proton sites of SSZ-13 zeolites. In Figure 8 it is clear that a distinct adsorption spectrum centered at a wavenumber of 19457 cm$^{-1}$ (513 nm of wavelength) was present in the rehydrated Co-PAR-x samples (x =15, 20, 25), which was the characteristic absorption band of the d–d electronic transition of octahedrally coordinated $Co^{2+}$ cations [77-79]. In contrast, the absorption band of the Co-ISO-x samples was weak and almost negligible. The results of ICP further confirmed that the total cobalt contents were also very low, which indicates that H-ISO-x samples only contained the isolated proton sites, whereas the H-PAR-x samples included some portion of paired protons.

In the synthesis system of the H-ISO-x samples with $TMAda^+$ as the only SDA, the bulky exogenous $TMAda^+$ cation is enclosed in the cage of crystalline SSZ-13, and it can only balance the negative charges generated by the nearby and isolated $AlO_4^-$ tetrahedron during the crystallization process [77-78]. According to the charge balance theory, when there is a lack of free small cations in the synthetic

system, the successful crystallization of SSZ-13 is limited to an Si/Al ratio (SAR) ranging from 15 to 30, and miscellaneous crystals and defects will appear when the SAR of the feed is outside of this range [77]. Here, the crystallization was carried out within the valid SAR range, it was also found that the crystallinity decreased sharply with the increase in SAR. However, no miscellaneous crystals or amorphous silicon-alumina were found in the results of XRD or SEM, which led to the conjecture that there are some defects in its structure, which resulted in reduced crystallinity and porous properties.

#### 4.1.2.2 Identification of Al sites inside zeolite structure

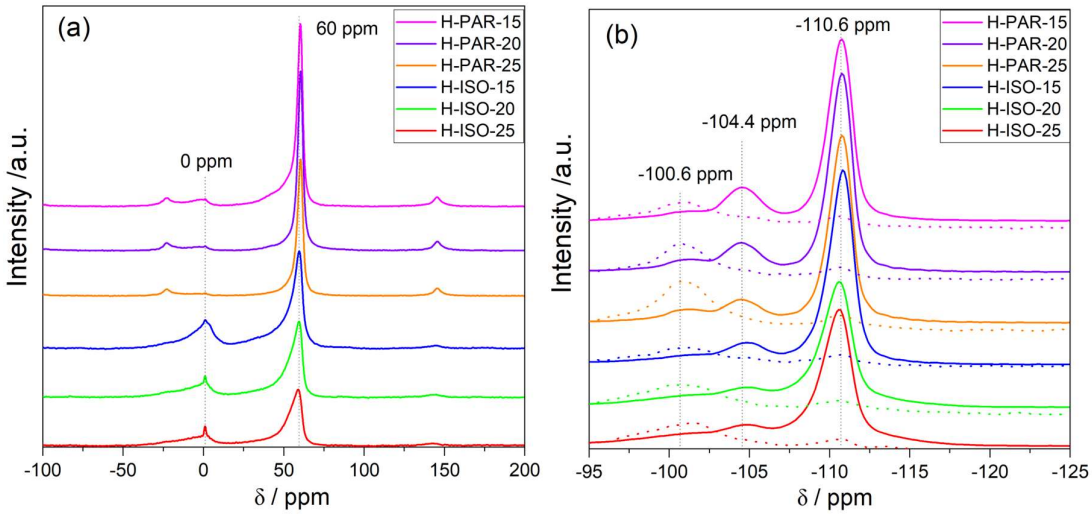


**Figure 9.** $^{27}$Al MAS(a), $^{29}$ Si MAS (b, solid traces), and $^{29}$Si CP-MAS NMR (b, dotted traces) of H-ISO-x and H-PAR-x samples (x=15, 20, 25).

The $^{27}$Al MAS NMR spectra of sample H-PAR-x and sample H-ISO-x are shown in Figure 9a. The resonance at approximately 60 ppm was assigned to the tetrahedrally coordinated Al atoms in the framework, and the signal at 0 ppm was attributed to the extra-framework octahedral coordinated Al atoms[71,77,78,82,83]. Nearly all of the aluminum atoms in the H-PAR-x samples were in the framework. In contrast, some extra-framework aluminum species were formed in the H-ISO-x samples.

In Figure 9b the framework Si atoms with the $Q^4$(0Al) ( at -110 ppm) or $Q^4$(1Al) (-104ppm) configurations were clearly observed from the $^{29}$Si MAS NMR spectra (Figure 8b, solid traces) from all samples. Because the replacement of one Si by one Al atom in the framework of zeolite causes a downfield shift of approximately 5 ppm [78,82], with the help of cross-polarization spectra ($^{29}$Si CP-MAS in Figure 8b, dotted traces), the board peak at approximately −100 ppm was identified as the resonance of Si atoms in the $Q^3$(0Al) [ Si $(OSi)_3(OH)$] coordination, rather than in the $Q^4$(2Al) [Al-O-Si $(OSi)_2$-O-Al] linkages [71,77]. Based on the identification of the above resonance peaks, deconvolution and curve fitting was performed on the $^{29}$Si MS NMR spectrum, and the estimated value of the Si/Al ratio (SAR) in the zeolite framework was calculated according to the relative peak area, as shown in Table 5. It can be clearly seen that the framework SAR of the H-PAR-x samples, estimated by the $^{29}$Si MAS spectra, was consistent with the SAR in the bulk phase. On the contrary, for the H-ISO-x samples, the SAR in the framework was much higher than the SAR in the bulk phases. This result is consistent with the results of $^{27}$Al MAS NMR spectra, further confirming the presence of non-framework aluminum species in H-ISO-x samples, whereas the Al in the H-PAR-x samples all existed in the form of framework aluminum. For the H-PAR-x samples, The results of the $^{29}$Si specta ruled out the existence of linkages of Al-O-Si-O-Al [$Q^4$(2Al)] in the structure. Combined with the UV-Vis results

(Figure 8), it can be further noted that the paired Al (paired protons) mainly existed in Al-O-Si-O-Si-O-Al, rather than in the Al-O-Si-O-Al structure.

**Table 5.** The deconvolution results of $^{29}$Si MS NMR spectra of proton type SSZ-13 zeolite samples and their corresponding acid amount from $NH_3$-TPD results.

| Samples | Si/Al[a] | Proportion of $Q^4$(nAl) and $Q^3$(nAl) [b] /% | | | | Si/Al[c] | BAS density[d] |
|---|---|---|---|---|---|---|---|
| | /100% | $Q^4$(0Al) | $Q^4$(1Al) | $Q^4$(2Al) | $Q^3$(0Al) | /100% | /mmol*g$^{-1}$ |
| H-ISO-15 | 13.9 | 74.5 | 18.5 | 0 | 7.0 | 20.1 | 0.35 |
| H-ISO-20 | 20.2 | 74.6 | 13.6 | 0 | 11.8 | 25.9 | 0.25 |
| H-ISO-25 | 26.5 | 72.6 | 10.5 | 0 | 16.9 | 31.6 | 0.23 |
| H-PAR-15 | 14.2 | 69.4 | 22.2 | 0 | 8.4 | 16.5 | 0.41 |
| H-PAR-20 | 20.3 | 73.6 | 18.7 | 0 | 7.6 | 19.7 | 0.35 |
| H-PAR-25 | 27.3 | 74.1 | 13.3 | 0 | 12.6 | 26.3 | 0.30 |
| TEA-ISO-15 | 13.9 | 61.2 | 19.0 | 0 | 19.9 | 16.9 | / |
| TEA-ISO-20 | 20.2 | 60.0 | 14.9 | 0 | 25.4 | 20.1 | / |

[a] Si/Al ratio of bulk phase. [b] Proportions of the different Si species with the $Q^4$(nAl) or $Q^3$(nAl) configuration. [c] The Si to Al ratio in the framework. [d] Brønsted acid density.

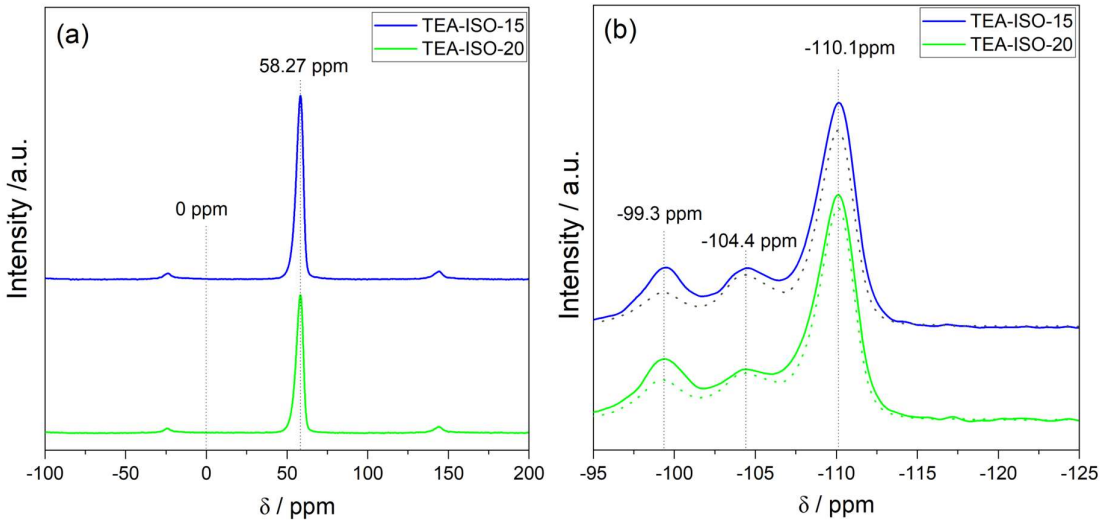


**Figure 10**. $^{27}$Al MAS(a), $^{29}$ Si MAS (b, solid traces), and $^{29}$Si CP-MAS NMR (b, dot traces) of TEA-ISO-15 and TEA-ISO-20 samples.

Figure 10 further confirms the information about the framework structure of the H-ISO-x zeolite precursors (TEA-ISO-15 and TEA-ISO-20) before calcination. In the $^{27}$Al MAS NMR spectra (Figure 10a), there is no resonance peak of octahedrally coordinated non-framework aluminum (0 ppm), only the signals of tetrahedrally coordinated framework aluminum (58.27 ppm) were present. The deconvolution results of the $^{29}$Si MS NMR spectra (Figure 10b) also showed that the SAR in the framework was close to the bulk SAR. This information proves that the precursors of the H-ISO-x zeolite samples had a relatively complete framework before calcination, and that the framework dealumination occurred during the process of calcination to remove the SDA. The dealumination,

thereby produced octahedral non-framework aluminum species, leading to a decrease in crystallinities and porous properties. It is particularly noteworthy that the resonance peaks related to the silanol structure $Q^3$(0Al) (-99.3ppm) decreased rapidly after calcination, which suggests that silanol species were the potential defect sites leading to the framework dealumination during calcination.

#### 4.1.2.3 Acidity characterization.

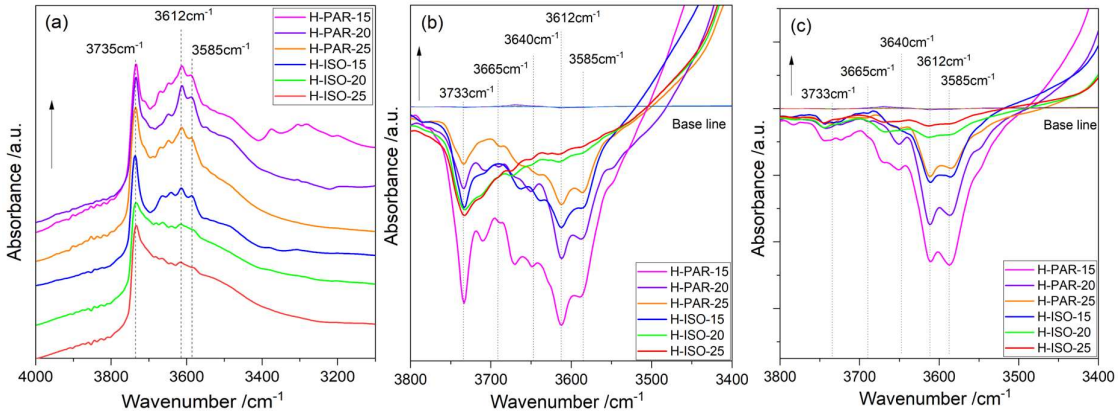


**Figure 11**. The IR spectra of hydroxyl groups on the surface of proton-type samples (a), and the corresponding hydroxyl bands after ammonia adsorption at 30 °C (b), or after ammonia adsorption at 200 °C (c).

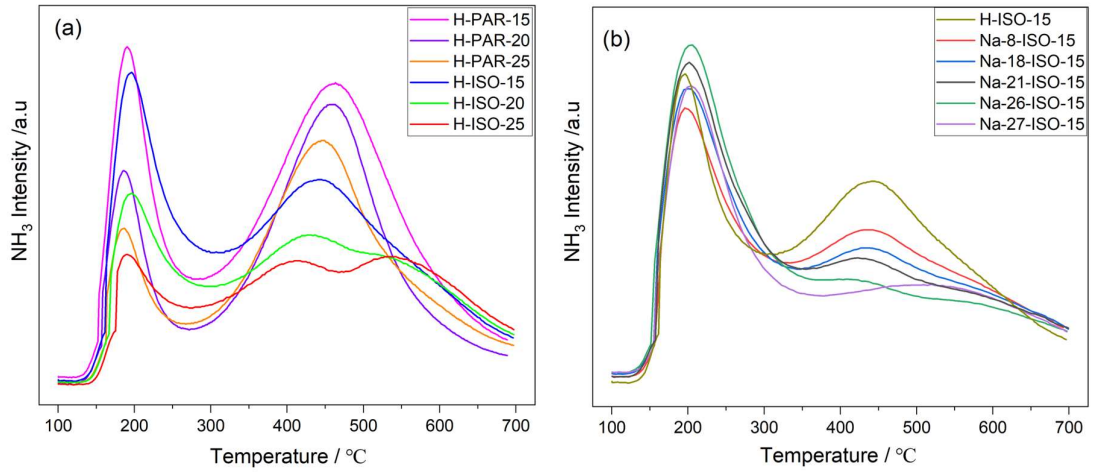


**Figure 12.** $NH_3$-TPD profiles of proton-type zeolite samples (a), and the sodium-type samples prepared by exchanging the H-ISO-15 sample with sodium nitrate (b).

Figure 11a exhibits the surface acidity of two types of protonic SSZ-13 zeolite samples. No vibration signal of Al-OH bonds (3782$cm^{-1}$) of amorphous alumina was detected in any of the samples [84]. In terms of the band intensity of the bridged hydroxyl groups (3612$cm^{-1}$, 3585$cm^{-1}$) [84-86], it was found that the intensity in H-PAR-x (x=15, 20, 25) samples was higher than that in the H-ISO-x samples, which indicates that there are more Brønsted acid sites in the H-PAR-x samples. In the same series of samples as the SAR increases, the relative strength of the bridging hydroxyl groups decreased, which also predicts a decline in its Brønsted acidity. To identify the strength of the acid sites associated with the surface hydroxyl groups, the adsorption spectra were collected after adsorbing $NH_3$ at 30 °C (Figure

11b ) and 200 ℃ (Figure 11c), where the positive bands (3500-3100 $cm^{-1}$ and 1800- 1350 $cm^{-1}$) indicate the formation of adsorbed species, and negative bands (3700-3500 $cm^{-1}$) refer to the consumption of nonacidic/acidic sites[84]. It was observed that almost all hydroxyl species can adsorb ammonia at these low temperatures (30 ℃), resulting in the decay of the hydroxyl vibrational band from the reference zero to a negative value. When the adsorption temperature increased to 200 ℃ (Figure 11c), the $NH_3$ desorbed from the weak acid sites, but remained adsorbed on strong acid sites, thus showing that there are still negative bands in the bridging hydroxyl range (about 3600 $cm^{-1}$). This result clearly indicates that the acid sites associated with bridged hydroxyl groups (Brønsted acid sites) are strong acidic sites, compared to silanol groups (3733 $cm^{-1}$) and extra-framework Al hydroxyl groups (3665 $cm^{-1}$, 3640$cm^{-1}$). For the $NH_3$ adsorption at 200 ℃, it can still be observed that the negative intensities of the hydroxyl bonds on the surface of the H-ISO-x samples were weaker than those of the H-PAR-x samples. This result is consistent with the relative intensities of the surface hydroxyl groups, indicating that the Brønsted acidity of the H-ISO-x samples were weaker than the H-PAR-x samples. Although the distribution of proton acid sites of samples H-PAR-x and H-ISO-x was different, there was no difference in the produced hydroxyl groups. After the adsorption of ammonia, the vibrational bands of the hydroxyl groups did not undergo any red-shift or blue-shift (see Figures 6b, 6c). This means that these acid sites exhibited the same acidic strength towards the adsorbate ($NH_3$), regardless of the acid site distribution.

In the spectroscopic experiments it has been proven that the adsorption of ammonia at a high temperature occurs mainly on the Brønsted acid sites. Therefore, the precise quantification of acid sites of samples was carried out with $NH_3$-TPR measurements. In Figure 12a all samples presented two major desorption peaks centered around ∼200 ℃ and 450 ℃, the amount of Brønsted acid (BAS) density was calculated by deconvolution and integration of the desorption peaks centered in the range 300 °C to 700 °C, and recorded in Table 5. There is a strong correlation between the BAS density and the ratio of Si/Al in the framework of the samples. Moreover, the additional sodium ion exchange experiments also confirm that the neutralization of Brønsted acid sites by sodium ions will reduce the high-temperature desorption peak of $NH_3$ during the $NH_3$-TPR experiment (Figure 12b). With the increase in Si/Al in the framework, the BAS density gradually decreased, demonstrating the order of strength: H-PAR-15 > H-PAR-20 ≈H-ISO-15 >H-PAR-25 > H-ISO-20> H-ISO-25. In examination of the results of the catalytic experiment under the same reaction conditions and TOS, among the catalysts with different acidity, the selectivity for light olefins exhibited an opposite, but highly correlated trend: M/H-ISO-25 > M/H-ISO-20 > M/H-PAR-25 > M/H-ISO-15 > M/H-PAR-20 > M/H-PAR-15.

### 4.1.3 Effect of Brønsted acid density on the reactivity of H-SSZ-13 zeolite

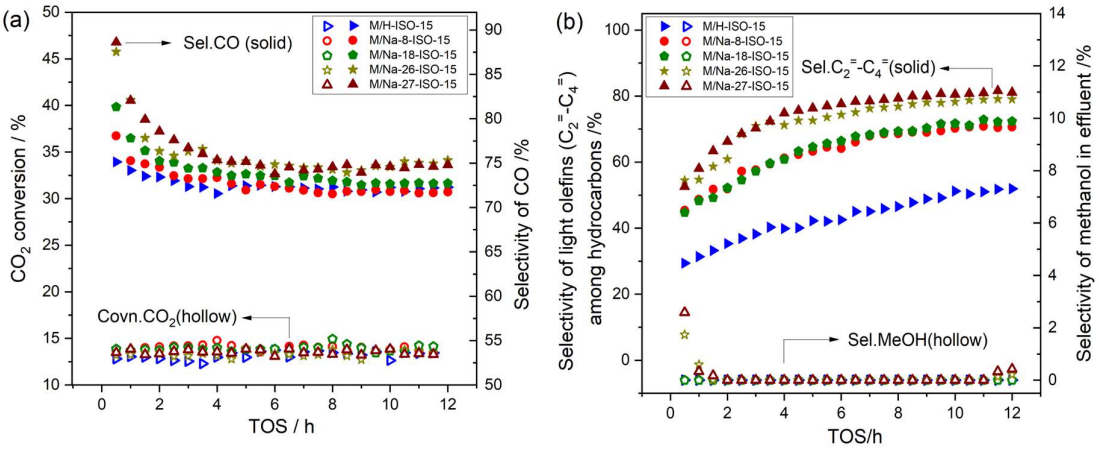


**Figure 13.** $CO_2$ hydrogenation over the bifunctional catalysts of $In_2O_3$ and SSZ-13 with varying Brønsted acid site densities. (a) The conversion of $CO_2$ and selectivity for CO; (b) The selectivity for unconverted methanol and selectivity for light olefins ($C_2^=$ to $C_4^=$) among hydrocarbons. GHSV = 6400 $mL*g^{-1}*h^{-1}$, T=325 ºC, P=10 bar, $H_2/CO_2$= 6.

**Table 6.** Physicochemical properties of sample H-ISO-15 before and after sodium ion exchange.

| Sample | Na [a] /wt.% | Al [a] /wt.% | $S_{BET}$ [b] /$m^2*g^{-1}$ | $V_{micro}$ [c] /$cm^3*g^{-1}$ | Exchange degree [d] /% | BAS density [e] /$mmol*g^{-1}$ |
|---|---|---|---|---|---|---|
| H-ISO-15 | / | 2.79 | 619 | 0.26 | / | 0.35 |
| Na-8-ISO-15 | 0.18 | 2.73 | 585 | 0.25 | 8% | 0.26 |
| Na-18-ISO-15 | 0.44 | 2.77 | 596 | 0.25 | 18% | 0.23 |
| Na-21-ISO-15 | 0.51 | 2.78 | 570 | 0.24 | 21% | 0.21 |
| Na-26-ISO-15 | 0.61 | 2.73 | 573 | 0.24 | 26% | 0.17 |
| Na-27-ISO-15 | 0.62 | 2.74 | 577 | 0.23 | 27% | 0.15 |

[a] Concentrations of Na and Al. [b] BET surface area. [c] Micropore volume. [d] Exchange degree. [e] Brønsted acid density.

In order to further distinguish the effect of BAS density, rather than that of others, on the distribution of light olefin products over the tandem catalyst, the reactivities of tandem catalysts with varying BAS density of zeolite components were tested and are shown in Figure 13. The detailed physicochemical properties of zeolite components are shown in Table 6. By using the zeolite sample H-ISO-15 as parent material, the Brønsted acidity of H-ISO-15 was modified by $Na^+$ ion exchange. The obtained Na-type zeolite samples exhibited decreased BAS density without changing the porous properties.

It was found that the Brønsted acid site (BAS) density was the determining factor for product distribution and stability of the catalyst. Catalysts with higher acid density demonstrated higher MTO and hydrogenation activity, and the products were dominated by alkanes. As the BAS density of the catalyst decreased, both the MTO reaction rate and the hydrogenation rate decreased simultaneously, and the catalysts with lower BAS density gave higher selectivity of light olefins. However, when the BAS density of the catalyst was too low, the selectivity of olefins could not be further improved, on the contrary, its stability was severely weakened. Specifically, the catalysts with low BAS density showed a low methanol conversion rate at the beginning of the reaction, where unreacted methanol appeared in

the effluent. At the same time, the accumulation of methanol also caused a higher CO selectivity during the initial stage. With the establishment of the organic co-catalyzing centers (hydrocarbon pool species, HCPs), the conversion of methanol gradually increased, and the selectivity to CO decreased to its steady-state value as the reaction proceeded. After the reaction continued for 12 h, the active sites of the catalyst were covered or blocked due to the accumulation of coke deposition. The catalysts with the lowest BAS density, therefore, exhibited quick deactivation, which was manifested by the reappearance of unreacted methanol in the effluent, and the selectivity of CO increased again.

### 4.1.4 Effect of Brønsted acid density on the coking behavior

Figure 14 shows the coke deposition characteristics of tandem catalysts with different acidities. From the result of TGA (Figure 14a), it is clear that the BAS density of the zeolite components affected the coke deposition rate in the tandem catalyst. When the BAS density of the zeolites was higher than 0.25 mmol/g, the coke deposition was low, and the amount of coke on the catalysts with different BAS density had few variations after 12 h of reaction. On the contrary, when the BAS density was lower than 0.25 mmol/g, the coke deposition rate increased rapidly. The TPO profiles found that the BAS density of the catalyst also affected the type of deposited coke (Figure 14b). The high-temperature decomposed coke dominated inside of catalysts with a BAS density higher than 0.23 mmol/g. When the BAS density of the catalyst was reduced below 0.23 mmol/g, the low-temperature decomposed coke increased more rapidly. The lower the BAS density, the higher proportion of the low-temperature decomposed coke. The analysis of soluble coke in the spent catalyst by GC-MS further confirmed that the composition of coke was closely associated with the BAS density. On catalysts with high BAS density, the deposited coke was light methylbenzenes, mainly including toluene to tetra-methylbenzene. When the BAS density gradually decreased, in addition to light methylbenzene, the penta-methylbenzene, hexa-methylbenzene, and adamantane species appeared in large numbers on the spent catalyst. It is well known that methylbenzenes are generally considered to be the hydrocarbon pool species (HCPs), which catalyze the MTO reaction together with Brønsted acid centers [25,26,45]. Whereas adamantane species are generally considered as the main species that cause rapid deactivation of MTO at low temperatures (300-400 °C) [25,72]. Therefore, it is reasonable to speculate that too low BAS density led to deactivation of the catalyst, possibly due to the large amount of inactive adamantane species.

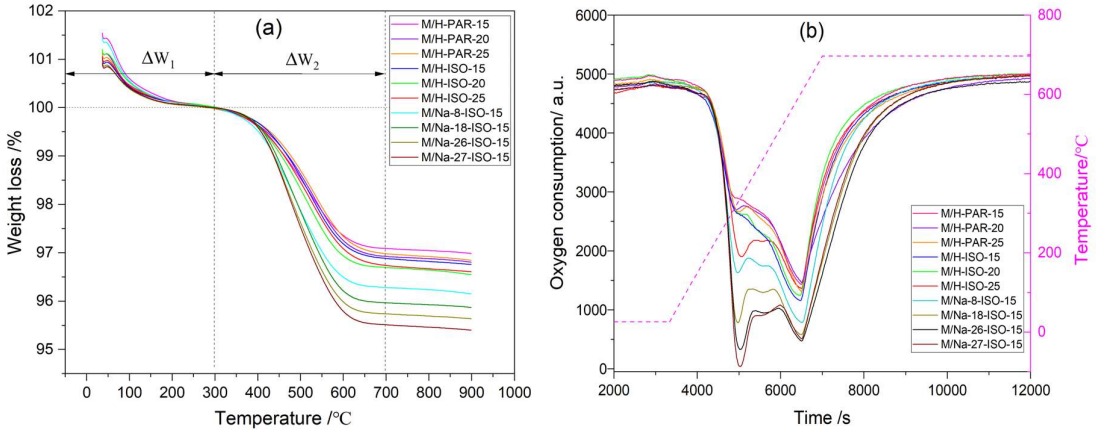


**Figure 14.** The TGA patterns (a) and TPO profiles (b) of deposited coke on spent catalysts after $CO_2$ hydrogenation reaction at temperature of 325 ºC, 10 bar, $H_2/CO_2$= 6 and after TOS of 12 h.

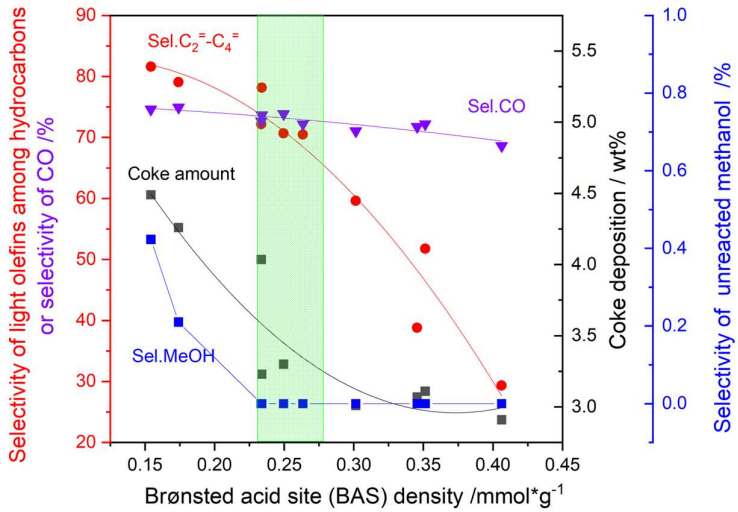


**Figure 15**. Effect of the Brønsted acid site (BAS) density of zeolite component on the catalytic performance of the bifunctional $In_2O_3$/SSZ-13 catalysts. (1) The selectivity for light olefins ($C_2^=$-$C_4^=$), (2) coke deposition amount, (3) the selectivity for unreacted methanol at TOS of 0.5 h. Reaction condition: catalyst weight = 1 g, the weight ratio of $In_2O_3$/SSZ-13 = 2 in granule mixture, GHSV = 6400 mL*g$^{-1}$*h$^{-1}$, T=325 ºC, P=10 bar, $H_2/CO_2$= 6. TOS=12 h.

In Figure 15 the effect of the BAS density on the selectivity for CO, the selectivity for light olefins among hydrocarbons, and the selectivity for unreacted methanol during the initial period (0.5h), as well as the coke deposition, has been summarized after the 12 h experiments. Among all the catalysts with varying Al distributions and porous properties, it can be clearly seen that the BAS density exhibits a good correlation with the selectivity for light olefins and coke deposition in $CO_2$ hydrogenation. This further demonstrates that the BAS density of the zeolite component in the bifunctional catalysts is the decisive factor for olefin production. In order to achieve both high selectivity of olefins and stability of the catalyst, the BAS density of the catalyst must be optimized within a reasonable range. Under the current reaction conditions (325 ºC, 10 bar), the ideal BAS density of the zeolite was about 0.25 mmol/g. Zeolite H-ISO-20 was suitable for such acidity when combined with an $In_2O_3$ catalyst as a bifunctional tandem catalyst. Catalyst M/H-ISO-20 gave 70% selectivity for light olefins among hydrocarbons and 74% selectivity for CO with no deactivation after 12h of operation. It should be pointed out that over a tandem catalyst with a fixed composition, the selectivity for olefins also gradually changes with the progression of the reaction, here the continuous accumulation of coke may be the main reason for the change in catalytic performance. Further investigation associated with coke accumulation during $CO_2$ hydrogenation is discussed in **Paper II**.

## 4.2 Modulating the formation of coke to improve the production of light olefins from $CO_2$ hydrogenation over $In_2O_3$ & SSZ-13 catalysts

As described in section 4.1, the Brønsted acid (BAS) density of the zeolite component is an important factor affecting product distribution and coking performance during $CO_2$ hydrogenation. However, over tandem catalysts with a fixed zeolite component, as the reaction proceeds, the coke continues to deposit, and the BAS density gradually decreases, leading to changes in the activity of the catalyst and the selectivity for products [25]. Among many coke species the active hydrocarbon pool species (HCPs), acting as co-catalyst centers for the MTO reaction, play a very important role in the formation of light olefins, whereas inert coke, such as adamantanes or bulky polycyclic aromatic hydrocarbons, covers the acid sites, blocks the pores, and leads to catalyst deactivation [72]. In order to improve the stability of the catalyst, it is necessary to study and fine-tune the type of coke, while controlling the accumulation rate of the coke. In **Paper II**, using the model tandem catalyst M/H-ISO-25 (including the $In_2O_3$ and zeolite sample H-ISO-25 as components) as the main reference catalyst, the type and accumulation rate of deposited coke, under various temperatures and pressures, was studied through transient temperature experiments. A dynamic balance mechanism between the coke formation and digestion was revealed, and a pre-coking modification method to improve olefin selectivity was proposed. One-hundred hours of testing was carried out under the optimal reaction conditions to verify the stability of the modified catalysts.

### 4.2.1 The effect of temperature on reactivity and coke deposition

#### 4.2.1.1 The effect of temperature on the product distribution

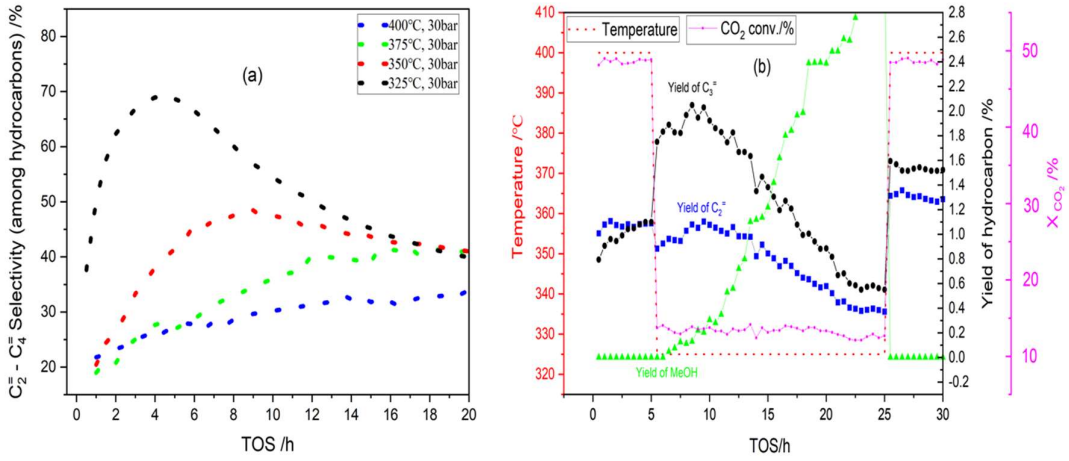


**Figure 16.** Catalytic performance of $CO_2$ hydrogenation over M/H-ISO-25 tandem catalysts. (a) Selectivity for light olefins ($C_2^=$, $C_3^=$ and $C_4^=$) with TOS during the constant temperature (T=325 ºC, 350 ºC 375 ºC, 400 ºC) experiments. Here, the selectivity for olefins is within the hydrocarbons, excluding CO, $CH_3OH$ and DME. (b) The yield of ethylene ($C_2^=$), propene ($C_3^=$), and methanol with TOS during the transient temperature experiment. Temperature variation sequence: 5 h at 400 ºC →20 h at 325 ºC→5 h at 400 ºC. Other conditions: catalyst weight = 1g, the weight ratio of $In_2O_3$/ H-ISO-25 = 2 in granule mixture, GHSV = 6400 mL*$g^{-1}$*$h^{-1}$, P=30 bar, $H_2/CO_2$= 6.

Figure 16 presents the performance of the tandem catalyst in static and transient temperature experiments. In Figure 16a, at a high temperature of 400 °C, the selectivity for olefins was low, without deactivation after running for 20 h. As the reaction temperature decreased, or the reaction time prolonged, the selectivity for olefins increased gradually, and the lower the reaction temperature, the

higher the growth rate of olefins. At 325 ℃ at TOS of 4 h, the highest selectivity for light olefins was 70% (based on total HC, not including CO) was achieved. Thereafter, the selectivity for olefins decreased rapidly as the reaction proceeded (TOS > 4 h) due to deactivation. Interestingly, from the $CO_2$ hydrogenation in the transient temperature experiment (as shown in Figure 16b), it was found that after the catalyst had been deactivated during 20 hours of reaction at 325 ℃, it could recover its reactivity when the reaction temperature was increased again to 400 ℃. By comparing the performance of the fresh catalyst and the regenerated one, under the same reaction conditions (400 ℃, 30 bar), it was found that the yield of ethylene and propene had increased, while the conversion of $CO_2$ remained the same. The following experiments and discussions were carried out to answer in detail these questions: Why did the increased temperature restore the activity of the catalyst deactivated at low temperature? Why did the regenerated catalyst have improved performance?

#### 4.2.1.2 The role of coke in the HMTO (MTO with co-feeding $H_2$) process

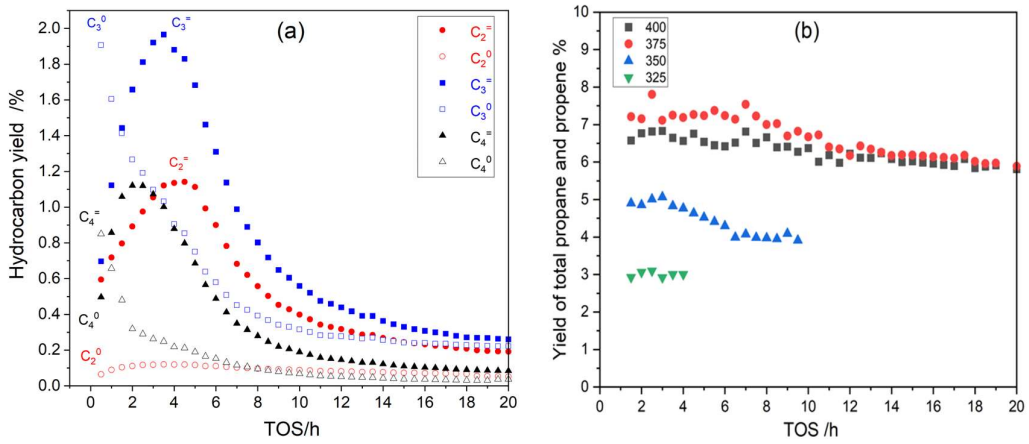


**Figure 17**. Distribution of products from $CO_2$ hydrogenation over M/H-ISO-25 tandem catalysts. (a) The yield of major hydrocarbons with TOS at 325 ℃, (b) The total yield of $C_3$ (propane and propene) at different temperature conditions before deactivation. Other conditions: Catalyst weight = 1g, the weight ratio of $In_2O_3$/ H-ISO-25 = 2 in granule mixture, GHSV = 6400 $mL*g^{-1}*h^{-1}$, P=30 bar, $H_2/CO_2$= 6.

Figure 17 records the yields of olefin and alkane products as a function of reaction time at 325 ℃ over the tandem catalysts during $CO_2$ hydrogenation. It is worth noting that the yields of ethylene and ethane exhibited a similar trend over TOS, whereas the $C_{2+}$ alkenes (e.g. propene and butene) and corresponding alkanes (e.g. propane and butane) demonstrated opposite trends before deactivation. But the sum of propylene and propane, or the sum of butene and butane remained relatively constant as the reaction proceeds. It has been generally accepted that the formation of ethylene is related closely to the aromatics cycle, and that increasing the hydrocarbon pool species and steric hindrance would be of help to improving the selectivity for ethylene [25-26, 45]. Therefore, the deposition of coke promoted the formation of total $C_2$ products: higher quantities of coke deposition before deactivation contributed to a higher selectivity towards $C_2$. On the other hand, the deposition of coke also suppressed the hydrogenation reaction of unsaturated hydrocarbons on the Brønsted acid sites, giving the increased yield of $C_{2+}$ olefins and a decreased yield of their corresponding paraffins, as is evident in Figure 17b. As the reaction proceeded (coke accumulation) before catalyst deactivation, the propene yield showed an increasing trend, and the propane yield showed a decreasing trend. However, the total yield of propene and propane was stable. DeLuca et al. claimed that the hydrogenation barrier of alkene decreased as the chain length of the molecule increased and its corresponding carbonium species

stabilized [44]. Compared with propylene and $C_{3+}$ olefins, it was difficult for ethylene to hydrogenate over a weak acid site. Therefore, coke deposition-induced inhibition of hydrogenation has a weak effect on ethylene selectivity, but it has a significant effect on increased selectivity for $C_{2+}$ olefins.

#### 4.2.1.3 The effect of temperature on the evolution of coke

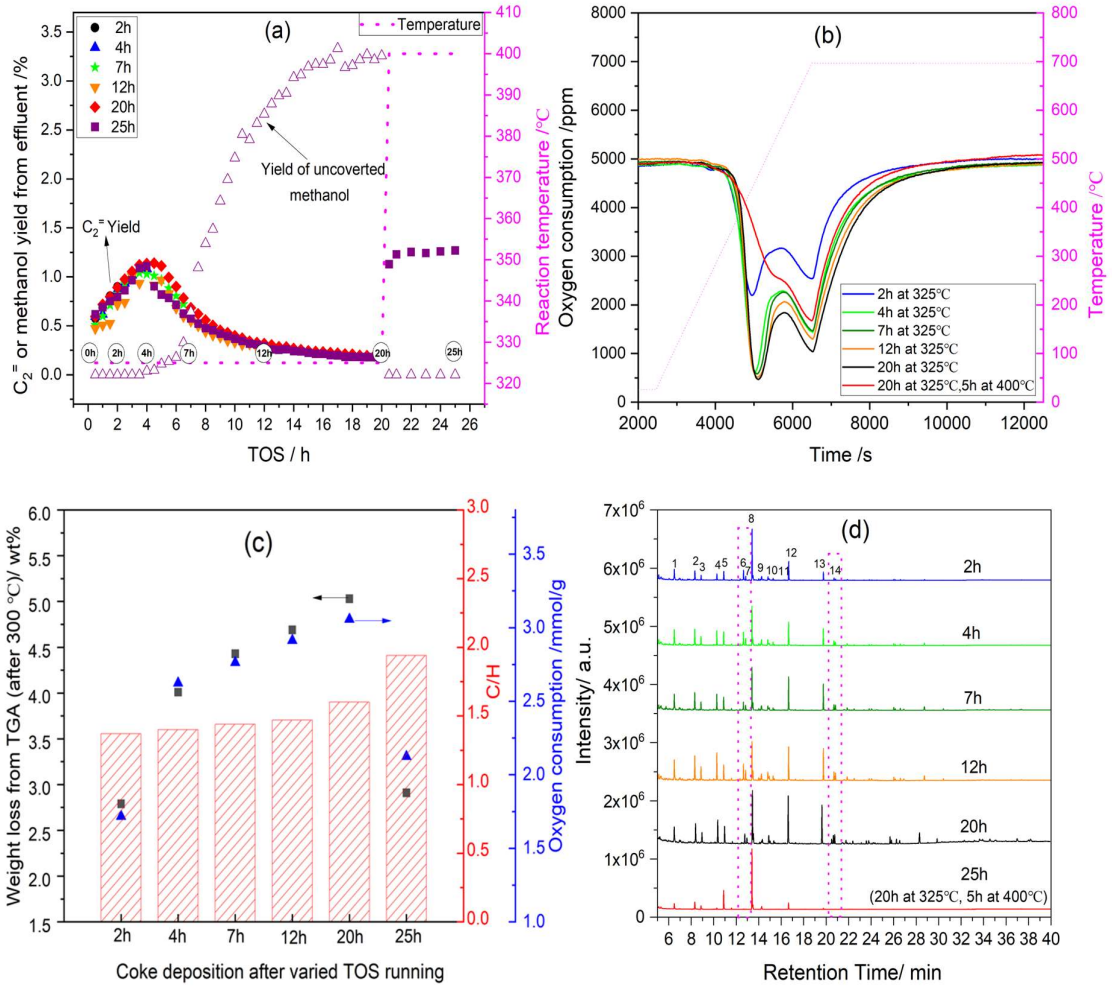


**Figure 18**. The parallel experiments of $CO_2$ hydrogenation with varying TOS and temperature over M/H-ISO-25 tandem catalysts. (a) The catalytic performance, (b) TPO profiles of coke in spent catalysts, (c) Weight loss, oxygen consumption and composition analysis (C/H mole ratio) of coke from TGA and TPO results. (d) GC-MS results of the soluble coke retained in spent catalysts. The specific compound inside of coke 1: toluene; 2 & 3: xylene; 4 & 5: tri-methylbenzene; 6: butyl-adamantane; 7: dimethyl-adamantane; 8 & 9: tetra-methylbenzene; 10&11: naphthalene; 12: penta-methylbenzene; 13: hexa-methylbenzene; 14: methyl-diadamantane; 15: trimethyl-naphthalene; 16: tetramethyl-naphthalene; 17: naphthalene; 18: 2.6-diisopropylnaphthalene; 19: dimethylphenanthrene. Reaction conditions: catalyst weight = 1g, the weight ratio of $In_2O_3$/ H-ISO-25 = 2 in granule mixture, GHSV = 6400 mL*g$^{-1}$*h$^{-1}$, P=30 bar, $H_2/CO_2$= 6. T =325 ℃ from TOS of 0 to 20 h, T=400 ℃ from TOS of 20 h to 25 h.

In order to study the deposition rate and the evolution of coke inside of catalysts, six parallel experiments were carried out in the transient temperature experiment, the spent catalysts were taken out after various reaction times (2 h, 4 h, 7 h,12 h, 20 h, 25 h). The reactivity of catalysts and characterization results of spent catalysts are shown in Figure 18. For fresh tandem catalysts, the catalyst started to deactivate after 4 h TOS at 325 °C. After 20 hours of operation at 325°C followed by 5 hours at 400°C, the catalyst regained its activity (as shown in Figure 18a).

From the results of TPO (Figure 18b) and TGA (Figure 18c), it can be seen that the rate of coke accumulation inside the catalyst was the fastest at the initial stage of the reaction (0–4h). When the catalyst was gradually deactivated, the coke deposition rate decreased, but the accumulated amount of coke still increased slowly. At the TOS of 20 h, the accumulated coke reached the maximum value of 4.9 wt.%. However, after continuous high-temperature reaction at 400 for 5 h, the retained coke was decreased to 2.8 wt.%. Moreover, the type of coke was also significantly altered after high-temperature treatment. In the Figure 18b, after running at 325 °C, the spent catalyst contained two types of coke with oxidative decomposition peaks, centered at low temperature (500 °C) and high temperature (700 °C), and their amount increased but the composition did not change as the reaction proceeded. After continuous reaction at 400 °C for 5 h, the TPO profile of the low-temperature oxidation decomposition coke disappeared, and the amount of high-temperature oxidation decomposition coke also decreased. In Figure 18c, the detailed elemental analysis of the coke decomposition products shows that the C/H ratio of the residual coke increases after reaction at 400 °C for 5 h, which indicates decomposition of the light coke.

In Figure 18d, the GC-MS analysis gives the qualitative results for all soluble coke from spent catalysts. After the reaction at a low temperature of 325°C, the soluble coke in the spent catalyst mainly included alkylbenzenes and adamantanes. As the reaction progressed, the concentrations of heavy alkylbenzenes (Penta-methylbenzene, Hexa-methylbenzene) and adamantanes both increased gradually. The small amounts of polycyclic aromatics were present in the spent catalyst after TOS of 20 h. However, after continuous reaction at 400 °C for 5 h, almost all polycyclic aromatics, heavy alkylbenzenes, and adamantane species disappeared inside the spent catalysts. The main residual coke species were tetra-methylbenzene and other light methylbenzenes, which are generally considered as hydrocarbon pool species. In Figure 18c, it is known that the lack of low-temperature oxidation decomposition coke resulted in a higher C/H ratio of residual coke in the spent catalyst (TOS= 25 h). It is reasonable then to speculate that the low-temperature oxidation decomposition coke species (light coke) in the TPO curves are mainly associated with adamantane species. Since the adamantane species have a lower C/H ratio composition compared to polycyclic aromatics and heavy alkylbenzenes, their decomposed products should have lower C/H ratios. In the spent catalysts containing the adamantane species as coke, the C/H ratio of the oxidative decomposition products was low (seen in Figure 18 c, TOS= 20 h), while in the regenerated catalyst without the adamantane species, the TOP result of residual coke showed an increased C/H ratio (seen in Figure 18 c, TOS= 25 h).

#### 4.2.1.4 Effect of coke on the acidity and porous properties of catalysts

**Table 7.** Textural properties of spent and fresh catalysts and their fresh ingredients before and after reaction.

| Sample | $S_{BET}$ [a] ($m^2*g^{-1}$) | $V_{meso}$ [b] ($cm^3*g^{-1}$) | $V_{micro}$ [c] ($cm^3*g^{-1}$) |
|---|---|---|---|
| Fresh (H-ISO-25) | 514.8 | 0.051 | 0.220 |
| Fresh ($In_2O_3$) | 95.9 | 0.310 | 0.022 |
| Fresh (M/H-ISO-25) | 197.7 | 0.120 | 0.073 |
| Spent-20h (20h at 325 °C) | 21.2 | 0.049 | 0.003 |
| Spent-25h (20h at 325 °C, 5h at 400 °C) | 98.8 | 0.047 | 0.039 |

[a] BET surface area. [b] Mesopore volume. [c] Micropore volume.

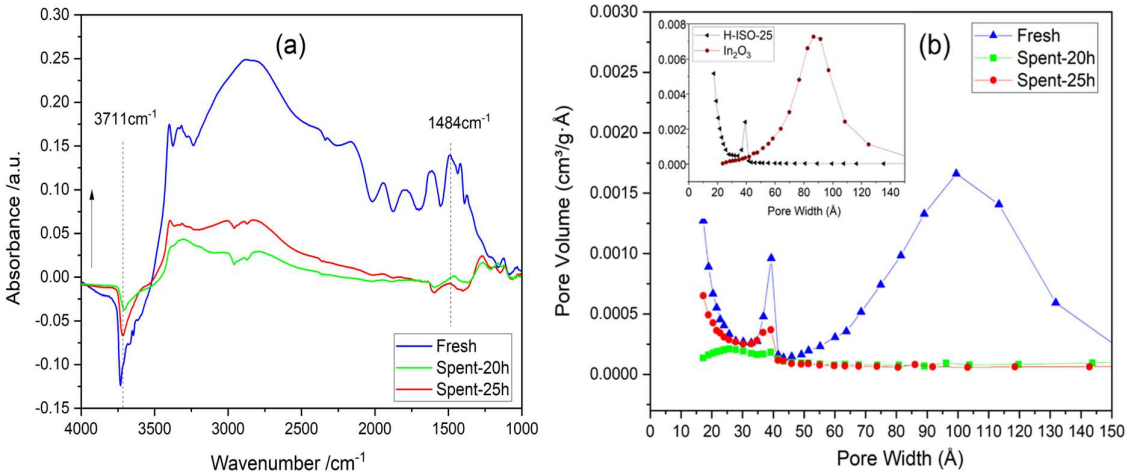


**Figure 19**. FTIR spectra of the adsorption of $NH_3$ at 30 °C (a) and pore size distribution analysis (b) of fresh and spent tandem catalysts. The 'Fresh' represents an unused catalyst (M/H-ISO-25), the H-ISO-25 and $In_2O_3$ indicate the zeolite and oxide components, respectively in the inserted panel of Figure 19b. 'Spent-20 h' is the spent catalyst after 20 h at 325 °C, and 'Spent-25h' is the spent catalyst after 20 h at 325 °C followed by 5 h at 400 °C.

Using IR spectra of $NH_3$ adsorption and the $N_2$ isothermal adsorption, the surface acidity and porous information of fresh, deactivated (TOS=20 h), and regenerated catalysts (TOS=25 h) were analyzed, and the results are shown in Table 7 and Figure 19. After 20 h of reaction at 325 °C, a large amount of coke accumulated inside the spent catalyst, covering the active hydroxyl sites (acid centers) and hindering the diffusion of products by blocking the micropore structure of the catalyst. This led to significant deactivation of catalysts. However, after continued reaction at 400 °C, without any oxygen combustion, the surface acidity and micropores were recovered to some extent. In Figure 19a, the increased negative peak of hydroxyl groups (approximately 3711 $cm^{-1}$) and slightly increased vibrational peak of adsorbed $NH_3$ (approximately 1484 $cm^{-1}$) indicate that accessible acid sites were restored [84-86]. Figure 19b demonstrates that the increase in the specific surface area and micropore volume of the catalyst supports the importance of high temperature for restoring the porosity of the catalyst.

In summary, the reaction temperature played an important role in affecting the selectivity of the target product and the lifetime of the tandem catalyst. Under the high temperature conditions, the rate of coke formation was slow, there were fewer hydrocarbon pool species, therefore the yield of light olefins was

low. Low temperature promoted both the production of active hydrocarbon pool species and inactive light coke (adamantane species), resulting in coverage of acid sites and blockage of pores, and eventually catalyst deactivation. Following regeneration at high temperatures, the harmful light coke was decomposed or transformed into polymethylbenzenes, thus allowing for the rapid build-up of the active hydrocarbon pool species. This transient temperature treatment was shown to contribute to an increased selectivity for light olefins.

### 4.2.2 The effect of pressure on reactivity and coke deposition

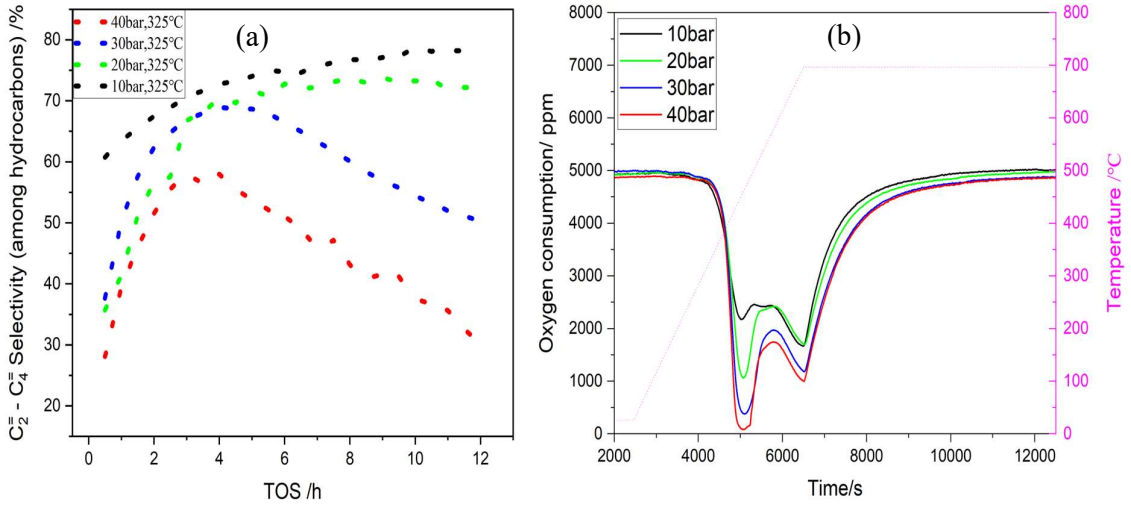


**Figure 20**. The selectivity for light olefins ($C_2^=$ to $C_4^=$) under various reaction pressures during $CO_2$ hydrogenation over M/H-ISO-25 tandem catalyst (a), and TPO profiles of the coke in the corresponding spent catalysts after 12 h of reaction (b). Here the selectivity of olefins is within the hydrocarbons, excluding CO, $CH_3OH$ and DME. Reaction conditions: catalyst weight = 1g, weight ratio of $In_2O_3$/ H-ISO-25 =2 in granule mixture, GHSV = 6400 mL*$g^{-1}$*$h^{-1}$, T=325 ºC, $H_2/CO_2$= 6, and TOS=12 h.

Figure 20 reveals the significant effect of reaction pressure on the selectivity for light olefins and the stability of catalysts. In Figure 20a, when the reaction was carried out at the low temperature of 325 °C, the higher reaction pressure had a negative impact on the stability of the catalyst. At 10 bar, the catalyst had higher stability, and the selectivity for light olefins exceeded 80% after 12 h TOS without any deactivation. As the reaction pressure increased from 10 bar to 40 bar, severe catalyst deactivation occurred, manifested in an increase in the selectivity toward the methane and unreacted methanol in the effluent. After 2.5 h of reaction at 40 bar, the catalyst began to deactivate. As mentioned earlier, when the hydrogen-to-carbon ratio of the feed was fixed, increasing the total pressure increases the partial pressure of both hydrogen and methanol simultaneously since the high pressure favors the methanol synthesis. Increasing the hydrogen partial pressure has been widely reported to suppress the coke deposition and improve the stability of catalysts. However, the increase of methanol partial pressure promotes the disproportionation reaction of methanol, thereby producing coke precursors such as formaldehyde and accelerating the deactivation of the catalyst [55]. It is apparent here that increasing the partial pressure of methanol greatly weakened the effect of the hydrogen partial pressure, in order to prolong catalyst lifetime [73]. More specifically, compared with the hydrogenation reaction, the disproportionation reaction of methanol was dominant in this case, resulting in a large amount of formaldehyde being generated and involved in the Prins reaction [55], which reacted with olefins to form dienes, aromatics, and generate inert coke substances that eventually lead to catalyst deactivation.

Figure 20b demonstrates an important correlation between reaction pressure and inert coke formation. At a low temperature of 325 °C, a large amount of light coke (low-temperature oxidation decomposition coke) was found in the deactivated catalyst after the high-pressure (40 bar) reaction. This result further confirmed that the formation of light coke, and more specifically the formation of adamantane species, was the main cause of catalyst deactivation at low temperatures. Previous studies have reported that the formation of adamantane was mainly attributed to the cyclization of dienes to cycloalkanes, followed by the subsequent isomerization of cycloalkanes to adamantanes at low temperatures under solely the MTO reaction. There was not enough evidence here to identify from which pathway it was formed during $CO_2$ hydrogenation. However, it is reasonable to speculate that formaldehyde played a key role in adamantane formation. Low temperature and high pressure accelerate the formation of formaldehyde, which forms inactive adamantane through oligomerization and cyclization, eventually leading to the deactivation of the zeolite catalyst.

### 4.2.3 Pre-coking of the catalysts with varying acidity in transient experiment

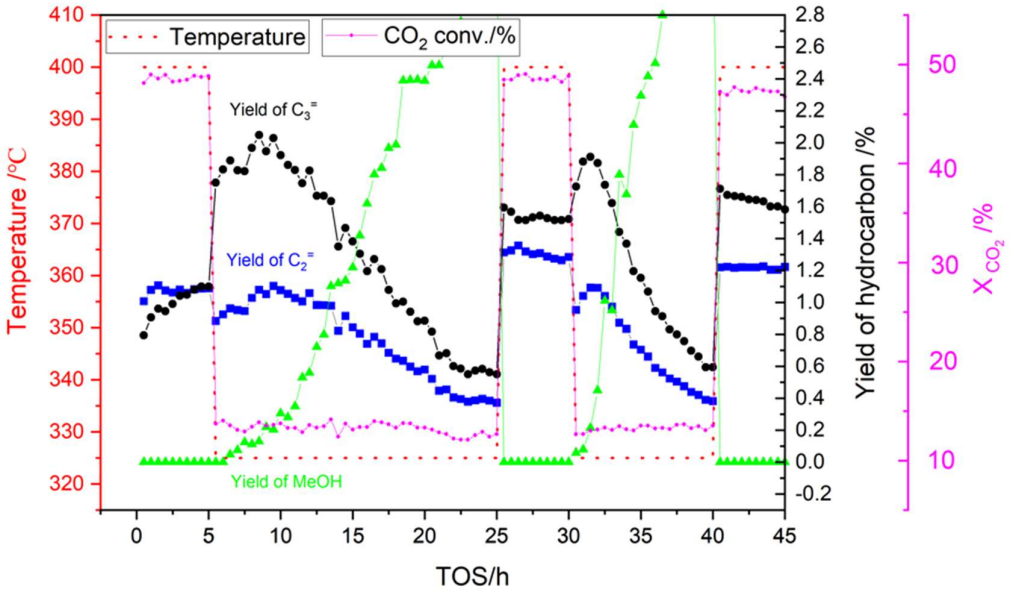


**Figure 21**. The continuous transient experiment over tandem catalyst M/H-ISO-25. Temperature variation sequence: 5 h at 400 ºC → 20 h at 325 ºC → 5 h at 400 ºC → 10 h at 325 ºC → 5 h at 400ºC. Reaction conditions: catalyst weight = 1 g, the weight ratio of $In_2O_3$/ H-ISO-25 = 2 in granule mixture, GHSV = 6400 $mL*g^{-1}*h^{-1}$, P=30 bar, $H_2/CO_2$=6.

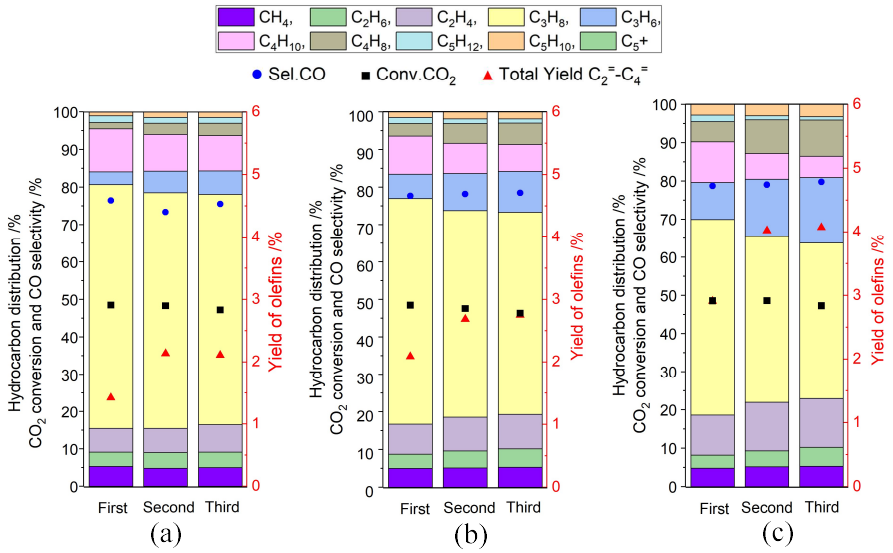


**Figure 22.** Catalytic performance of M/H-ISO-15 (a), M/H-ISO-20 (b), and M/H-ISO-25 (c) at 400 ℃ before and after coking treatment. The notations 'First', 'Second', and 'Third' refer to the reaction performance for fresh catalyst (TOS=5 h), after the first cycle of coking treatment (TOS=30 h), and after the second cycle of coking treatment (TOS=45 h), respectively in the continuous transient experiment. Reaction conditions: catalyst weight =1 g, weight ratio of oxidate/ zeolite=2 in granule mixture, GHSV = 6400 mL*$g^{-1}$*$h^{-1}$, T=400 ºC, P=30 bar and $H_2/CO_2$= 6.

Continuous transient experiments (400 ºC 5 h → 325 ºC 20 h → 400 ºC 5 h → 325 ºC 10 h → 400 ºC 5 h) were carried out to study the reactivity of catalysts with various acidities before and after pre-coking treatments. Figure 21 shows the schematic diagram of the tandem catalyst M/H-ISO-25 after two rounds of pre-coking treatment and the corresponding change in trend of olefin products. Here, the first round of pre-coking refers to the treatment from TOS =5 h to TOS=30 h, and the second round of pre-coking refers to the operation from TOS=30 h to TOS=45 h. In the initial stage at 400 °C, as the reaction progressed, coke gradually accumulated and the selectivity for light olefins increased steadily. When the reaction temperature was changed to 325 ºC, the catalyst began to deactivate. Typically, the lower the acid density of the catalyst, the faster the rate of deactivation. When the reaction conditions were returned to the second 400 °C stage, the activity and performance of all catalysts were well recovered. In the second pre-coking stage at 325 °C, the yield of light olefins again showed a volcanic curve response. This demonstrates that the coking deactivation and de-coking regeneration of the catalyst can be switched repeatedly.

To compare the performance of the catalysts before and after pre-coking, the steady-state results of TOS at 5, 30, and 45 h are selected for comparison, which are denoted as 'first, second and third,' respectively in Figure 22. The results indicate that the M/H-ISO-25 catalyst with the lowest acid density the highest selectivity for olefins after pre-coking treatments is reached. In addition, regarding the same catalyst, the yield of olefins after the second round of pre-coking treatment did not increase beyond that after the first round of pre-coking treatment. This indicates that the catalyst had established a steady state, and that the accumulation of hydrocarbon pool species had also reached a dynamic equilibrium after a sufficient duration of the coking treatment under certain reaction conditions.

### 4.2.4 The stability test of the pre-coked catalyst

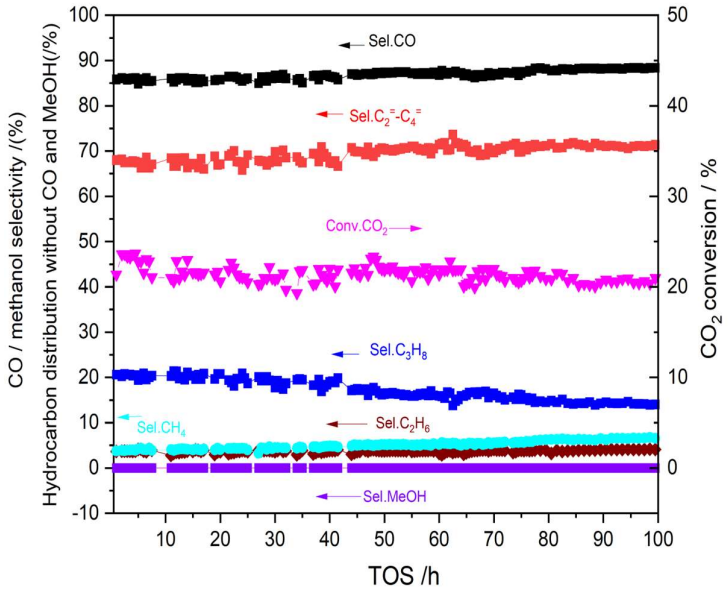


**Figure 23.** Long-term catalytic performance of pre-coked tandem catalyst M/H-ISO-25 in $CO_2$ hydrogenation. Pre-coking procedure: 325 ºC for 20 h then 400 ºC for 5 h under GHSV = 6400 mL*g$^{-1}$*h$^{-1}$, $H_2/CO_2$= 6, P=30 bar. Reaction Conditions: catalyst weight = 1 g, weight ratio of $In_2O_3$/ H-ISO-25 = 2 in granule mixture, GHSV = 6400 mL*g$^{-1}$*h$^{-1}$, P= 20 bar, $H_2/CO_2$= 3 and T=375 °C.

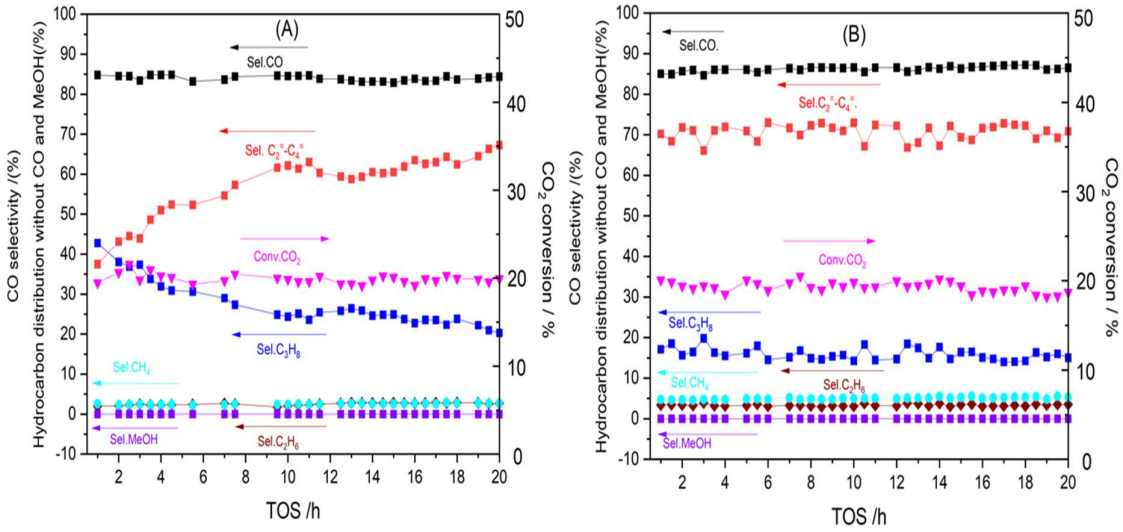


**Figure 24**. Catalytic performance of $CO_2$ hydrogenation over fresh (a) and pre-coked catalyst (b). Parent Catalyst: M/H-ISO-25, total weight = 1g, the weight ratio of $In_2O_3$/ H-ISO-25 = 2, Pre-coking procedure: 325ºC for 20 h then 400 ºC for 5 h under GHSV = 6400 mL*g$^{-1}$*h$^{-1}$, $H_2/CO_2$= 6, P=30 bar. Reaction condition: GHSV = 6400 mL*g$^{-1}$*h$^{-1}$, T=375 ºC, $H_2/CO_2$= 3. P=20 bar.

Figure 23 shows the long-term reaction performance of the tandem catalyst after a pre-coking treatment. Under the optimized reaction temperature and pressure, it demonstrated a very stable activity and high selectivity for light olefins (70% based on the formation of hydrocarbons). The $CO_2$ conversion was 20%, and there was no obvious deactivation during 100 h of operation. The results confirmed that the

combination of reaction temperature, pressure, and appropriate acid (BAS) density of the catalyst can control the type of coke and balance the formation and decomposition rates of coke, thereby prolonging the lifetime of catalysts for $CO_2$ hydrogenation. Compared with the fresh catalyst under the same reaction conditions, the results (in Figure 24) demonstrate that the pre-coking treatment played an important role in stabilizing the active sites and shortening the time for the production of light olefins. This was mainly due to the rapid deposition of hydrocarbon pool species and the regulation of catalyst acidity through this pre-coking. Therefore, under suitable reaction conditions, the balance between coke deposition and decomposition can be quickly established. To support the reaction results, the characterizations of the pre-coked catalyst, before and after long-term tests, were carried out and the results are shown in Figure 24 and Figure 25. In the pre-coked catalyst, the amount of deposited coke was 2.4 wt.%, and the light methylbenzenes were the main components of the coke. After 100 h of reaction, the coke in the spent catalyst was still dominated by light methylbenzenes with a trace of polycyclic aromatics, but no adamantanes. The total amount of coke was only 4.0 wt.%, with an average deposition rate of 0.016 wt.%*$h^{-1}$. This low rate of coke deposition further confirms an almost steady state for the formation and decomposition of coke during the long-term reaction.

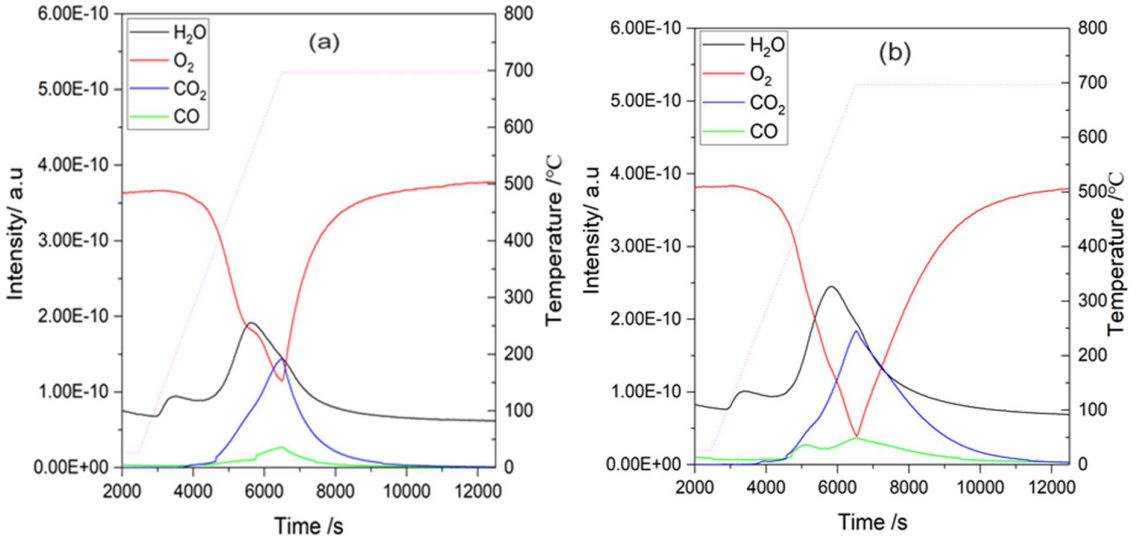


**Figure 25**. The TPO results of pre-coked catalysts before (a) and after (b) 100 h TOS (the pre-coking procedure and reaction condition are specified in Figure 23).

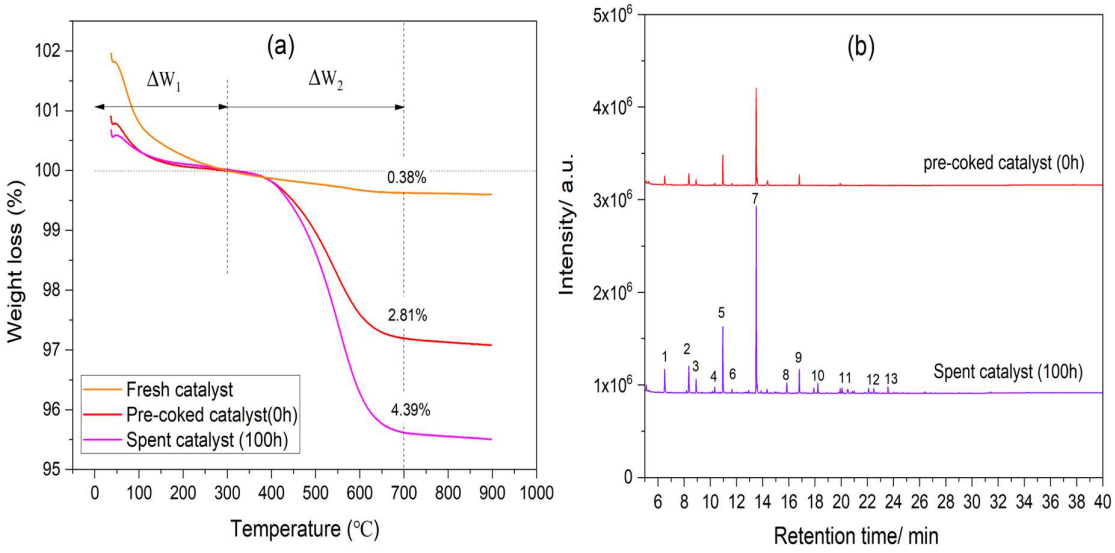


**Figure 26**. The TGA(a) and GC-MS (b) result of pre-coked catalysts before (a) and after (b) 100 h TOS (the pre-coking procedure and reaction condition are specified in Figure 23). Identification of compounds: (1) Toluene; (2), (3) Xylene; (4) p-Ethyltoluene; (5), (6) Tri-methylbenzene; (7) Tetra-methylbenzene; (8) Naphthalene; (9) Penta-methylbenzene; (10) Methylnaphthalene; (11) Dimethyl-naphthalene; (12) Trimethyl-naphthalene; (13) Tetramethyl-naphthalene.

# 5 Conclusions

The main objectives of this study were to investigate the possible use and development of SSZ-13 zeolite as an efficient MTO catalyst component in the tandem catalyst for $CO_2$ hydrogenation to light olefins. The catalyst needs to have high hydrothermal stability while also enabling high selectivity and stability towards light olefin production. To achieve this goal, SSZ-13 zeolites with various acidities were synthesized and characterized. The effects of zeolite acidity on product distribution and coke deposition were thoroughly investigated. The best SSZ-13 zeolite was screened out, and the related reasons influencing it performance have been analyzed. Simultaneously, based on the exploration of the role of coke in olefins production and the study of coke composition over the deactivated catalyst, a modified catalyst with higher olefin selectivity was further developed through pre-coking. Under the optimized reaction conditions, its stable performance was verified through a 100 h long-term test. Some fundamental insights were also proposed through detailed catalyst characterization, transient reactivity tests, and coke analysis.

Firstly, two types of SSZ-13 zeolites with similar bulk composition, but different arrangements of framework Al (isolated Al and paired Al distributions in the framework) were synthesized. Their performance was investigated at a low temperature of $CO_2$ hydrogenation, and the main acid properties (acid density and distribution) influencing selectivity for olefins and coke formation were explored. The results demonstrate that the SSZ-13 zeolites with paired Al or isolated Al distribution could be crystallized from a gel precursor respectively with and without $Na^+$ cations in the structure directing agent (SDA). Due to the lack of freely mobile $Na^+$ cations during the crystallization process, the zeolites with isolated Al also contained the $Q^3(0A)$ types of hydroxyl defects in their structure. The higher the Si/Al in the bulk phase, the higher the quantity of defect sites in the framework. After removing SDA through high-temperature calcination, the framework with the defects underwent dealumination, resulting in a lower content of bridged hydroxyl groups and lower Brønsted acid site (BAS) density. Whereas the framework of the SSZ-13 zeolites with paired Al distribution, was more stable and obtained a larger amount of Brønsted acid sites after removal of the SDA. In integrating these zeolites and indium oxides as tandem catalysts for $CO_2$ hydrogenation, the low acidity SSZ-13 zeolites with isolated Al distribution showed a good performance as MTO catalyst components and exhibited higher selectivity for light olefins during $CO_2$ hydrogenation. In order to distinguish the effects of BAS density and distribution on the product selectivity and coke formation, the $Na^+$ cations were introduced to tailor the BAS density without affecting the porous properties. These comparative experiments indicated that the BAS density was highly correlated with the selectivity for light olefins among different types of SSZ-13 zeolites. Reducing the BAS density was beneficial in improving the selectivity for light olefins. However, when the BAS density of the catalyst was too low, the catalysts exhibited firstly, increased and then, decreased MTO reactivity, giving a longer initial period in the beginning and exhibiting rapid deactivation with longer time-on-stream. The characterization of spent catalysts indicated that the catalysts with low BAS density experienced a rapid coke deposition rate. In particular, compared with polyalkylbenzenes (belonging to hydrocarbon pool species), adamantanes were found to be abundant on the deactivated catalysts, and their formation was strongly associated with emissions of unreacted methanol during the initial stage of reaction, which may be one of the most important contributing factors to catalyst deactivation. At 325 ºC and 10 bar, the preferred catalyst had a BAS density of approximately 0.25 $mmol*g^{-1}$ and exhibited 70% selectivity to light olefins among hydrocarbons and 74% selectivity to CO without deactivation after 12h time-on-stream. Most of the coke accumulated inside the catalyst was composed of alkylbenzene species.

Secondly, over the optimized tandem catalysts with the low acidity SSZ-13 zeolite component, the selectivity for olefins and coke formation (coke type and deposition rate) were systematically investigated under varying temperatures and pressures. The results indicated that the coking behavior of SSZ-13 zeolite was significantly affected by reaction temperature and pressure during $CO_2$ hydrogenation to olefins. Furthermore, coke inside zeolites was linked to both the MTO reaction and the hydrogenation of hydrocarbons, resulting in it affecting both product distributions and catalyst lifetimes. In contrast to the purely MTO reaction process, the co-existence of hydrogen with more water and methanol during the tandem process, affects the overall performance of the SSZ-13 zeolite for the MTO reactions. At high temperatures, the hydrogenation and cracking reactions dominated and inhibited the accumulation of both active coke (hydrocarbon pool species) and inactive coke species (adamantanes). These conditions prolonged the lifetime of the SSZ-13 zeolite, but a large amount of $C_{2+}$ alkanes were produced due to the excessive hydrogenation of $C_{2+}$ alkenes on Brønsted acid sites. At low temperatures, the deposition of coke was accelerated and the selectivity for olefins was improved, however, the catalyst deactivated rapidly, especially under higher pressures. This low-temperature and high-pressure condition favored the methanol disproportionation reaction and subsequent accumulation of inactive adamantanes, which blocked the pores and active sites and resulted in rapid deactivation. However, after a pre-coking treatment under transient conditions (coking at 325 ℃ followed by regeneration at 400 ℃ with constant pressure 30 bar), the inactive adamantanes were decomposed but active hydrocarbon pool species (HCPs) were preserved, which not only reopened the channel structure, but also modulated the suitable active sites within the zeolite, resulting in an improved selectivity for olefins. Continuous transient experiments further confirmed the existence of a dynamic equilibrium between the formation and degradation of coke inside SSZ-13 zeolites during $CO_2$ hydrogenation. This balance can be achieved by optimizing the reaction conditions to match the BAS density of the catalyst. Under the optimized conditions of 20 bar and 375 ℃, with an $H_2$ to $CO_2$ mole ratio of 3, the pre-coked tandem catalyst of $In_2O_3$ and SSZ-13 (BAS density =0.23 $mmol*g^{-1}$) exhibited very stable performance for $CO_2$ hydrogenation. The selectivity for light olefins was within 70% ± 2% (based on hydrocarbons formed), and the average coke deposition rate was 0.016 $wt.\%*h^{-1}$ during 100 h time-on-stream.

# 6 Future work

Our current work clearly demonstrates that SSZ-13 zeolite is a promising MTO catalyst component in tandem catalysts, giving high olefin selectivity among hydrocarbons and good stability during $CO_2$ hydrogenation. However, there remains a significant amount of CO as a by-product, mainly due to the mismatch between the optimal reaction conditions for the methanol synthesis reaction (CTM) and the methanol to olefins reaction (MTO). **Paper II** confirms that the efficient and stable performance of SSZ-13 zeolites needs to be guaranteed by high temperature and low-pressure reaction conditions, however, this condition is not favorable for methanol synthesis. On the contrary, it promotes the reverse water gas shift reaction (RWGS) and produces a large amount of CO. In **Paper I**, it was demonstrated that catalytic conversion of methanol over SSZ-13 zeolites has a thermodynamic driving force to shift the methanol synthesis equilibrium, thus suppressing the parallel RWGS reaction. Unfortunately, the promoted synergy can only be performed within a limited proximity between the $In_2O_3$ catalyst and SSZ-13 zeolite. Intimate contact between these catalyst components can cause rapid solid-state ion exchange of the indium cation into the zeolite, resulting in rapid deactivation of the catalyst [74-75].

At present, copper-based catalysts are one of the most promising catalysts for methanol synthesis at low temperatures and low pressure. At low-temperature, RWGS can be effectively suppressed, and the selectivity for CO decreased. Here, a rationally designed reactor could be conceived to carry out the synthesis of methanol or dimethyl ether in the low-temperature zone and the MTO reaction in the high-temperature zone, thereby effectively increasing the conversion rate of $CO_2$ and suppressing the formation of CO, while promoting the yield of olefins. Under the conditions of 250 °C, 30 bar, and $H_2/CO_2=3$, the results of thermodynamic calculations show that the selectivity of methanol and dimethyl ether (DMT) can reach 80%, and the conversion rate of $CO_2$ can reach up to 30% over a tandem catalyst [87]. Therefore, the next step of this work may focus on the development of low-temperature tandem catalysts for the synthesis of DME and the study of high-low temperature integrated processes. Specific research includes, but is not limited to, catalyst preparation, characterization, testing, and related kinetic modeling. Furthermore, when choosing reaction conditions, in addition to the parameters already mentioned, it is also important to consider the cost of OPEX (operating expenses) and CAPEX (capital expenditures). For example, we can recirculate CO and $H_2$ back to the process, alternatively, separate the CO and $H_2$ from $CO_2$ and use them in another process, however, it would add extra cost for the separation. The CAPEX of the plant would depend on several factors, especially the selectivity. It is therefore important to consider the whole system and it would be interesting to perform techno-economic analysis.

# 7 References


[1] Liu,W.; Cheng, S.; Malhi, H.S.; Gao, X.; Zhang, Z.; Tu,W. Hydrogenation of $CO_2$ to Olefins over Iron-Based Catalysts: A Review. Catalysts. 2022, 12, 1432.

[2] The Paris Agreement. https://www.un.org/en/climatechange/paris-agreement (accessed 02/2023).

[3] Chauvy, R.; Weireld, G. D. $CO_2$ Utilization Technologies in Europe: A Short Review. Energy Technol. 2020, 8, 2000627.

[4] European Commission, Joint Research Centre, Tsiropoulos, I., Nijs, W., Tarvydas, D., et al. Towards net-zero emissions in the EU energy system by 2050: insights from scenarios in line with the 2030 and 2050 ambitions of the European Green Deal, Publications Office, 2020, https://data.europa.eu/doi/10.2760/081488 (accessed 02/2023).

[5] IEA (2022), Global Energy Review: $CO_2$ Emissions in 2021, IEA, Paris. https://www.iea.org/reports/global-energy-review-co2-emissions-in-2021-2. (accessed 02/2023).

[6] Centi, G.; Iaquaniello, G.; Perathoner, S. Can We Afford to Waste Carbon Dioxide? Carbon Dioxide as a Valuable Source of Carbon for the Production of Light Olefins. ChemSusChem 2011, 4, 1265 – 1273.

[7] Chauvy,R.; Meunier.N.; Thomas, D.; Weireld, D.G. Selecting emerging $CO_2$ utilization products for short- to mid-term deployment. Appl. Energy. 2019,236, 662.

[8] Kovač, A.; Paranos,M.; Marciuš, D. Hydrogen in energy transition: A review. Int. J. Hydrog. 2021, 46, 10016-10035.

[9] Goud, D.; Gupta, R.; Maligal-Ganesh, R.; Peter, S. C. Review of catalyst design and mechanistic studies for the production of olefins from anthropogenic $CO_2$. ACS Catal. 2020, 10, 14258−14282.

[10] Ethylene demand and production capacity worldwide from 2015 to 2022. APA, Chicago, Harvard, MLA & Bluebook. https://www.statista.com/statistics/1246694/ethylene-demand-capacity-forecast-worldwide/(accessed 02/2023).

[11] Proylene demand and production capacity worldwide from 2015 to 2022. APA, Chicago, Harvard, MLA & Bluebook. https://www.statista.com/statistics/1246689/propylene-demand-capacity-forecast-worldwide/(accessed 02/2023).

[12] Ojelade, O. A.; & Zaman, S. F. A review on $CO_2$ hydrogenation to lower olefins: Understanding the structure-property relationships in heterogeneous catalytic systems. J. $CO_2$ Util. 2021, 47, 101506.

[13] B. Pawelec; R. Guil-López; N. Mota; J. L. G. Fierro; R. M. N. Yerga. Catalysts for the Conversion of CO2 to Low Molecular Weight Olefins—A Review. Materials. 2021,14, 6952.

[14] R. Ye, J. Ding, W. Gong, M. D. Argyle, Q. Zhong, Y. Wang, C. K. Russell, Z. Xu, A. G. Russell, Q. Li, M. Fan, Y. G. Yao, $CO_2$ Hydrogenation to High-Value Products via Heterogeneous Catalysis. Nat. Commun. 2019,10, 5698.

[15] Numpilai, T.; Cheng, C. K.; Limtrakul, J.; & Witoon, T. Recent advances in light olefins production from catalytic hydrogenation of carbon dioxide. Process Saf. Environ. Prot. 2021, 151, 401-427.

[16] Friedel, R. A.; Anderson, R. B. Composition of Synthetic Liquid Fuels. I. Product Distribution and Analysis of $C_5$-$C_8$ Paraffin Isomers from Cobalt Catalyst. J. Am. Chem. Soc. 1950, 72, 1212-1215.

[17] Jadhav, S. G.; Vaidya, P. D.; Bhanage, B. M.; Joshi, J. B. Catalytic carbon dioxide hydrogenation to methanol: A review of recent studies. Chem Eng Res Des, 2014, 92, 2557-2567.

[18] Bowker, M. Methanol synthesis from $CO_2$ hydrogenation. ChemCatChem. 2019, 11(17), 4238-4246.

[19] Schwiderowski, P.; Ruland, H.; Muhler, M. Current developments in $CO_2$ hydrogenation towards methanol–a review related to industrial application. Curr. Opin. Green Sustain. 2022, 100688.

[20] Sha, F.; Han, Z.; Tang, S.; Wang, J.; Li, C. Hydrogenation of Carbon Dioxide to Methanol over Non− Cu-based Heterogeneous Catalysts. ChemSusChem. 2020, 13(23), 6160-6181.

[21] Guil-López, R.; Mota, N.; Llorente, J.; Millán, E.; Pawelec, B. Fierro, J. L. G.; Navarro, R. M. Methanol synthesis from $CO_2$: a review of the latest developments in heterogeneous catalysis. Materials. 2019, 12(23), 3902.

[22] Li, Z.; Wang, J.; Qu, Y.; Liu, H.; Tang, C.; Miao, S.; Feng, Z.; An, H.; Li, C. Highly Selective Conversion of Carbon Dioxide to Lower Olefins. ACS Catal. 2017, 7, 8544- 8548.

[23] Liu, X.; Wang, M.; Zhou, C.; Zhou, W.; Cheng, K.; Kang, J.; Zhang, Q.; Deng, W.; Wang, Y. Selective transformation of carbon dioxide into lower olefins with a bifunctional catalyst composed of $ZnGa_2O_4$ and SAPO-34. Chem. Commun. 2018, 54, 140 -143.

[24] Gao, P.; Dang, S.; Li, S.; Bu, X.; Liu, Z.; Qiu, M.; Yang, C.; Wang, H.; Zhong, L.; Han, Y.; Liu, Q.; Wei, W.; Sun, Y. Direct Production of Lower Olefins from $CO_2$ Conversion via Bifunctional Catalysis. ACS Catal. 2018, 8, 571- 578.

[25] Tian, P.; Wei, Y.; Ye, M.; Liu, Z. Methanol to Olefins (MTO): From Fundamentals to Commercialization. ACS Catal. 2015, 5, 1922- 1938.

[26] Yang, M.; Fan, D.; Wei, Y.; Tian, P.; Liu, Z. Recent Progress in Methanol-to-Olefins (MTO) Catalysts. Adv. Mater. 2019, 31, 1-15.

[27] Sharma, P.; Sebastian, J.; Ghosh, S.; Creaser, D.; Olsson, L. Recent advances in hydrogenation of $CO_2$ into hydrocarbons via methanol intermediate over heterogeneous catalysts. Catal. Sci. Technol. 2021, 11(5), 1665-1697.

[28] Arora, S.S.; Nieskens, D.L.S.; Malek, A. et al. Lifetime improvement in methanol-to-olefins catalysis over chabazite materials by high-pressure $H_2$ co-feeds. Nat. Catal.2018, 1, 666-672.

[29] Shi, Z.; Neurock, M.; Bhan, A. Methanol-to-Olefins Catalysis on HSSZ-13 and HSAPO-34 and Its Relationship to Acid Strength. ACS Catal. 2021, 11, 1222- 1232.

[30] Zhao, X.; Li, J.; Tian, P.; Wang, L.; Li, X.; Lin, S.; Guo, X.; Liu, Z. Achieving a Superlong Lifetime in the Zeolite-Catalyzed MTO Reaction under High Pressure: Synergistic Effect of Hydrogen and Water. ACS Catal. 2019, 9, 3017- 3025.

[31] Gao, F; Szanyi, J., On the hydrothermal stability of Cu/SSZ-13 SCR catalysts. Appl. Catal. A: Gen. 2018, 560, 185-194.

[32] Bleken, F.; Bjørgen, M.; Palumbo, L.; Bordiga, S.; Svelle, S.; Lillerud, K.P.; Olsbye, U. The effect of acid strength on the conversion of methanol to olefins over acidic microporous catalysts with the CHA topology. Top Catal. 2009, 52, 218- 228.

[33] Stangeland, K.; Li, H.;Yu, Z. Thermodynamic analysis of chemical and phase equilibria in $CO_2$ hydrogenation to methanol, dimethyl ether, and higher alcohols. Ind. Eng. Chem. Res. 2018 ,57(11), 4081-4094.

[34] Fornero, E. L.; Chiavassa, D. L.; Bonivardi, A. L.; Baltanás, M. A. $CO_2$ capture via catalytic hydrogenation to methanol: Thermodynamic limit vs.'kinetic limit'. Catal. Today. 2011,172(1), 158–165.

[35] Lunkenbein, T.; Girgsdies, F.; Kandemir, T.; Thomas, N.; Behrens, M.; Schlögl, R.; Frei, E. Bridging the time gap: a copper/zinc oxide/aluminum oxide catalyst for methanol synthesis studied under industrially relevant conditions and time scales. Angew Chem, Int Ed. 2016, 55(41), 12708-12712.

[36] Martin, O.; Martín, A.J.; Mondelli, C.; Mitchell, S.; Segawa, T.F.; Hauert, R.; Drouilly, C.; Curulla-Ferré, D.; Pérez-Ramírez, J. Indium oxide as a superior catalyst for methanol synthesis by $CO_2$ hydrogenation. Angew Chem, Int Ed. 2016, 128(21), 6369-6373.

[37] Frei, M.S.; Capdevila-Cortada, M.; García-Muelas, R.; Mondelli, C.; López, N.; Stewart, J.A.; Curulla-Ferré, D.; Pérez-Ramirez, J. Mechanism and microkinetics of methanol synthesis via CO2 hydrogenation on indium oxide. J. Catal. 2018, 361, 313-321.

[38] Dang, S.; Yang, H.; Gao, P.; Wang, H.; Li, X.; Wei, W.; Sun, Y. A review of research progress on heterogeneous catalysts for methanol synthesis from carbon dioxide hydrogenation. Catal. Today 2019, 330, 61–75.

[39] Tsoukalou, A.; Abdala, P.M.; Stoian, D.; Huang, X.; Willinger, M.G.; Fedorov, A.; Müller, C.R. Structural Evolution and Dynamics of an $In_2O_3$ Catalyst for $CO_2$ Hydrogenation to Methanol: An Operando XAS-XRD and In Situ TEM Study. J. Am. Chem. Soc. 2019, 141, 13497–13505.

[40] Akkharaphatthawona, N.; Chanlekc, N.; Cheng, C.K.; Chareonpanicha, M.; Limtrakule, J.; Witoon, T. Tuning adsorption properties of $Ga_xIn_{2-x}O_3$ catalysts for enhancement of methanol synthesis activity from $CO_2$ hydrogenation at high reaction temperature. Appl. Surf. Sci. 2019, 489, 278–286.

[41] Frei, M.S.; Mondelli, C.; García-Muelas, R.; Kley, K.S.; Puértolas, B.; López, N.; Safonova, O.V.; Stewart, J.A.; Curulla Ferré, D.; Pérez-Ramírez, J. Atomic-scale engineering of indium oxide promotion by palladium for methanol production via $CO_2$ hydrogenation. Nat. Commun. 2019,10 (1), 3377.

[42] Araújo, T.P.; Shah, A.; Mondelli, C.; Stewart, J.A.; Ferré, D.C.; and Pérez-Ramírez, J. Impact of hybrid $CO_2$-CO feeds on methanol synthesis over $In_2O_3$-based catalysts. Appl. Catal. B: Environ. 2021, 285, 119878.

[43] Ferri, P.; Li, C.; Millán, R.; Martínez-Triguero, J.; Moliner, M.; Boronat, M.; Corma, A. Impact of Zeolite Framework Composition and Flexibility on Methanol-To-Olefins Selectivity: Confinement or Diffusion? Angew Chem, Int Ed. 2020, 132(44), 19876-19883.

[44] DeLuca, M.; Janes, C.; Hibbitts, D. Contrasting Arene, Alkene, Diene, and Formaldehyde Hydrogenation in H-ZSM-5, H-SSZ-13, and H-SAPO-34 Frameworks during MTO. ACS Catal. 2020, 10, 4593- 4607.

[45] Olsbye, U.; Svelle, S.; Bjørgen, M.; Beato, P.; Janssens, T. V. W.; Joensen, F.; Bordiga, S.; Lillerud, K. P. Conversion of Methanol to Hydrocarbons: How Zeolite Cavity and Pore Size Controls Product Selectivity. Angew. Chem. Int. Ed. 2012, 51, 5810- 583.

[46] Hu, S.; Shan, J.; Zhang, Q.; Wang, Y.; Liu, Y.; Gong, Y.; Wu, Z. and Dou, T. Selective formation of propylene from methanol over high-silica nanosheets of MFI zeolite. Appl. Catal. A: Gen. 2012, 445, 215-220.

[47] Sassi, A.; Wildman, M.A.; Ahn, H. J.; Prasad, P.; Nicholas, J.B.; Haw, J.F. Methylbenzene chemistry on zeolite H Beta: Multiple insights into methanol-to-olefin catalysis. J. Phys. Chem. B. 2002,106(9), 2294-2303.

[48] Chen, J.; Li, J.; Yuan, C.; Xu, S.; Wei, Y.; Wang, Q.; Zhou, Y.; Wang, J.; Zhang, M.; He, Y.; Xu, S. Elucidating the olefin formation mechanism in the methanol to olefin reaction over AlPO-18 and SAPO-18. Catal. Sci. Technol. 2014, 4, 3268.

[49] Gao, B.; Yang, M.; Qiao, Y.; Li, J.; Xiang, X.; Wu, P.; Wei, Y.; Xu, S. Tian, P.; Liu, Z. A low-temperature approach to synthesize low-silica SAPO-34 nanocrystals and their application in the methanol-to-olefins (MTO) reaction. Catal. Sci. Technol. 2016, 6(20), 7569-7578.

[50] Zhou, J.; Zhi, Y.; Zhang, J.; Liu, Z.; Zhang, T.; He, Y.; Zheng, A.; Ye, M.; Wei, Y.; Liu, Z. Presituated “coke”-determined mechanistic route for ethene formation in the methanol-to-olefins process on SAPO-34 catalyst. J. Catal. 2019, 377, 153-162.

[51] Huang, H.; Wang, H.; Zhu, H.; Zhang, S.; Zhang, Q.; Li, C. Enhanced ethene to propene ratio over Zn-modified SAPO-34 zeolites in methanol-to-olefin reaction. Catal. Sci. Technol. 2019, 9(9), 2203-2210.

[52] Zhong, J.; Han, J.; Wei, Y.; Xu, S.; He, Y.; Zheng, Y.; Ye, M.; Guo, X.; Song, C.; Liu, Z. Increasing the selectivity to ethylene in the MTO reaction by enhancing diffusion limitation in the shell layer of SAPO-34 catalyst. Chem. Commun. 2018, 54(25), 3146-3149.

[53] Dyballa, M.; Obenaus, U.; Blum, M.; Dai, W. Alkali metal ion exchanged ZSM-5 catalysts: on acidity and methanol-to-olefin performance. Catal. Sci. Technol. 2018, 8(17), 4440-4449.

[54] Chen, D.; Moljord, K.; Fuglerud, T.; Holmen, A. The effect of crystal size of SAPO-34 on the selectivity and deactivation of the MTO reaction. Microporous Mesoporous Mater. 1999, 29(1-2), 191-203.

[55] Hwang, A.; Kumar, M.; Rimer, J.; Bhan, A. Implications of methanol disproportionation on catalyst lifetime for methanol-to-olefins conversion by HSSZ-13, J. Catal. 2017, 346, 154 -160.

[56] Liu, Z.; Ni, Y.; Sun, T., Zhu, W., Liu, Z. Conversion of $CO_2$ and $H_2$ into propane over InZrOx and SSZ-13 composite catalyst. J. Energy Chem. 2021, 54, 111-117.

[57] Ni, Y.; Chen, Z.; Fu, Y.; Liu, Y.; Zhu, W.; Liu, Z. Selective conversion of $CO_2$ and $H_2$ into aromatics. Nat. Commun. 2018, 9(1), 3457.

[58] Li, Z.; Qu, Y.; Wang, J.; Liu, H.;Li, M.; Miao, S.; Li, C. Highly selective conversion of carbon dioxide to aromatics over tandem catalysts. Joule, 2019, 3(2), 570-583.

[59] Ghasemi, M.; Mohammadi, M.; Sedighi, M.; Sustainable production of light olefins from greenhouse gas $CO_2$ over SAPO-34 supported modified cerium oxide. Microporous Mesoporous Mater. 2020, 297, 110029.

[60] Numpilai, T.; Wattanakit, C.; Chareonpanich, M.; Limtrakul, J.; Witoon, T. Optimization of synthesis condition for $CO_2$ hydrogenation to light olefins over $In_2O_3$ admixed with SAPO-34. Energy Convers. Manag. 2019,511-523.

[61] Dang, S.; Li, S.; Yang, C.; Chen, X.; Li, X.; Zhong, L.; Gao, P.; Sun, Y. Selective transformation of $CO_2$ and $H_2$ into lower olefins over $In_2O_3$-ZnZrOx/SAPO-34 bifunctional catalysts. ChemSusChem, 2019, 12(15), 3582-3591.

[62] Liu, X.; Wang, M.; Yin, H.; Hu, J.; Cheng, K.; Kang, J.; Zhang, Q.; Wang, Y.Tandem catalysis for hydrogenation of CO and $CO_2$ to lower olefins with bifunctional catalysts composed of spinel oxide and SAPO-34. ACS Catal. 2020, 10(15), 8303-8314.

[63] Wang, P.; Zha, F.; Yao, L.; Chang, Y. Synthesis of light olefins from $CO_2$ hydrogenation over (CuO-ZnO)-kaolin/SAPO-34 molecular sieves. Appl Clay Sci. 2018, 163, 249-256.

[64] Tian, H.; Yao, J.; Zha, F.; Yao, L.; Chang, Y. Catalytic activity of SAPO-34 molecular sieves prepared by using palygorskite in the synthesis of light olefins via $CO_2$ hydrogenation. Appl Clay Sci. 2020, 184,105392.

[65] Chen, J.; Wang, X.;Wu, D.; Zhang, J.; Ma, Q.;Gao, X.; Lai, X.;Xia, H.; Fan, S.; Zhao, T.S. Hydrogenation of $CO_2$ to light olefins on CuZnZr@(Zn-) SAPO-34 catalysts: Strategy for product distribution. Fuel, 2019, 239, 44-52.

[66] Deimund, M.A.; Harrison, L.; Lunn, J.D.; Liu, Y.; Malek, A.; Shayib, R.; Davis, M.E. Effect of heteroatom concentration in SSZ-13 on the methanol-to-olefins reaction. ACS Catal. 2016, 6(2), 542-550.

[67] Lu, S.; Yang, H.; Yang, C.; Gao, P.; Sun, Y. Highly selective synthesis of LPG from $CO_2$ hydrogenation over $In_2O_3$/SSZ-13 binfunctional catalyst, J. Fuel Chem. Technol. 2021, 49(8), 1132-1139.

[68] Zhu, Q.; Kondo, J.N.; Ohnuma, R.; Kubota, Y.; Yamaguchi, M.; Tatsumi, T. The study of methanol-to-olefin over proton type aluminosilicate CHA zeolites Microporous Mesoporous Mater. 2008, 112(1-3), 153-161.

[69] Di Iorio, J.R.; Nimlos, C.T.; Gounder, R. Introducing catalytic diversity into single-site chabazite zeolites of fixed composition via synthetic control of active site proximity. ACS Catal. 2017, 7(10), 6663-6674.

[70] Nishitoba, T.; Yoshida, N.; Kondo, J.N; Yokoi, T. Control of Al distribution in the CHA-type aluminosilicate zeolites and its impact on the hydrothermal stability and catalytic properties. Ind. Eng. Chem. Res.2018, 57(11), 3914-3922.

[71] Huang, Y.; Ma, H.; Xu, Z.; Qian, W.; Zhang, H.; Ying, W. Direct Conversion of Syngas to Light Olefins over a ZnCrO x+ H-SSZ-13 Bifunctional Catalyst. ACS omega, 2021, 6(16), 10953-10962.

[72] Wei, Y.; Li, J.; Yuan, C.; Xu, S.; Zhou, Y.; Chen, J.; Wang, Q.; Zhang, Q.; Liu, Z. Generation of diamondoid hydrocarbons as confined compounds in SAPO-34 catalyst in the conversion of methanol. Chem. Commun. 2012, 48, 3082-3084.

[73] Nieskens, D. L. S.; Lunn, J. D.; Malek, A. Understanding the Enhanced Lifetime of SAPO-34 in a Direct Syngas-to-Hydrocarbons Process. ACS Catal. 2019, 9, 691- 700.

[74] Wang, Y.; Wang, G.; van der Wal, L.I.; Cheng, K.; Zhang, Q.; de Jong, K.P.; Wang, Y. Visualizing Element Migration over Bifunctional Metal-Zeolite Catalysts and its Impact on Catalysis. Angew Chem, Int Ed. 2021,133(32), 17876-17884.

[75] Ding, Y.; Jiao, F.; Pan, X.; Ji, Y.; Li, M.; Si, R.; Pan, Y.; Hou, G.; Bao, X. Effects of proximity-dependent metal migration on bifunctional composites catalyzed syngas to olefins. ACS Catal. 2021,11(15), 9729-9737.

[76] Ghosh. S; Sebastian, S.; Olsson, L.; Creaser, D. Experimental and kinetic modeling studies of methanol synthesis from $CO_2$ hydrogenation using $In_2O_3$ catalyst. Chem. Eng. J. 2021, 416, 129120.

[77] Di Iorio, J.R.; Gounder, R. Controlling the isolation and pairing of aluminum in chabazite zeolites using mixtures of organic and inorganic structure-directing agents. Chem. Mater. 2016,28, 2236-2247.

[78] Lee, S.; Nimlos, C.T.; Kipp, E.R.; Wang, Y.;Gao, X.; Schneider, W.F. Lusardi, M.;Vattipalli, V.; Prasad, S.; Moini, A.; Gounder, R. Evolution of Framework Al Arrangements in CHA Zeolites during Crystallization in the Presence of Organic and Inorganic Structure-Directing Agents. Cryst. Growth Des. 2022,22, 6275-6295.

[79] Dědeček, J.; Kaucký, D.; Wichterlová, B.; Gonsiorová, O. $Co^{2+}$ ions as probes of Al distribution in the framework of zeolites. ZSM-5 study. Phys. Chem. Chem. Phys. 2002, 4, 5406-5413.

[80] Ghosh. S; Sebastian, S.; Olsson, L.; Methanol mediated direct CO2 hydrogenation to hydrocarbons: Experimental and kinetic modeling study. Chem. Eng. J. 2022, 435, 135090.

[81] Database of Zeolite Structures. http://www.iza-structure.org/databases/ (accessed February 20, 2023).

[82] Mlekodaj, K.; Dedecek, J.; Pashkova, V.; Tabor, E.; Klein, P.; Urbanova, M.; Karcz, R.; Sazama, P.; Whittleton, S.R.; Thomas, H.M.; Fishchuk, A.V. Al organization in the SSZ-13 zeolite. Al distribution and extra-framework sites of divalent cations. J. Phys. Chem. C. 2019, 123, 7968-7987.

[83] Jia, C.; Massiani, P.; Barthomeuf, D. Characterization by infrared and nuclear magnetic resonance spectroscopies of calcined beta zeolite. J. CHEM.SOC.FARADAY TRANS. 1993, 89, 3659-3665.

[84] Skarlis, S.A.; Berthout, D.; Nicolle, A.; Dujardin, C.; Granger, P. IR Spectroscopy Analysis and Kinetic Modeling Study for $NH_3$ Adsorption and Desorption on H- and Fe-BEA Catalysts. J. Phys. Chem. C. 2013,117, 7154-7169.

[85] Bordiga, S.; Regli, L.; Cocina, D.; Lamberti, C.; Bjørgen, M.; Lillerud, K.P. Assessing the Acidity of High Silica Chabazite H - SSZ-13 by FTIR Using CO as Molecular Probe: Comparison with H-SAPO-34. J. Phys. Chem. B. 2005,109, 2779- 2784.

[86] Ravi, M.; Sushkevich, V.L.; van Bokhoven, J.A. On the location of Lewis acidic aluminum in zeolite mordenite and the role of framework-associated aluminum in mediating the switch between Brønsted and Lewis acidity. Chem. Sci. 2021,12, 4094- 4103.

[87] Bonura, G.; Cordaro, M.; Spadaro, L.; Cannilla, C.; Arena, F.; Frusteri, F. Hybrid Cu–ZnO–$ZrO_2$/H-ZSM5 system for the direct synthesis of DME by $CO_2$ hydrogenation. Appl. Catal. B: Environ. 2013,140, 16-24.